



U.S. DEPARTMENT OF COMMERCE

Rogers C. B. Morton, Secretary

NATIONAL OCEANIC AND ATMOSPHERIC ADMINISTRATION

Robert M. White, Administrator

ENVIRONMENTAL RESEARCH LABORATORIES

Wilmot N. Hess, Director

PB246932



## NOAA TECHNICAL REPORT ERL 335-AOML 18

# An Evaluation of the Use of the Earth Resources Technology Satellite for Observing Ocean Current Boundaries in the Gulf Stream System

GEORGE A. MAUL

QC  
807.5  
U66  
no. 335  
AOML-18  
C.2

COLO.  
975

the Superintendent of Documents, U. S. Government Printing Office, Wash

C55.13:ERL 335-AOML 18

REPRODUCED BY:  
U.S. Department of Commerce  
National Technical Information Service  
Springfield, Virginia 22161

NTIS



20402

Property of  
NOAA Miami Library / AOML  
4301 Rickenbacker Causeway  
Miami, Florida 33149



## DISCLAIMER


The NOAA Environmental Research Laboratories do not approve, recommend, or endorse any proprietary product or proprietary material mentioned in this publication. No reference shall be made to the NOAA Environmental Research Laboratories, or to this publication furnished by the NOAA Environmental Research Laboratories, in any advertising or sales promotion which would indicate or imply that the NOAA Environmental Research Laboratories approve, recommend, or endorse any proprietary product or proprietary material mentioned herein, or which has as its purpose an intent to cause directly or indirectly the advertised product to be used or purchased because of this NOAA Environmental Research Laboratories publication.

QC  
807.5

U66  
no 335

AOML-18  
C.2

NOAA FORM 25-13 (2-73)		BIBLIOGRAPHIC DATA SHEET		U. S. DEPARTMENT OF COMMERCE NATIONAL OCEANIC AND ATMOSPHERIC ADMINISTRATION	
1. NOAA ACCESSION NUMBER NOAA-75101402		2.		3. RECIPIENT'S ACCESSION NUMBER	
4. TITLE AND SUBTITLE An Evaluation of the Use of the Earth Resources Technology Satellite for Observing Ocean Current Boundaries in the Gulf Stream System				5. REPORT DATE January 1975	
7. AUTHOR(S) George A. Maul				8. REPORT NO. ERL 335-AOML 18	
9. PERFORMING ORGANIZATION NAME AND ADDRESS Environmental Research Laboratories, NOAA Boulder CO 80302				10. PROJECT/TASK NO.	
				11. CONTRACT/GRANT NO.	
12. SPONSORING ORGANIZATION NAME AND ADDRESS  Same				13. TYPE OF REPORT AND PERIOD COVERED NOAA	
				14.	
15. PUBLICATION REFERENCE An Evaluation of the Use of the Earth Resources Technology Satellite for Observing Ocean Current Boundaries in the Gulf Stream System, Tech. # ERL 335-AOML 18, May '75					
16. <del>ABSTRACT</del> Remote sensing of ocean color to locate current boundaries has been tested in the eastern Gulf of Mexico. Infrared techniques fail there several months of the year because surface thermal signatures are destroyed by summer insolation. A 1-year time history of the Gulf Loop Current has been made by a ship in synchronization with the Earth Resources Technology Satellite (ERTS). Surface chlorophyll-a, temperature, and scattering observations show that color signature of the current is present when thermal indications are absent, and thus this flow can potentially be monitored by a combination of visible and infrared techniques. The gain settings for the satellite are not optimized for ocean radiances and hence computer enhancement of the data is required. The ship data demonstrate an annual cycle of growth, eddy separation, and decay of the Gulf Loop Current, but this could not be reproduced with ERTS due to the 18-day orbit cycle and because the sensors were not designed for ocean radiance levels or spectral distributions. This research supports the concept that a visible multispectral scanner is capable of providing triweekly pathlines of the Gulf Loop Current. (Author Modified)					
17. KEY WORDS AND DOCUMENT ANALYSIS					
17A. DESCRIPTORS *Spaceborne photography, * Ocean currents, Water flow, Photography, Limnology, Oceans, Aerial cameras, Currents					
17B. IDENTIFIERS/OPEN-ENDED TERMS  *Satellites, *Satellite photography, *Gulf currents, *Ocean current boundaries Gulf stream, Gulf stream system, Surface manifestation					
17C. COSATI FIELD/GROUP  8C, 8H					
18. AVAILABILITY STATEMENT Superintendent of Documents, U.S. Government Printing Office, Washington D.C. 20402 (C55. 13:ERL 335-AOML 18) <i>Robert Freeman</i>				19. SECURITY CLASS (This report) UNCLASSIFIED	
				20. SECURITY CLASS (This report) UNCLASSIFIED	
				21. NO. OF PAGES 130	

 NOAA Miami Library / AOML  
4301 Rickenbacker Causeway  
Miami, Florida 33149

PRICES SUBJECT TO CHANGE

## INSTRUCTIONS FOR COMPLETING NOAA FORM 25-13

(Bibliographic Data Sheet based on COSATI Guidelines to Format Standards for Scientific and Technical Reports Prepared by or for the Federal Government, PB-180 600. This form is used to report scientific and technical publications by NOAA authors, contractors and grantees. Instructions for completing are as follows.)

### SUBMIT ONE COPY

TO:

Chief, Technical Information Division (D83)  
Environmental Science Information Center  
National Oceanic and Atmospheric Administration  
Washington, D. C. 20235

1. NOAA ACCESSION NUMBER. Leave blank.
2. Leave blank.
3. RECIPIENT'S ACCESSION NUMBER. Leave blank.
4. TITLE AND SUBTITLE. Title should indicate clearly and briefly the subject coverage of the report, and be displayed prominently. Set subtitle, if used, in smaller type or otherwise subordinate it to main title. When a report is prepared in more than one volume, repeat the primary title, add volume number and include subtitle for the specific volume.
5. REPORT DATE. Indicate the date of publication. Include, at least the year and, if possible, the month.
6. PERFORMING ORGANIZATION CODE. Leave blank.
7. AUTHOR(S). Give name(s) in conventional order (e.g., John R. Doe, or J. Robert Doe). List author's affiliation if it differs from the performing organization.
8. REPORT NUMBER. If a report number appears on the publication cover and/or title page, indicate that number in this block.
9. PERFORMING ORGANIZATION NAME AND ADDRESS. Give name, street, city, state, and zip code. List no more than two levels of an organizational hierarchy.
10. PROJECT/TASK NUMBER. Use the project or task numbers under which the report was prepared.
11. CONTRACT/GRANT NUMBER. Insert contract or grant number under which report was prepared.
12. SPONSORING AGENCY NAME AND ADDRESS. Include zip code. If address is identical to block 9, enter "same" in this block.
13. TYPE OF REPORT AND PERIOD COVERED. Indicate interim, final, etc., and dates covered if applicable.
14. SPONSORING AGENCY CODE. Leave blank.
15. PUBLICATION REFERENCE. Enter the journal title, volume, issue, inclusive pages, and publication date for journal articles or the report series title and report number for technical reports.
16. ABSTRACT. Include a brief (200 words or less) factual summary of the most significant information contained in the report. If the report contains a significant bibliography or literature survey, mention it here.
17. KEY WORDS AND DOCUMENT ANALYSIS. Leave blank
18. DISTRIBUTION STATEMENT. Leave blank
- 19 & 20. SECURITY CLASSIFICATION. Preprinted. Do not submit classified reports.
21. NUMBER OF PAGES. Leave blank
22. PRICE. Leave blank



## CONTENTS

	Page
ABSTRACT	1
1. INTRODUCTION	1
1.1 Definition of the Problem	2
1.2 Choice of the Test Site	2
1.3 Prior Ocean Color Observations	3
2. OPTICAL AND HYDROGRAPHIC PROGRAM	6
2.1 Background of Optical Theory	6
2.2 Optical Properties of the Loop Current Front	8
2.3 Background of Hydrographic Observations	12
2.4 Observation Program	14
3. CURRENT PATTERNS AND THEIR SURFACE MANIFESTATIONS	17
3.1 Correlation Between Surface Optical Parameters and Subsurface Temperatures	17
3.2 Pathlines of the Current	19
3.3 Theoretical Relationship Between Surface and Subsurface Fronts	24
4. RADIATION OBSERVATIONS	29
4.1 Theoretical Effect of Sea State on Upwelling Light	29
4.2 Spectroradiometer Observations	32
4.3 ERTS Observations of the Gulf Loop Current	36
4.4 Satellite Evidence of Fine-Scale Features in the Current	46
5. DISCUSSION	50
5.1 Evaluation of Ocean Color Data for Locating the Gulf Loop Current	50
5.2 Some Features of the Current Usefully Observed From Satellites	55
5.3 Suggestions for Future Research	61
6. CONCLUSION	63
7. ACKNOWLEDGMENTS	66
8. REFERENCES	67
9. APPENDIXES	73
APPENDIX A	73
APPENDIX B	90

AN EVALUATION OF THE USE OF THE EARTH RESOURCES TECHNOLOGY  
SATELLITE FOR OBSERVING OCEAN CURRENT BOUNDARIES  
IN THE GULF STREAM SYSTEM

George A. Maul

ABSTRACT

Remote sensing of ocean color to locate current boundaries has been tested in the eastern Gulf of Mexico. Infrared techniques fail there for several months of the year because surface thermal signatures are destroyed by summer insolation. A 1-year time history of the Gulf Loop Current has been made by ship in synchronization with the Earth Resources Technology Satellite (ERTS). Shipboard measurements of upwelling spectral irradiance show that the color change across the cyclonic boundary is associated with changes in chlorophyll-a concentrations and changes in the volume scattering function. Surface chlorophyll-a, temperature, and scattering observations show that color signature of the current is present when thermal indications are absent, and thus this flow can potentially be monitored by a combination of visible and infrared techniques. Shipboard observations indicate that sea-state changes frequently occur at the cyclonic edge; this is recorded in ERTS images which show that the current's boundary can be detected by changes in either color or sea state. Theoretical spectra of upwelling irradiance confirm that surface reflectance changes due to meteorological conditions spectrally alter ERTS radiances. The gain settings for the satellite are not optimized for ocean radiances and hence computer enhancement of the data is required. The ship data demonstrate an annual cycle of growth, eddy separation, and decay of the Gulf Loop Current, but this could not be reproduced with ERTS due to the 18-day orbit cycle and because the sensors were not designed for ocean radiance levels or spectral distributions. This research supports the concept that a visible multispectral scanner, which supplies at least daily observations, is capable of providing triweekly pathlines of the Gulf Loop Current.

1. INTRODUCTION

The objective of this report is to present an evaluation of the use of the Earth Resources Technology Satellite for observing ocean current boundaries. Definition of the problem is discussed first so that the purpose and direction of the research are pellucid at the outset. Choice of the test site and a brief discourse on earlier ocean color investigations complete the introduction. The latter subjects are discussed because the focus of the research is to examine the application of ocean color remote sensing to locating currents in the eastern Gulf of Mexico; Appendix A demonstrates the utility of visible scanning radiometer data in other parts of the Gulf Stream system from Cape Florida to Cape Hatteras.

## 1.1 Definition of the Problem

The location of ocean currents by infrared radiometers in aircraft and satellites is operationally successful from aircraft over the Gulf Stream. The statistical correlation between the surface thermal signature of the Gulf Stream and the velocity core has been studied, and it has been shown (Hansen and Maul, 1970) that north of Cape Hatteras there is a thermal indication of the cyclonic edge (left-hand side facing downstream in the Northern Hemisphere) at all seasons. Atlases, however (e.g., Robinson, 1973), show that major portions of the Gulf Stream system have no surface thermal gradients caused by seasonal heating for as much as 4 months of the year.

The cyclonic edge of the Gulf Stream-type flows is frequently well defined and can often be observed by noting changes in temperature, salinity, color, and sea state (Stommel, 1966, pp. 62-65; Uda, 1938). Color changes imply that the optical properties of the ocean change in the vicinity of the cyclonic edge. If those optical properties are observable when the thermal signature is lost, a year-round remote sensing technique is potentially available.

Specifically, this research is to test the utility of the Earth Resources Technology Satellite, ERTS (supplemented by Skylab photography), for observing ocean currents from changes in the optical properties of the water across the cyclonic edge through information collected in a sequence of ground-truth research vessel cruises in synchronization with the satellite. The research relates upwelling irradiance spectra to the current's surface optical signature, evaluates the seasonality of parameters contributing to the surface optical signature, correlates the surface optical signature and the deeper thermal structure, obtains pathlines of the deeper thermal signature, tests whether ERTS data reproduce the circulation pattern, contributes to basic oceanographic knowledge in the test site, and examines the requirements for an optimum ocean-color-sensing satellite.

## 1.2 Choice of Test Site

Radiation data from the Earth Resources Technology Satellite's Multispectral Scanner (MSS) became available from mid-1972 onward, but almost exclusively over the United States because of limitations in on-board tape recorder capacity. Satellite tracking stations at Greenbelt, Maryland, and Goldstone, California, are able to receive signals over the Gulf of Mexico and into the Cayman Sea, an area that fits the problem definition and is logistically convenient. ERTS has an 18-day revisit time that requires the ocean feature to be studied as a slowly varying phenomenon. Data taken by the R/V DISCOVERER in 1969-70 showed that changes in the circulation patterns in this area were not rapid and that monthly observation schedules would be acceptable.

On the basis of these considerations, the eastern Gulf of Mexico was chosen as the test site. Here, the flow from the Yucatan Strait penetrates northward into the Gulf to a varying degree before exiting through the Straits of Florida. Leipper (1970) proposed an annual cycle of growth,

spreading, and decay of this current system, but it was based on data spaced at random intervals over 2 years including several cruises not designed to collect data on the current. The sequence of current patterns obtained in the present study was designed to provide a proper time series of the Gulf Loop Current from Yucatan to Key West. The surface vessel cruises are at 36-day intervals in synchronization with ERTS overpasses.

Routine monitoring of the Gulf Loop Current has several practical applications: The relatively sterile waters of the current mark a boundary of organic production important to the fishing industry (Austin, 1971). The high velocities in the current can have a marked effect on optimum ship routing. Sound propagation characteristics in the sea change significantly in the vicinity of the current's boundary, having implications for bathymetric surveying and national defense. The location of the Loop Current has been related to storm intensification (Leipper and Volgenau, 1970) in this hurricane fertile region. Environmentalists are concerned about the transport of hydrocarbons and wastes (Smith, 1974).

These data have already been used to document the first Florida east coast red tide (Murphy *et al.*, 1974), wherein the organisms were transported by entrainment from Florida Bay to the Florida east coast. The impact of a recent accidental jettisoning of hundreds of cyanide canisters following a ship collision in the Yucatan Straits is being studied with these results (Corwin and Richardson, 1974). The Gulf of Mexico thus represents an area of regional interest where knowledge of surface current trajectories in real-time is an important contribution to the proper use of the oceans.

### 1.3 Prior Ocean Color Observations

Early work on ocean color is summarized by Schott's 1935 map (Neumann and Pierson, 1966, p. 68) of Forel color for the Atlantic Ocean in figure 1. The contours of Forel scale number clearly separate the Sargasso Sea from the east coast of North America's coastal waters. Similarly, Joseph and Wattenbergs' 1944 map (Neumann and Pierson, 1966, p. 65) of the distribution of the vertical extinction coefficient in the Atlantic almost duplicates Schott's distribution of color (fig. 1): The Sargasso Sea is a clear, blue, water mass, juxtaposed with a green, more turbid coastal water mass.

Observations have shown that the temperature and salinity change at the cyclonic edge of the Gulf Stream is well correlated with a rapid change in horizontal velocity shear (e.g., Maul and Hansen, 1972). A color change is associated with this shear but the correlation was not established. In the summer of 1971, observations were taken by the author while on board the R/V KNORR in the Gulf Stream off New England. The Forel-scale color failed to correlate with surface temperature changes: Forel number 0-1 were always recorded in the Stream with higher temperatures, and Forel numbers 4-5 were always observed at stations in the slope water outside of the Stream with lower surface temperatures. These changes were noted even if the station spacing inside and outside the boundary was only several kilometers apart. From these observations, it appears that color change is as viable an indicator of the cyclonic edge as temperature or salinity.

Hanson (1972) reviewed the field of ocean remote sensing and discussed

the techniques for measuring temperature in the infrared or microwave, salinity and sea state in the microwave, and color by visible spectroscopy. The research effort discussed herein centers on the use of the visible and reflected infrared portion of the electromagnetic spectrum (400-1100 nm). Yentsch (1960) contributed to using remote spectral devices in this spectral region in his study on the influence of phytoplankton pigments on the color of the sea. That paper, and a later one (Yentsch, 1962), discussed changes in the absorption spectra of sea water due to chlorophylls and to particulates. The absorption spectra show a shift in the wavelength of maximum transparency toward the green with increasing chlorophyll concentrations; larger particle sizes cause higher attenuation of light in the shorter wavelengths of the spectrum. The Forel color shift in the ocean (fig. 1) is explained by these results.

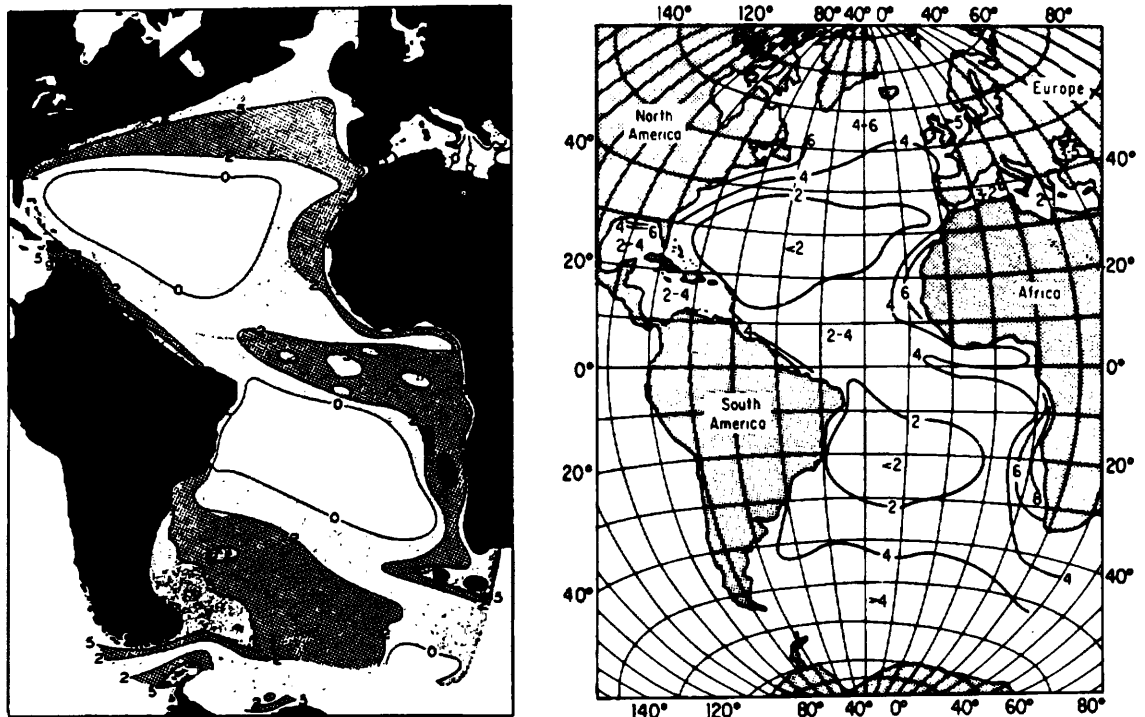


Figure 1.1a (left): Color of the sea as indicated in percent of yellow as indicated by the Forel scale, according to Schott.  
 Figure 1.1b (right): Distribution of the vertical extinction coefficient (x100) of the surface water, according to Joseph and Wattenberg (both figures after Neumann and Pierson, 1966).

Remote sensing of the color, on the other hand, is a corollary to the absorption spectra problem. Clark et al. (1970) obtained reflectance spectra of upwelling radiance from aircraft over the Sargasso Sea, the New England slope water, and Georges Bank. They related the spectra of back-scattered light to varying chlorophyll concentration and noted that anomalies in the spectra are related to other biochromes, suspended sediment, surface reflection, polarization, and air light. Chandrasekhar (1960) showed from radiative transfer theory that the reflectance spectra at the ocean's surface are a function of both the scattering and attenuation of the water itself and the materials suspended or dissolved in it. Chandrasekhar's theory gives a qualitative explanation of the spectra obtained by Clark et al.: Higher reflectances are caused by increased scattering, and shifts in the wavelength of maximum reflectance are due to absorption (see also Yentsch, 1960, 1962).

The results discussed above form the basis for this study. In the Gulf Stream off New England, a color change is associated with the cyclonic edge of the current. That color shift is associated with changes in the concentration of pigment forming molecules in the water, and it can be detected by airborne spectroradiometers. If similar results can be obtained in the test site, then ocean color can be used to delineate the boundary of the Gulf Loop Current. The following sections will discuss ocean spectra in light of more recent theoretical results and the application of the color sensors aboard the Earth Resources Technology Satellite to current boundary location.

## 2. OPTICAL AND HYDROGRAPHIC PROGRAM

The subsections of this chapter elucidate the background of the research. The optical theory necessary to interpret both the shipboard observations and satellite data is presented. An aircraft/ship experiment conducted before the satellite launch is used to test whether ERTS has the basic capability to observe ocean color, and what surface vessel measurements are required to obtain satisfactory ground truth. Previous hydrographic observations in the Gulf of Mexico are then researched, and a useful indicator of the Gulf Loop Current's deeper thermal signature is chosen for the time series. Finally, the observation program and measuring techniques are discussed.

### 2.1 Background of Optical Theory

The radiance ( $N(\lambda)$ ) at the top of the atmosphere can be written as the sum of the ocean surface radiance ( $N_s(\lambda)$ ), the diffuse radiance from beneath the ocean ( $N_d(\lambda)$ ), and the radiance from the atmosphere ( $N_a(\lambda)$ ):

$$N(\lambda) = \alpha(\lambda)N_s(\lambda) + \gamma(\lambda)N_d(\lambda) + N_a(\lambda) \quad (2.1)$$

where  $\alpha(\lambda)$  and  $\gamma(\lambda)$  are atmospheric transmittance factors for  $N_s$  and  $N_d$ , and  $\lambda$  is wavelength. The effect of the atmosphere on ocean color sensing from space has been recently studied by Curran (1972). In this work, however, interest is in determining the boundary of these baroclinic flows by changes in the optical properties of the ocean ( $N_s, N_d$ ). The radiance of the atmosphere does not contribute to determining these ocean properties except to reduce the contrast, unless there is significant atmospheric spatial variability. The effect of sea state on  $N(\lambda)$  is to spectrally alter  $N_s(\lambda)$ ; this will be discussed in section 4.2.

Gordon (1973) constructed a single scattering model for the ocean wherein he related the diffuse reflectance ( $R_d(0,-)$ ) just above the sea surface (defined as the ratio of the upwelling irradiance ( $H(0,+)$ ) to the downwelling irradiance ( $H(0,-)$ )) to several optical properties of the water and its suspended or dissolved materials.  $R_d(0,-)$  as defined here does not include the surface component and is proportional to  $N_d$ ,

$$N_d \propto R_d(0,-) \cdot H(0,-) = H(0,+), \quad (2.2)$$

where the proportionality constant depends on angle. The optical parameters in Gordon's model are  $\omega_0$ , which is defined as the ratio of the beam scattering coefficient ( $b$ ) to the total beam attenuation coefficient ( $c$ ), and  $B$ , which is the fraction of backscattered light:

$$B \equiv 2\pi \int_{\pi/2}^{\pi} \frac{\beta(\theta)}{b} \sin \theta d\theta. \quad (2.3)$$

$\beta(\theta)$  in (2.3) is the volume scattering function which relates to the intensity of radiation ( $dJ(\theta)$ ), singly scattered from a small sample volume ( $dv$ ) when illuminated by an incident irradiance ( $H_0$ ) through

$$\beta(\theta) \equiv \frac{dJ(\theta)}{H_0 dv} \quad (2.4)$$

Examples of measurements of this variable are given later in section 2.2. It has been shown that  $\beta(45^\circ)$  and  $b$  are well related in the ocean (Beardsley *et al.*, 1970). In Gordon's model, for a semi-infinite ocean, the forward-scattered light is approximated by a delta function (cf., Jerlov, 1968), and the diffuse reflectance can be written

$$R_d(0, -) = \frac{k \omega_0 B}{1 - \omega_0 F} \quad (2.5)$$

where  $F$  is the fraction of forward-scattered light ( $1-B$ ), and  $k$  is a constant. Each of the variables in (2.2), (2.3), (2.4), and (2.5) are dispersive, that is, they are wavelength dependent and will be tacitly assumed to be so hereforth.  $R_d$  is the contribution to the reflectance of photons from the atmosphere that penetrate the ocean's surface and are scattered back into the atmosphere.

Equation (2.5) allows spectra to be computed for comparison with observations. The important oceanic parameters are  $\omega_0$  and  $B$ . These independent variables provide an infinite set of possible contributions to the upwelling light, and they must be known to interpret observations. Unfortunately  $\omega_0$  is only imperfectly known even for pure water, and the contributions to  $B$  from particles alone ( $B_p$ ) are unknown. From the behavior of  $R_d$ , Maul and Gordon (1974) were able to show that the spatial gradient of (2.1) in two ERTS bands can give quantitative information about the gradient of particle concentrations in the sea. This is a useful result for locating ocean currents from ERTS because there are large changes in the extinction coefficient (Joseph and Wattenburg)<sup>1</sup> across these boundaries.

ERTS is a polar-orbiting research and development satellite originally designed to return seven channels of data; one instrument failed (channels 1-3) early in the mission. The ground swath is 185 km wide and the revisit time is 18 days. The sensors of the multi-spectral scanner are in the visible and near infrared (reflected infrared) region. Pertinent details are summarized in table 2.1.

<sup>1</sup> Cited by Neumann and Pierson (1966), p. 65.



Table 2.1 Multispectral Scanner Specifications

Band	Bandpass (nm)	Nominal radiance response (mW cm <sup>-2</sup> sr <sup>-1</sup> )	Digital steps (Quantized onboard)
MSS-4	500-600	0-2.48	128
MSS-5	600-700	0-2.00	128
MSS-6	700-800	0-1.76	128
MSS-7	800-1100	0-4.60	64

Note: The Earth Resources Technology Satellite's multispectral scanner is quantized onboard and the data relayed in a digital bit stream. An oscillating mirror system reflects upwelling radiation into six detectors for each channel so that six scanlines of the earth are observed simultaneously. Energy for each quantum step can be estimated by assuming a linear relationship over the 128 (64) steps (NASA, 1971).

The satellite does not receive any information from the blue portion of the spectrum (400-500 nm). It seems that this is a severe limitation for oceanography since most of the spectral information observed at the sea surface is contained in this spectral interval (see section 4.2).

The penetration depth of the ERTS sensors is important in data interpretation because, in the coastal zone, bottom reflection contributes to  $R_d$ . Gordon and McCluney (1974) have studied this and show that in the open ocean, the mean penetration depth is 15 to 18 m for MSS-4, and 3 m for MSS-5. In the coastal zone, these values will be even less because of larger values of the absorption coefficient ( $a_y$ ) due to yellow substance (Gelbstoff; Kalle, 1938). Charnell and Maul (1973) showed that, for MSS-6 and MSS-7, pure water is essentially opaque because of very large attenuation coefficients in the near infrared; therefore, any information from MSS-6 or MSS-7 can be considered surface data only, whereas some subsurface variability may be inferred from MSS-4 and MSS-5.

## 2.2 Optical Properties of the Loop Current Front

Figure 2.1 is a south-north section through the cyclonic front of the Gulf Loop Current near Dry Tortugas. These data were collected during a joint ship/aircraft experiment on 27-28 June 1972, and are representative of the variability in temperature, scattering, chlorophyll-a concentration, and spectra.

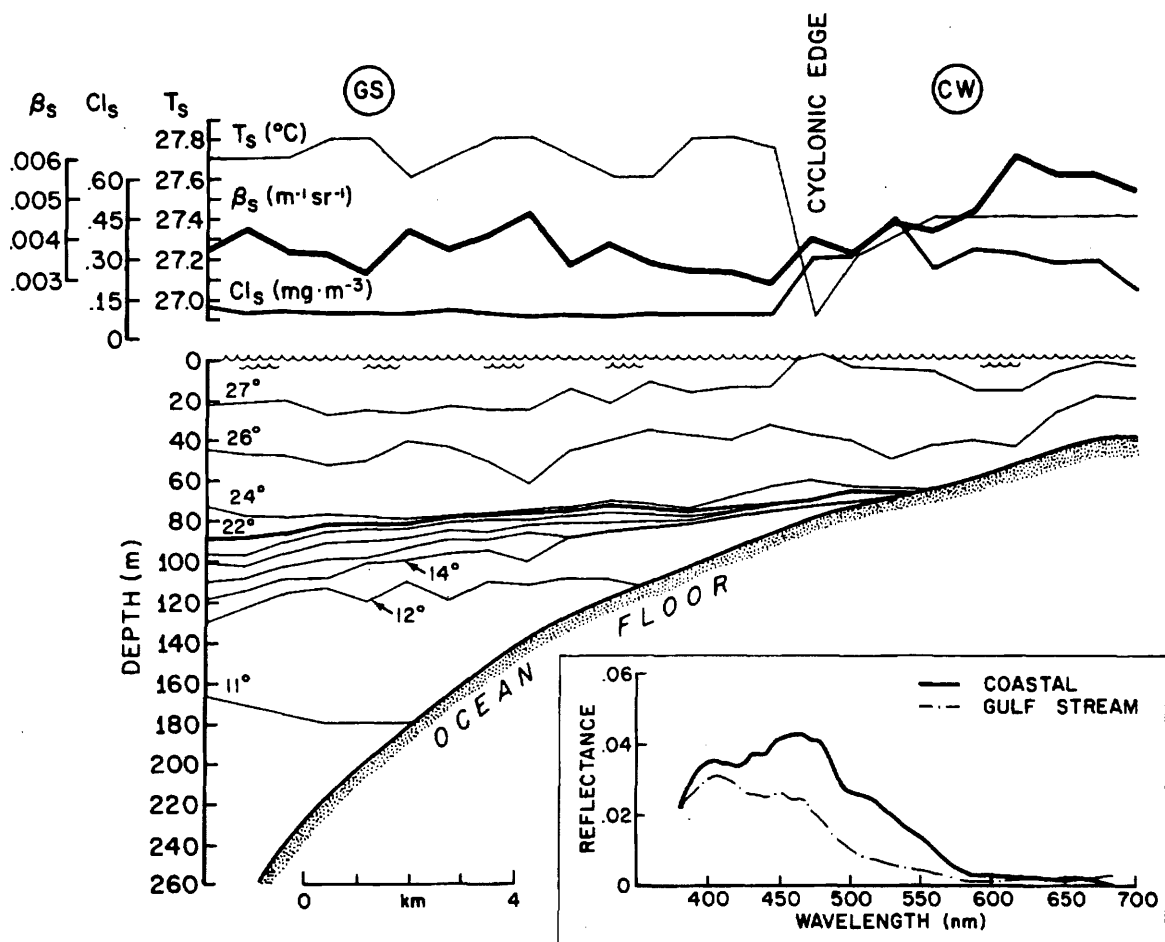


Figure 2.1 South-to-north (left to right) cross section of the Gulf Loop Current's cyclonic boundary. Isotherms in the thermal cross section are in degrees Celsius. The cyclonic edge marks not only where temperature, scattering, and chlorophyll values change, but also salinity, current velocity, and frequently sea state. Inset are reflectance spectra; one taken in the Gulf Stream (GS), the other taken in the coastal water (CW). Mixed layer depth suggests that the optical properties which affect spectra are homogeneous for at least 20 m.

The surface temperature field ( $T_s$ ) shows a marked decrease near the current's edge. This is the thermal signature that completely disappears for 3 or 4 months when summer insolation makes these waters isothermal, thus rendering infrared techniques useless. The subsurface thermal field reflects early summer conditions: mixed layer depth of approximately 20 m, gentle slope of warmer isotherms (i.e., 22 $^{\circ}\text{C}$ ), and steeper slope of cooler isotherms (i.e., 14 $^{\circ}\text{C}$ ) when going toward the current. The core of the current is further offshore (to the left) than this section shows. Details of the boundary between the current and coastal waters are emphasized here to demonstrate use of visible techniques for remote sensing in tropical and subtropical waters.

Profiles of surface chlorophyll-a concentration ( $Cl_s$ ) and volume scattering function at  $45^\circ$  ( $\beta(45)_s$ ) made during the transect are shown along with the thermal signature. Light-scattering measurements were made during the experiment using a Brice-Phoenix light-scattering photometer and a blue (436 nm) filter. The volume-scattering function defined in (2.4) was calculated using

$$\beta(45^\circ) = \frac{a}{h \pi} \frac{TD}{D(0^\circ)} \tau \sin 45^\circ, \quad (2.6)$$

where  $a$  is the ratio of the working standard diffuser to the reference standard diffuser,  $\beta(45^\circ)$  is in units of  $m^{-1}sr^{-1}$ ,  $TD$  is the transmittance of the reference standard diffuser,  $h$  is the dimension of the irradiated element,  $D$  is the deflection of the galvanometer, and  $\tau$  is the transmittance of the neutral density filters. Chlorophyll-a measurements were made in vitro on a fluorometer calibrated with pure chlorophyll-a. The calibrations were checked on a spectrophotometer, and calculations were made using the S. C. O. R./ U. N. E. S. C. O. (Strickland and Parsons, 1968) equation:

$$Cl = 11.64 E_{663} - (2.16 E_{645} + 0.10 E_{630}), \quad (2.7)$$

where  $Cl$  is the chlorophyll-a concentration in  $mg\ m^{-3}$ ,  $E$  is the extinction (defined as the logarithm of the reciprocal of transmittance), and subscripts are the applicable wavelength in nanometers. These techniques are used for all values reported herein.

The profiles demonstrate that the general level of scattering is  $0.7 \times 10^{-3} m^{-1} sr^{-1}$  (18%) more in the coastal water than in the current. Similarly the chlorophyll-a concentration is  $0.2\ mg\ m^{-3}$  (100%) more in coastal water. This is the general situation observed in these transects especially near the coast; however, many times there were no distinct changes of these indicators of optical properties across the cyclonic edge, and there were instances where scattering from an isolated sample was higher in the current, (see section 3.1). The slight peak in  $Cl_s$  just before reaching the edge is a common feature (Lorenzen, 1971). Maul (1973) related these chlorophyll peaks to the edge of currents, and it appears to be a feature of the accumulation of materials so often observed near the cyclonic edge (e.g., Stommel, 1966, p. iv).

Spectra of upwelling irradiance at 1-m depth and downwelling irradiance from the sun and sky 3 m above the water's surface were obtained during the ship/aircraft experiment. Reflectance ratios (uncorrected for the immersion effect, Tyler and Smith, 1970) are graphed as an inset on figure 2.1. Approximate location of these observations in the Gulf Stream (GS) and coastal waters (CW) are indicated on the top of the figure. The reflectance in coastal waters is generally higher than in the current, and the wavelength of maximum intensity is shifted to higher values. This is in agreement with color aerial photographs taken concurrently: A distinct discontinuity

in color from the green of the coastal water to the blue of the Gulf Stream occurred at the point labeled cyclonic edge in figure 2.1.

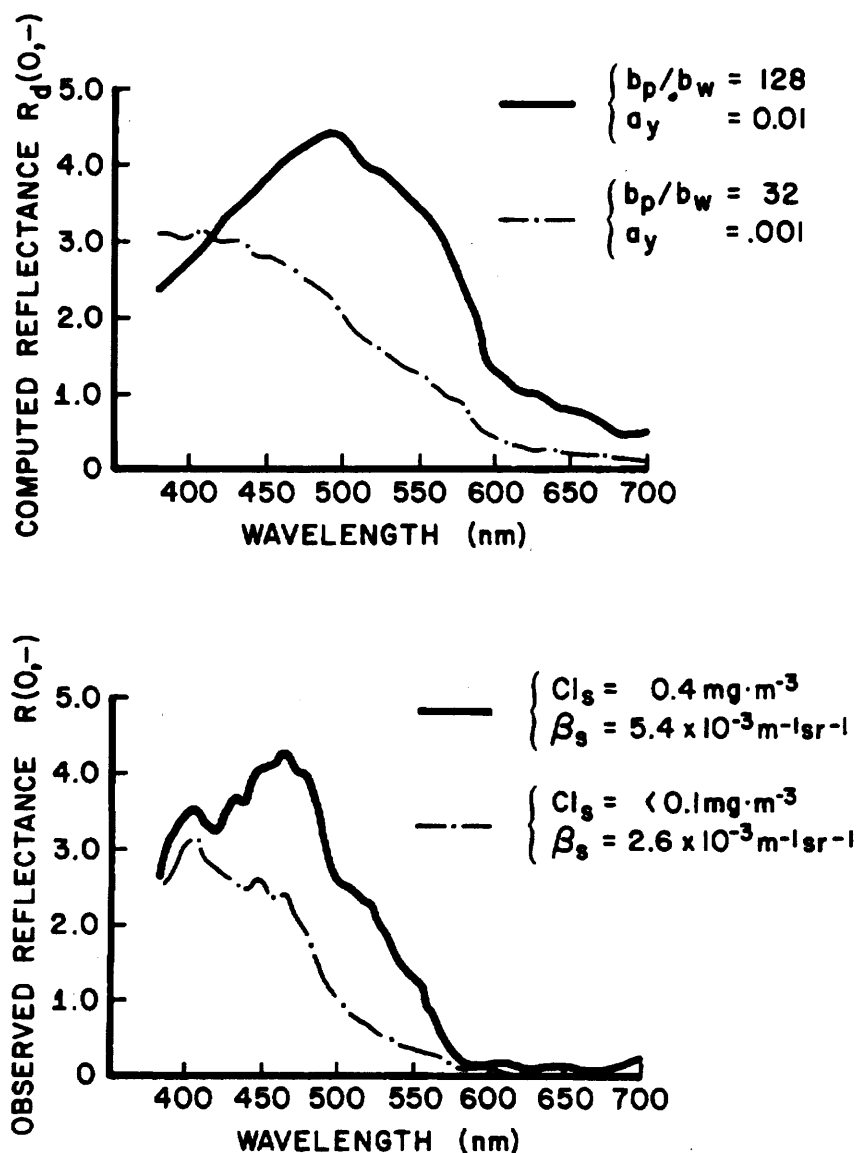


Figure 2.2a Theoretical spectra computed for ratio of particle scattering to water scattering of 128 (solid line) and 32 (dashed line). The beam attenuation coefficients were 0.01 and 0.001 ( $a_y$  values at 550 nm), respectively, for this example of coastal and offshore water types. Figure 2.2b Observed reflectance spectra for coastal (solid line) and Gulf Stream (dashed line). The surface volume scattering is for blue light at  $45^\circ$ . See figure 2.1 for geographic location.

Figure 2.2a contains the reflectance spectra for two water types. These spectra were calculated using the Monte Carlo technique by Gordon *et al.* (1974): (2.5) is a very good approximation to the full equation, which is a polynomial fit in powers of  $\beta\omega_0/1-\omega_0F$ . The solid curve is computed using a ratio of the particle-scattering coefficient ( $b_p$ ) to the pure-water scattering coefficient ( $b_w$ )=128; the ratio  $b_p/b_w$  is proportional to the concentration of suspended particles. The dashed line uses  $b_p/b_w=32$ , and hence is much lower in suspended materials. This is qualitatively analogous to the lowered-volume scattering function in the current. The values labeled  $a_y$  are beam absorption coefficients ( $a=c-b$ ) for yellow substance only. Range of  $a_y$  is chosen to represent coastal and oceanic values. For comparison, the observed reflectance spectra in figure 2.2b are from the inset to figure 2.1.

Referring to (2.5), it is seen that at a given wavelength, if  $B$  remains constant, the reflectance is dependent on the scattering albedo ( $\omega_0$ ). As more and more particles are added to the suspension,  $\omega_0$  increases and the upwelling radiance increases. In figure 2.2b, it is seen that  $\beta(45^\circ)$  has doubled in going from the current into coastal water. Simply increasing  $a_y$  would decrease  $\omega_0$  with a resultant decrease in  $N_d$ . The absorption coefficient is very dependent on wavelength. This causes a shift in the spectral peak to a longer wavelength, i.e., the water appears green to the eye. This is not to say that the chlorophyll-a and the Gelbstoff produce quantitatively similar results; in general they will not. What it does imply is that the broad absorption bands in pigments, such as chlorophyll and Gelbstoff at shorter wavelengths (<600 nm), produce qualitatively similar effects in the spectra. In nature, however, such as in a plankton bloom or in coastal waters, increased amounts of chlorophyll are normally accompanied by increased particle concentrations (organisms which contain the chlorophyll) as well as increased amounts of Gelbstoff. Since  $a$  and  $b$  vary almost independently, the reflectance signature, which depends on  $\omega_0$  and  $B$ , is not unique and can be unraveled only when the variation of the optical properties of the individual components with wavelength is known.

The aircraft experiment thus established that the color signature of the Gulf Loop Current was identical with the thermal signature, that an optical signature was present in summer, and that appropriate surface parameters for identifying that signature were chlorophyll-a concentration and volume scattering function. The observed reflectance spectra showed that there was variation in the MSS-4 bandpass interval and that the color change was potentially observable from ERTS. These results suggested that the eastern Gulf of Mexico was an acceptable test site, and the background of hydrographic conditions was researched.

### 2.3 Background of Hydrographic Observations

Early hydrographic work in the Gulf of Mexico has been summarized by Galtsoff (1954) who edited a complete overview of the biology, chemistry, geology, and physics of the area: In 1895, Lindenkohl published a map of the temperature field at 250 fm (457 m), in degrees Fahrenheit, which is reproduced in figure 2.3. The warm waters of the Caribbean can be seen flowing northward into the Gulf and penetrating deeply into the ambient

thermal field; similarly the Gulf Stream, seen as a region of large horizontal temperature gradient, is flowing easterly and then northerly through the Straits of Florida. In an analysis of these data, Sweitzer, in 1898, reported that the circulation was a spreading of this inflow which resulted in an anticyclonic circulation around the entire Gulf basin. Parr, in 1935, reported the opposite conclusion using ATLANTIS data taken in 1933; he stated that the Gulf Stream takes the shortest path from Yucatan to the Straits of Florida. Leipper expressed this divergence of opinion as the state of knowledge in 1954 even after reviewing Dietrich's 1939 map of the salinity maximum core, which reflects the deep penetration seen in figure 2.3.

Work done in the 1960's, notably by Leipper, and others (Capurro and Reid, 1972), led Leipper to speculate that there was an annual cycle in the current patterns in the eastern Gulf.

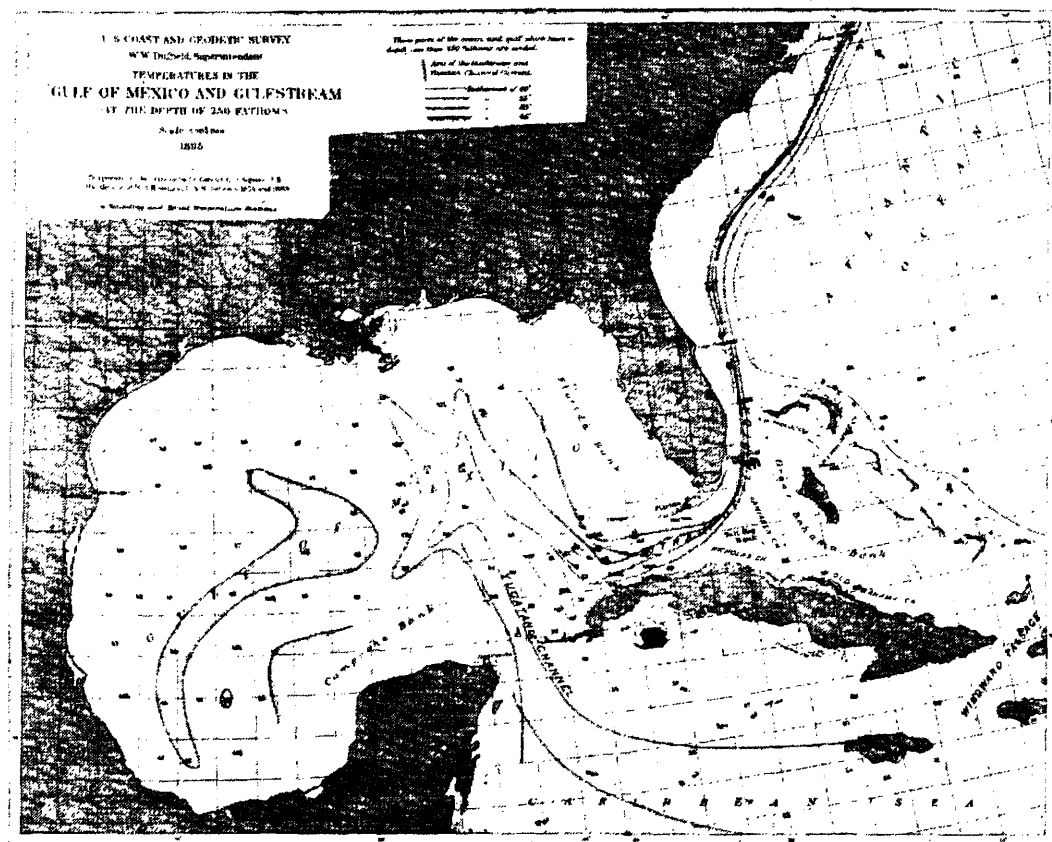


Figure 2.3 Lindenköhl's 1895 map of the temperature field ( $^{\circ}\text{F}$ ) at 250 fm in the Gulf of Mexico. Data are from soundings made by Sigsbee, Bartlett, and Brownson between 1874 and 1883. The shallow waters (<250 fm) of Campeche Bank and the west Florida Platform are stippled on the chart.

Bottom topography in the eastern Gulf of Mexico is dominated by a broad shallow shelf extending north of the Yucatan Peninsula, the Campeche Bank, and another broad shallow shelf west of Florida, the west Florida Platform. The continental slopes are marked by steep escarpments along the west Florida area and northeast of Campeche. Sill depth in the Yucatan Strait is 2000 m, and in the Straits of Florida is approximately 800 m (see inset to fig. 2.4). As the Yucatan Current flows over Campeche Bank, the bottom topography has been thought to control the flow as far north as 23°30'N (Molinari and Cochrane, 1972): Above that latitude, the flow is no longer so constrained. After leaving the confines of the Campeche Bank, the Gulf Loop Current makes an anti-cyclonic turn in the deep water of the basin, and once again is channeled by the Florida Platform and the Cuban Platform into the Straits of Florida.

The water masses in the eastern Gulf are essentially the same below the depth of the 17° C isotherm (Nowlin and McLellan, 1967) as evidenced by the temperature-salinity (T-S) relationship. The depth of this isotherm varies considerably, and as expected from simple dynamical considerations, 17° C is several hundred meters deeper under the current and in the Yucatan Water. Above the 17° C isotherm, the T-S relation for Gulf Loop Current Water and Eastern Gulf of Mexico Water, shows a distinct difference. The former has higher salinities, which reach a maximum near 22° C; the latter is generally cooler at the same saline level. Following the precedent of Wennekens (1959), all the water originating in the Yucatan Strait is referred to as Yucatan Water, the water along the continental shelves as Shelf Water, and the resident eastern Gulf of Mexico water as Eastern Gulf Water. The Yucatan Water is modified as it flows through the Gulf Loop Current (region of anticyclonic turning) and into the Straits of Florida, as evidenced by a decrease in the salinity maximum of the Subtropical Underwater (Wust, 1964). For consistency, the current regime is referred to by these three subdivisions: Figure 2.4, Yucatan Current as defined by the hydrographic sections from Cabo San Antonio, Cuba, to Isla Contoy, Mexico; Gulf Loop Current as the regime from the Yucatan section to the Key West, Florida, to Habana, Cuba, hydrographic section; Florida Current, eastward of the latter section.

#### 2.4 Observation Program

Leipper showed that the 22° C isotherm at 100-m depth was a good indicator of the current in all seasons of the year. Adopting this as the basis for the tracking strategy, this isotherm is followed with expendable bathythermographs (XBTs). The first four cruises were started in St. Petersburg. On the day of every second overpass by ERTS, the ship occupied the suborbital track; XBT data along the NNE-SSW tending line in figure 2.4 typify the ground track. Upon reaching the Yucatan Strait, a Salinity-Temperature-Depth (STD) profile was made at each of nine stations. After observing this hydrographic section, a zig-zag tracking pattern was initiated heading downstream, so that the average speed of the ship was boosted 2 kt. Typically, hourly XBT's were taken. When the depth of the 22° C isotherm exceeded approximately 125 m, the ship's course was altered to the left. This course was run until the 22° C isotherm was less than 80 m, and then course was altered to the right. The pattern was continued from Yucatan around the Loop to Dry Tortugas, in all but a few cases, where weather or fuel considerations made it advisable to run for Key West. The Key West-Habana section of seven STD lowerings was occupied after a short refueling

stop. From January through the end of the project (eight cruises), the cruises originated from Miami, and the Key West-Havana section was done first; this section is also a suborbital track.

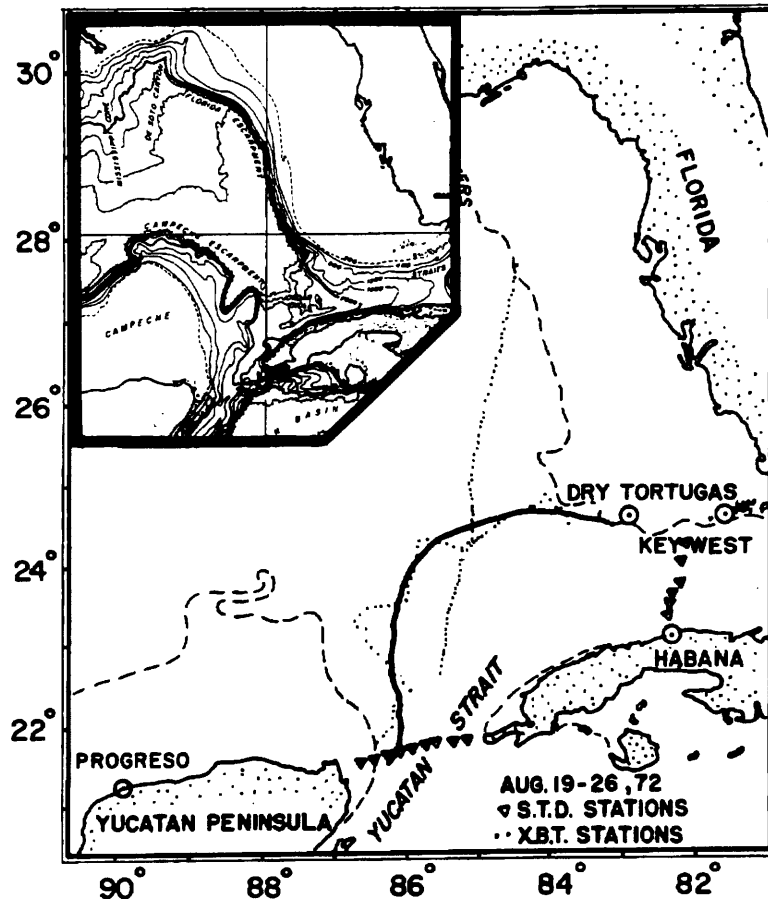


Figure 2.4 Example of the tracking technique is given in the main figure for August 1972. Dots are XBT drops and triangles are STD lowerings. The solid line is the pathline. (Inset) Bottom topography in the eastern Gulf of Mexico. Contours are in meters and show the topography of the deep eastern basin surrounded by the Florida, Campeche, and Cuban Platforms.

After each trip, the position data were replotted and a smooth plot constructed, which made a best fit to the estimated courses and speeds made good. Positioning was accomplished using Loran-A, radar, visual, and celestial observations. It is difficult to estimate errors, but based on Loran-A/radar comparisons,  $\pm 1$  to 3 km seem reasonable. The expendable BT strip chart recorder was tested (and adjusted if necessary) before each cruise with a test canister. The average-surface-bucket temperature and the average-XBT-surface temperature (from the recorder) were calculated for each cruise, and the surface XBT temperature was adjusted for the difference in the average.



In addition to the routine XBT observations described above, continuous flow measurements of chlorophyll-a using the technique of Lorenzen (1966), modified to include a bubble trap, were recorded. An infrared radiometer with a special 10.5- to 12.5- $\mu$ m bandpass filter recorded continuous near-surface measurements of radiation temperature for comparison with the NOAA-2 meteorological satellite (Maul and DeVivo, in preparation); these will be the first such comparison in the same wavelength interval. Volume scattering at 45°, 90°, and 135° was observed, using both blue (436 nm) and green (546 nm) light, on the suborbital track and at each STD station. During appropriate daylight hours, spectra of upwelling and downwelling irradiance were observed for correlation with the biological data and the optical data. STD stations were taken to a depth of 1000 m, or 100 m from the bottom, whichever was less. Surface calibration points were taken at each cast, and the lowering speed was about 50 m per minute. Station spacing was about 20 km, and no stations were closer than 22 km (12.4 mi) to foreign coasts.

### 3. CURRENT PATTERNS AND THEIR SURFACE MANIFESTATIONS

To interpret the ERTS data, ground-truth cruises were conducted. This section opens with an analysis of the correlation of the annual cycle of the surface optical signature of the Gulf Loop Current and the relation of that surface expression to the deeper thermal signature. Details of the pathlines are then discussed for their contribution to the physical oceanography of the Gulf of Mexico. In the last section, the theoretical relationship between the surface and 200-m fronts of a two-layer model are explored, and the importance of curvature in the pathlines is analyzed. The potential contribution and limitations of surface observations to needs in ocean physics are examined.

#### 3.1 Correlation Between Surface Optical Parameters and Subsurface Temperatures

During each of the transects of the Straits of Florida and the Yucatan Strait, profiles of surface-chlorophyll and surface-volume scattering function were made. The aircraft experiment summarized in figure 2.1 shows that the cyclonic edge is closely correlated to the maximum positive gradient in chlorophyll-a when proceeding toward the boundary from the current. Since this is the region of the current that an ocean color sensor will record as the boundary, the correlation between this maximum chlorophyll gradient and the deeper thermal structure must be established. Particularly, the correlation between the 22°C isotherm at 100-m depth is needed, and, for comparison with earlier work by Hansen and Maul (1970) in the Gulf Stream off New England, the 15°C isotherm at 200-m depth is also investigated.

The transect data, separated by months, are summarized in table 3.1. The first column is the month of the survey. The second column lists the horizontal separation in kilometers between the cyclonic edge at the surface (CE) and the 22°C isotherm at 100-m depth. Column three is similar to column two except being for the 15°C isotherm at 200 m. The fourth column is the average-surface chlorophyll-a concentration in the current (GS); the sixth column is the percent increase in chlorophyll-a concentration in the coastal water over that in the current. The volume-scattering function (not tabulated) showed general agreement with these trends in agreement with the discussion in section 2.2.

One reason that Leipper chose the 22°C isotherm as an indicator is evident from table 3.1. All blank entries, except January 1973, are caused by the indicator being aground; January is the one exception, in that no transects were made because of operational difficulties. The shallower indicator isotherm is more reliable in these waters as Leipper suggested. The horizontal separations are somewhat larger in the Yucatan Strait than in the Straits of Florida, possibly because of higher current velocities in the narrower Key West-Habana section. On the average, however, the separation is approximately 15 km, which is very close to the average value of 14.7 km reported by Hansen and Maul off New England between the maximum surface thermal gradient and the maximum thermal gradient at 200 m. This is unexpected, in that the ratio of the Coriolis parameter at Gulf of Mexico latitudes to New England is 0.6, and initially the separation would be expected to be larger in southern latitudes.

Table 3.1 Separation of Surface Front and Indicator Isotherm

YUCATAN	CE-22 @ 100 (km)	CE-15 @ 200 (km)	Cl <sub>s</sub> (GS) (mg.m <sup>-3</sup> )	Cl <sub>s</sub> (CW) (mg.m <sup>-3</sup> )	Difference %
AUG 72	2	-	0.13	0.89	(585)
SEP 72	-	-	-	-	-
O-N 72	6	-	0.85	1.24	46
DEC 72	10	-	0.34	0.64	88
JAN 73	-	-	-	-	-
FEB 73	8	-	0.36	0.48	33
MAR 73	23	19	0.14	0.16	14
A-M 73	-	-	0.20	0.23	15
JUN 73	20	6	0.18	0.32	78
JUL 73	25	-	0.31	0.49	58
AUG 73	37	61	0.40	0.55	38
SEP 73	28	18	0.37	0.51	38
AVE±σ	17.7±11.7	26.0±24.0	0.33±.21	0.55±.32	45±26 (99 ± 172)
FLORIDA					
AUG 72	13	13	0.06	0.13	117
SEP 72	-	-	0.06	0.19	217
O-N 72	6	17	0.50	0.85	70
DEC 72	14	17	0.54	0.66	22
JAN 73	-	-	-	-	-
FEB 73	14	10	0.80	0.93	16
MAR 73	-	-	0.13	0.14	8
A-M 73	-	-	0.31	0.36	16
JUN 73	14	8	0.21	0.31	48
JUL 73	11	0	0.24	0.43	79
AUG 73	14	15	0.24	0.41	71
SEP 73	0	5	0.41	0.64	56
AVE±σ	10.8±5.2	10.6±6.1	0.32±.23	0.46±.28	65±60
OVERALL					
AVE±σ	14.4±9.6	15.8±15.4	0.32±.21	0.50±.29	56±48

Summary of separation of the cyclonic edge (CE) and the indicator isotherm (22°C @ 100 m and 15°C @ 200 m), and the surface chlorophyll-a (Cl<sub>s</sub>) in the current (GS) and in coastal waters (CW). The percent difference between coastal and current chlorophyll values is computed by 100 (CW-GS)÷GS=%. Blank values are where data were not obtained or where indicator went aground.

The result implies that the current velocities must be less at higher latitudes, and this is indeed observed by Fuglister (1951) in his ship drift studies.

It is also useful to note that the average separation of the 15°C at 200 m is approximately the same as the 22°C at 100 m. If the relation between the 15°C isotherm at 200 m and the velocity core holds in these latitudes as it does off New England, then the pathlines to be discussed in section 3.2 are also pathlines of the velocity core maximum. The large standard deviations on the data in columns two and three reinforce earlier conclusions that these surface indicators of the current are complicated expressions of local wind and current conditions and should not be expected to be more precise indicators than they are. That is, for gross-scale features, they are reliable indicators (within 10-30 km) of the current's cyclonic edge, but for fine-scale analysis they may be misleading and must be used with caution. This is a fundamental limitation of remotely sensed ocean-current boundary location.

Average-surface chlorophyll-a concentrations in the current (GS) and in the coastal water (CW) are given in columns four and five of table 3.1. These values are in good agreement with those reported by Corcoran and Alexander (1963) in the Straits of Florida off Miami. Average values in the current are  $0.32 \text{ mg m}^{-3}$ , whereas the mean value was  $0.50 \text{ mg m}^{-3}$  in the coastal water. This represents an average increase of 56% in coastal water compared to that in the current. During several months of the spring of 1973, the % increase was markedly lower than in other months. Volume-scattering function values follow this trend also, which means that waters are spectrally similar and no ocean-color-sensing device could detect a boundary on the basis of color change alone. The data in the last column indicate that there is a maximum in the percent difference in the summer months, which is encouraging for remote sensing because that is when surface thermal signatures are lost.

Continuous-flow chlorophyll-a measurements were made during each cruise, including the current tracking to obtain the pathlines of the current. The general trend of surface values is not significantly different than that reported here. One exception is the summer of 1973 discussed below. Harbor and nearshore values were generally much higher than these reported here; estuarine water in general has entirely different chlorophyll and scattering values caused by suspended materials and Gelbstoff. These waters are easily distinguished in ERTS data as will be discussed in section 4.3.

### 3.2 Pathlines of the Current

Conditions prior to the first cruise are summarized in figure 3.1. These data were obtained through the courtesy of Merrill (Texas A & M University), Molinari (National Oceanic and Atmospheric Administration, NOAA), Rinkel (Florida State University System Institute of Oceanography, SUSIO), and Brooks and Niiler (Nova University) from 6 to 18 May 1972. In this composite of their data, an anticyclonic eddy is in the process of separating as evidenced by the ridge in the topography of the 22°C isotherm extending northeast from Campeche Bank to the Florida Platform. Areas where the 22°C isotherm is deeper than 125 m are stippled; the indicator isotherm is the heavy line

outlining the main flow and the eddy. Here the tracking technique would show very short radii of curvature in the zone where the separation was taking place, or the eddy could be missed entirely (if it were not for the suborbital trackline, cf., fig. 2.4). Recirculation in the eddy is already quite extensive as evidenced by the closure of the isopleths. The process of eddy separation cannot be discussed with the pathlines of the 22°C isotherm except to confirm that this did indeed occur. This eddy was observed as late as December 1972 in the suborbital trackline near the west Florida Platform.

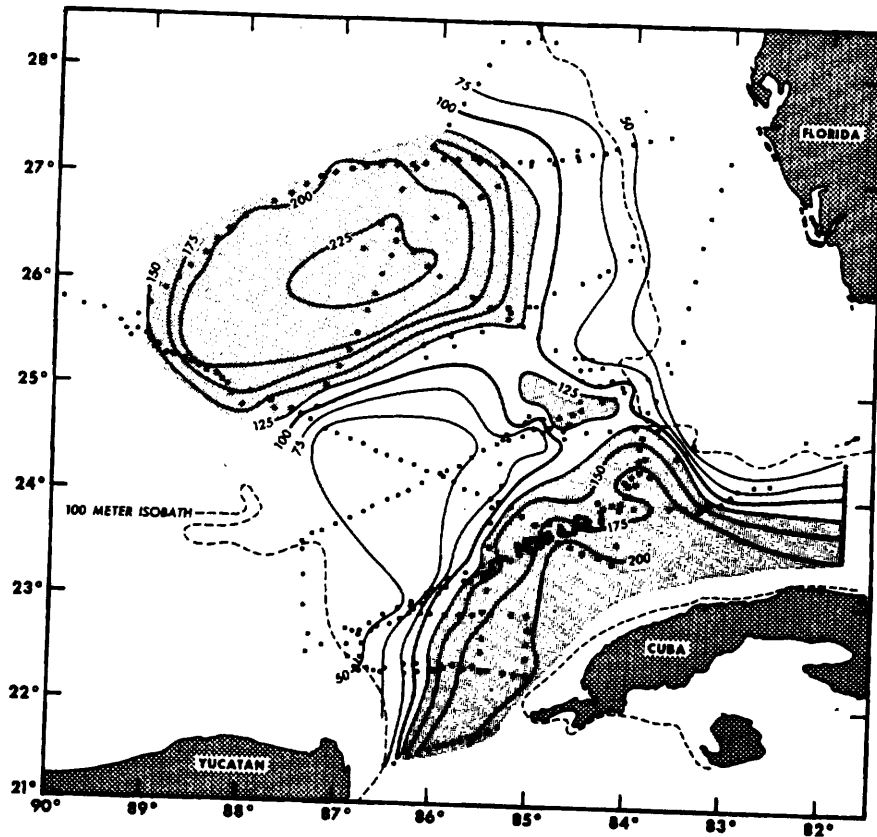


Figure 3.1 Depth of the 22°C isotherm in the project area, composited from data taken 6-18 May 1972. The eddy was actively separating from the main flow; and this figure required spatial smoothing, but it does illustrate the relation of the indicator (100-m depth contour heavy) to the thermal field. Stippled areas are where the isothermal surface was deeper than 125 m.

Pathlines of the 22°C isotherm at 100-m depth are given in figure 3.2. The series was obtained at 36-day intervals, coincidental with the 18-day period of ERTS. Dates of each survey are labeled on the appropriate pathline. The shortest tracking time was 3 days and the longest 6 days, so that near synopticity was accomplished. Hydrographic station transects of the straits added 2 to 3 days to each cruise.

By August 1972, the 22°C isotherm extended north from Yucatan and curved in a gentle anticyclonic arc, terminating tangent to the Florida Platform near Dry Tortugas (see also fig. 2.4). The suborbital trackline supports the earlier discussion that the eddy observed in May had completely separated, as evidenced by the 22°C isotherm being shallower than 30 m between the eddy and the main flow.

By September conditions had changed markedly. The initial current direction had a significant easterly component and flowed directly toward the west Florida shelf. There was evidence of Loop Current Water on the shelf, and the 22°C isotherm apparently went aground well north of Dry Tortugas. A red tide of *Gymnodinium breve* was reported on the west Florida shelf at this time. By late October the current had reformed to its southernmost extent, and evidence of Florida Bay Water flowing south through the Keys was noted in both the ship track and an ERTS image (see also fig. 4.9). Murphy *et al.* have used this evidence to document partially the source of the first reported Florida east coast red tide. It is hypothesized that the organisms were carried by the current through the Straits of Florida and exchanged with local coastal water north of Miami.

By December 1972, the current had swung to the west and had penetrated into the Gulf to the same latitude as during August. At 24°N, the stream flowed in a sharp anticyclonic turn to the east. January 1973 was the only month in which transects of the Straits were not obtained. This was caused by 25 m sec<sup>-1</sup> winds and high seas forcing the ship to turn back. Only four crossings were obtained, but sufficient detail permitted the observation that, for the first time in the series, the current penetrated north of Dry Tortugas (25°N).

The "spring intrusion" (Leipper, 1970) continued through February, March, April-May, and June when the current extended to 27°N. As the current penetrated deeper, it also swung farther to the west. North of 24°N, the isobaths curve sharply to the west, and the current flows into deeper water where different dynamics probably dominate.

A deep intrusion in July 1973, coupled with a marked cyclonic curvature off the west Florida shelf, led to expectation of an eddy separating by the following cruise. The deep intrusion from the east was not a sampling artifact; the R/V BELLOWS obtained concurrent hydrographic station data across the shelf and out into the main current throughout this area. The furthest western extent of the current also occurred in July. A vast area of green, high chlorophyll-content water was encountered along the western boundary opposite the intrusion from the east.

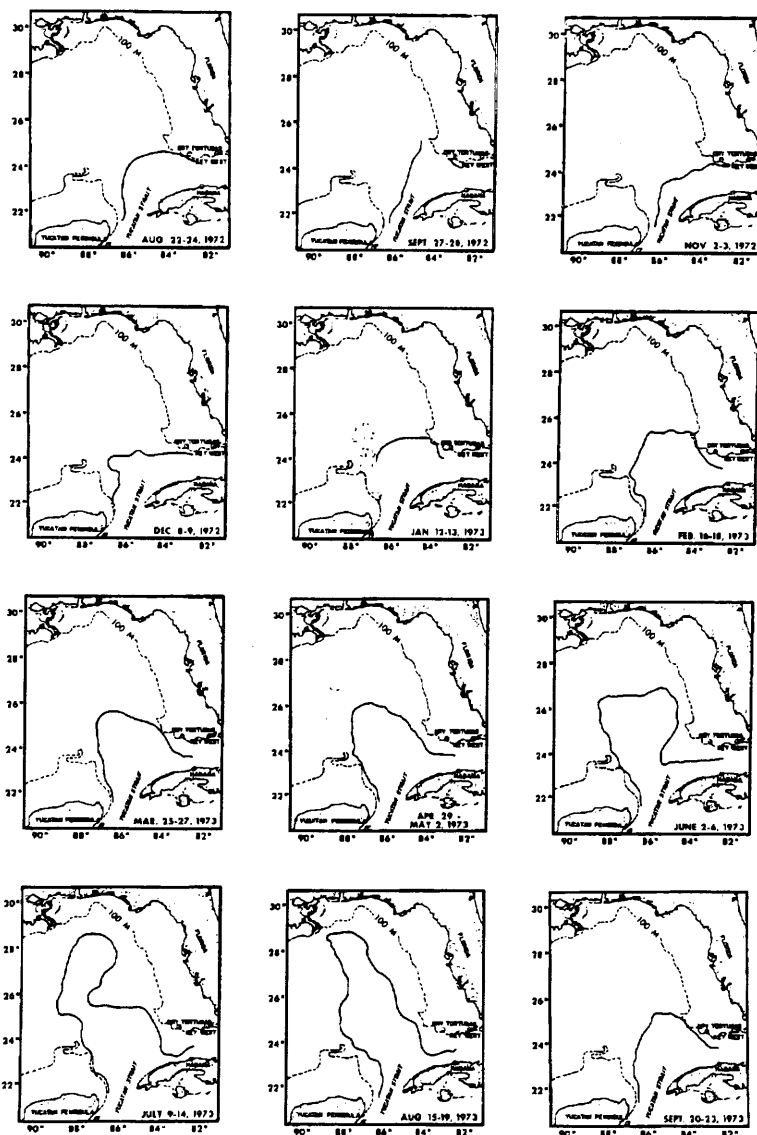


Figure 3.2 Pathlines of the 22°C isotherm at 100-m depth for the period August 1972 to September 1973. Dashed line is the 100 m isobath. Actual dates of each survey from Yucatan to Dry Tortugas, but excluding the time required for the STD sections, is given on the lower right of each figure. Sequence starts at the upper left and proceeds left to right, top to bottom.

By August 1973, the current system extended almost to the Mississippi Delta. The eddy had not separated. Very low salinity water ( $24\text{‰}$ ) was recorded by a simultaneous cruise of the R/V BELLOWS and the R/V VIRGINIA KEY all along the current edge off the Florida shelf. Surface salinities were less than  $30\text{‰}$  along the cyclonic boundary in the Straits of Florida. Because the Loop Current was so close to the Mississippi Delta and there are no other large sources of fresh water, it seems probable that this was Mississippi River Water in origin. This water has been traced as far north as Georgia where salinities were still  $32\text{‰}$  (D. Wallace, personal communication).

During the last cruise, September 1973, the current was found well to the south again, at approximately the same penetration as February. A track-line on the R/V BOWERS, from Ft. Myers west to  $87^{\circ}\text{W}$  and north to Pascagoula, confirmed that an anticyclonic eddy had indeed separated and that a significant change in the hydrography of the eastern Gulf had occurred in 1 month. There was no hint in the extensive August data that a recirculation had begun as a prelude to the eddy formation, although observations by Cochrane (personal communication, 1974), made between the April-May and June cruises, showed substantial closure in his isotherm field in this area.

These data support the possibility that the eddy separation is an annual event, but by no means does it occur at the same time each year. The May 1972 eddy and the September 1973 event are 16 months apart, whereas spacecraft data, supported by recently obtained buoy tracks (W. S. Richardson, personal communication), suggest that an eddy had separated in April 1974, a 7-month time difference. Other eddies have separated in November 1970, and one again in July or August 1971 (J. Brucks, personal communication). Thus in each of the last 5 years, between the vernal and autumnal equinoxes, an anticyclonic eddy appears to have separated from the main current.

In figure 3.3, the northward penetration of the  $22^{\circ}\text{C}$  isotherm into the Gulf is compared with historical data. The dashed line is Fuglister's harmonic fit of annual and semiannual terms to ship drifts in the Straits of Florida. The solid line is Niiler and Richardson's (1973) fit of a sinusoid, with an annual term only, to the direct transport measurements in the Straits of Florida. The light line with triangles is the fit of the arc distance from Cabo San Antonio to the pathlines of the indicator. Cochrane (1965) did an analysis similar to Fuglister's and showed that the ship drifts in the western Yucatan Strait are essentially the same as in the Straits of Florida, except that the maximum drift through Yucatan leads that through Florida by 1 month. Niiler and Richardson's curve shows the same general feature of low transports in winter and high transports in summer. They noted that the week-to-week fluctuations in the current were as much as the annual range, and further that the transports lag the annual cycle of wind stress curl over the Atlantic Ocean by 4 months. Maul (1974) reported that the slope of the  $17^{\circ}\text{C}$  isotherm in the Yucatan Strait lagged the penetration by three to four cruises. The general agreement between the three curves in figure 3.3 suggests that the variations in the Gulf Loop Current are well correlated with the annual cycle of current velocity and transport. The annual cycle of current velocity is in phase with the annual cycle of trade wind stress (Fuglister, 1951).



These data form the basis upon which Leipper's suggestion has been investigated. The pathlines indicate that: (a) There is an annual cycle of growth and decay of the Gulf Loop Current, (b) a major exchange of heat, salt, and momentum from the current into the Gulf is made at least once a year through the separation of an anticyclonic eddy or current ring, and (c) the circulation in the eastern Gulf of Mexico is associated with the annual cycle of mass transport.

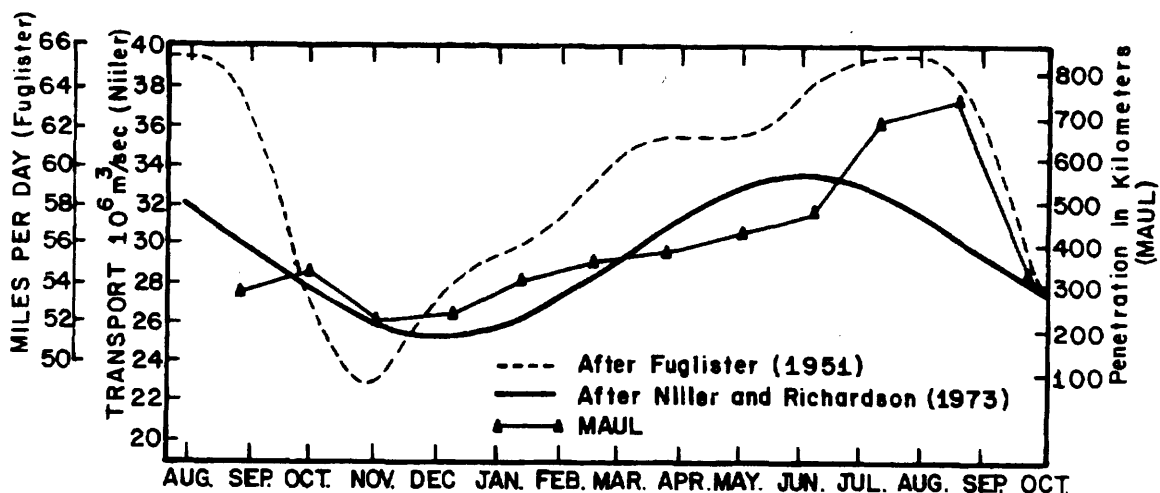


Figure 3.3 Annual cycle of surface drift velocity in the Straits of Florida between Cape Florida and  $30^\circ\text{N}$  (dashed), annual cycle in direct transport between Miami and Bimini (solid), and annual cycle of penetration of the Gulf Loop Current into the Gulf of Mexico (triangles) during 1972-73. The large decrease in penetration between August and September (right-hand side) represents the separation of an anticyclonic eddy and is a discontinuity in the penetration pattern.

### 3.3 Theoretical Relationship between Surface and Subsurface Fronts

The statistical relationship between surface and subsurface indicators discussed in section 3.1 allows an interpretation of the pathlines discussed in section 3.2 in terms of satellite ground truth. The average separation of the surface and subsurface fronts and values of the Coriolis parameter imply specific current velocities in a geostrophically balanced system. Hansen and Maul showed that the horizontal distance between the maximum temperature gradient at 200-m depth and the maximum temperature gradient at the sea surface varied with curvature in the Gulf Stream meanders off Cape Hatteras. For anticyclonic curvature, the separation averaged  $16.2 \pm 13.4 \text{ km}$ ; for cyclonic curvature, the distance was  $11.3 \pm 8.1 \text{ km}$ ; and for inflection points,  $14.2 \pm 9.7 \text{ km}$ . Even though the standard deviations ( $\pm\sigma$ ) are large, the conclusion from the  $t$  test is that the different values are statistically significant at the 95% confidence level.

To investigate the variability in separation of the surface front to the 200-m front, consider an unaccelerated, two-layer, frictionless model with the lower layer (2) at rest. The equations of motion for the upper layer (1) in natural coordinates are:

$$\begin{aligned} \frac{dV}{dt} + g\epsilon \frac{\partial D}{\partial s} &= 0, \\ KV^2 + fV + g\epsilon \frac{\partial D}{\partial n} &= 0, \end{aligned} \quad (3.1)$$

where  $g$  is gravity,  $\epsilon \equiv \frac{\rho_1 - \rho_2}{\rho_2}$ ,  $\rho$  is density,  $D$  is the thickness of the upper layer,  $\vec{s}$  is the along-stream coordinate, and  $\vec{n}$  is the cross-stream coordinate taken positive to the left of the velocity vector facing downstream. The radius of curvature ( $1/K$ ) is typically 100 km in the Gulf Stream meanders, reported on by Hansen (1970), and is positive for cyclonic curvature. Using (3.1) at a mean latitude of  $39^\circ$ , Hansen and Maul's data show that the average velocity in the anticyclonic turns is  $155 \text{ cm sec}^{-1}$ ,  $149 \text{ cm sec}^{-1}$  in the inflections, and  $158 \text{ cm sec}^{-1}$  in the cyclonic turns. The significance of curvature is apparent when the geostrophic velocities ( $k=0$ ) are computed:  $129 \text{ cm sec}^{-1}$  in the anticyclonic and  $185 \text{ cm sec}^{-1}$  in the cyclonic meanders, or approximately  $\pm 16\%$  error, respectively.

The relatively constant velocity at first glance seems at variance with the drogue studies of Parker (1972) and Chew (1974). In both of these studies, drogue velocities decreased in anticyclonic turns and increased through the inflection points into the cyclonic turns. In Parker's work, however, as the velocity decreased, the drogues were found far ( $>20 \text{ km}$ ) to the right of the Gulf Stream's velocity core (as indicated by the  $15^\circ\text{C}$  isotherm at 200 m; Fuglister and Voorhis, 1965), and they sped up again in the cyclonic turn as they drifted over to the indicator isotherm. Similarly in Chew's Gulf of Mexico data, the deceleration in anticyclonic turns was associated with the drogues being to the left of the  $22^\circ\text{C}$  isotherm at 100 m; accelerations in inflections found the drogues to the right of the indicator isotherm. These velocity changes are consistent with the possibility of a statistically constant velocity in the core, but the velocity core is not a streamline.

The intersection with the sea surface of the density discontinuity in a two-layer model is analogous to the surface-temperature gradient maximum and/or surface-color change zone in the ocean. As a first approximation, a constant velocity of  $150 \text{ cm sec}^{-1}$  is used to study the effects of curvature and latitude on the separation between the surface front and the front at 200-m depth. From Nowlin and McLellan's (1967) data,  $\rho_1$  is conservatively chosen to be 1.0255 and  $\rho_2 = 1.0265$ . Results for the latitudes of the Gulf of Mexico are given in figure 3.4.

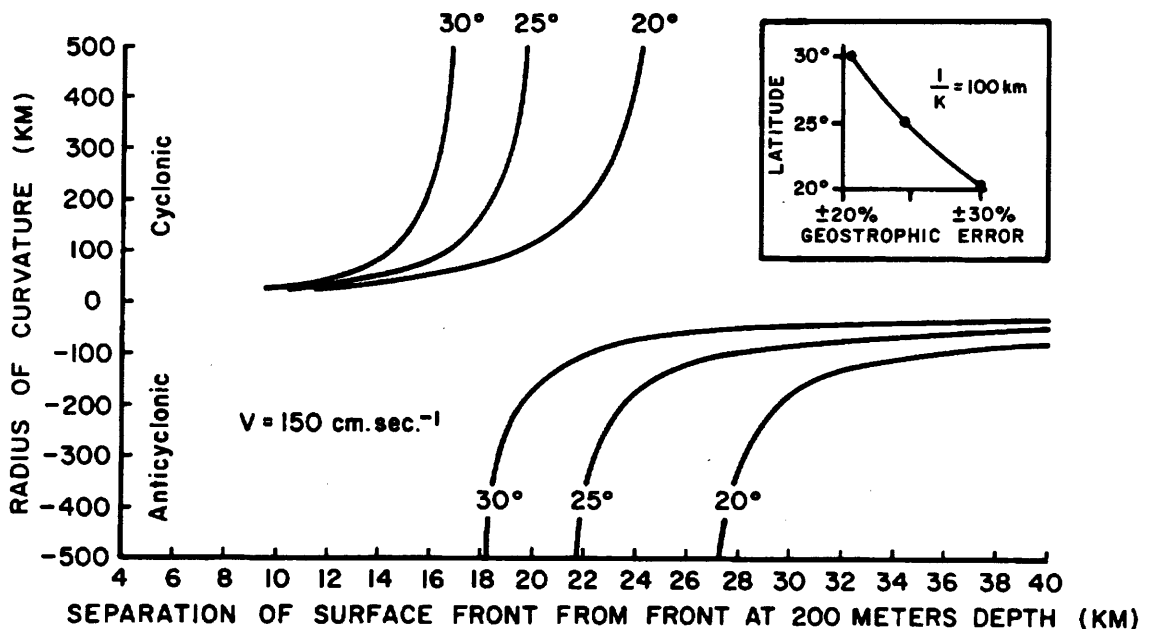


Figure 3.4 Theoretical separation of surface front from the front at 200-m depth versus the radius of curvature of Loop Current meanders. The curves are given for the bounding latitudes of the Gulf of Mexico ( $20^\circ$ ,  $25^\circ$ , and  $30^\circ$ ) and are for a velocity core speed of  $150 \text{ cm sec}^{-1}$ . Inset is the error introduced by assuming the geostrophic approximation as a function of latitude for a  $K=10^{-7} \text{ cm}^{-1}$ ; the error values are approximately symmetrical, but not exactly as seen in the main drawing.

Separation between the surface front and the 200-m front is a non-linear function of the radius of curvature and is inversely proportional to latitude. For large cyclonic curvature, the interface steepens. Conversely, the interface becomes very flat for the same curvature in the anticyclonic case. That is, for the same interface slope (pressure gradient) when the centripetal and Coriolis terms are additive (cyclonic curvature), the velocity will be less than for the anticyclonic case. The inset in figure 3.4 depicts the meridional dependence on the geostrophic approximation in meandering flow for a 100-km radius of curvature; this error becomes asymmetric for smaller radii. These results emphasize the need to account for curvature in interpreting maps of dynamic topography particularly in lower latitudes.

Typical amplitudes ( $a$ ) for meanders in the Gulf Stream system are 50 km; wavelengths ( $\lambda$ ) are characteristically 400 km (Chew, 1974; Hansen

(1970). Using these values and assuming a sinusoidal meander path, the effect of curvature on the separation between the satellite-sensed front and the front at 200-m depth can be studied. Curvature is calculated along the meander by

$$K = - \frac{a k^2 \sin k n}{(1 + a^2 k^2 \cos^2 k n)^{3/2}}, \quad (3.2)$$

where  $k \equiv 2\pi/\lambda$  and  $n$  is defined as before. Using (3.1) and (3.2), the curvature and the separation along the geodesics to the meander path can be computed. Figure 3.5 depicts the variability for  $V=100, 150$ , and  $200$   $\text{cm sec}^{-1}$  at  $25^\circ$  North latitude.

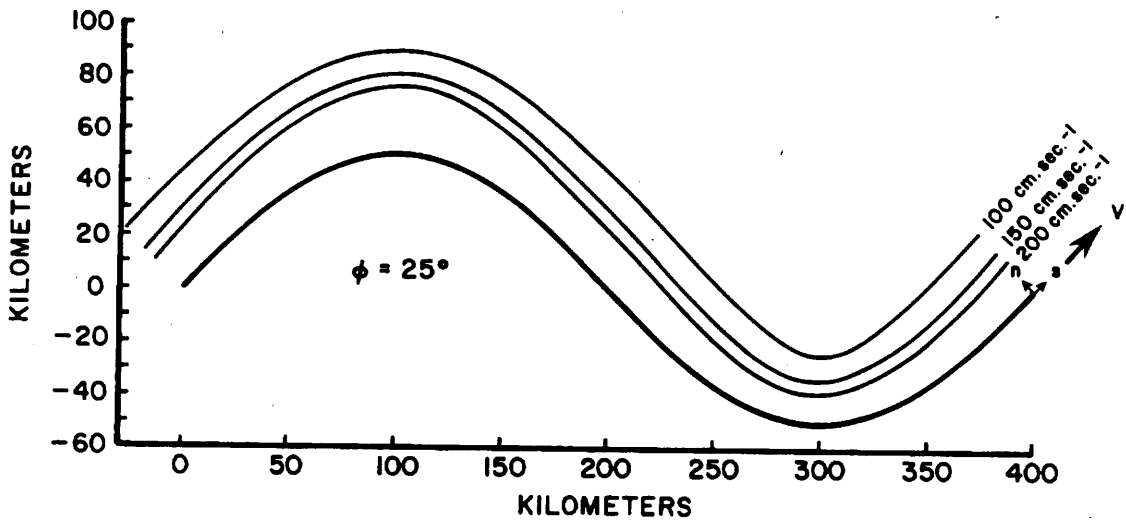


Figure 3.5 Schematic of separation of surface front from the front at 200-m depth (heavy line) as a function of curvature and velocity along a sinusoidal meander. The velocity is considered constant along  $V$  for each of the three cases.

Minimum radius of curvature for this model occurs at 100 and 300 km along the meander and is 81 km. The heavy line with the arrow in figure 3.5 is the meander pathline, and the other lines represent the location of the surface front with respect to the velocity core. Average separation for all velocities is 30.4 km in the anticyclonic turn. The minor effect of variations in the Coriolis parameter along the pathline (4%) have been neglected here; from figure 3.5, it is seen that  $\frac{\partial f}{\partial y}$  would reduce the anticyclonic separation and increase the cyclonic separation. The net effect is to reduce the pathline variability in the separation for an east-west oriented meander, and to do so more strongly at higher latitudes.

In summary, the distance from the satellite-sensed cyclonic edge to the current core will have typical separations of 26 km in the cyclonic turns and 39 km in the anticyclonic turns during the autumn and early winter when current velocities are a minimum of  $100 \text{ cm sec}^{-1}$ . During springtime when velocities have increased to  $150 \text{ cm sec}^{-1}$ , the corresponding values are 16 km in the cyclonic turns and 30 km in the anticyclonic turns. During the maximum velocities, which Fuglister (1951) and Cochran (1965) report to be mid-summer, the values are 11 km and 26 km for the cyclonic and anticyclonic turns, respectively. The average theoretical separation is 22 km, which is somewhat larger than the statistical value of 15 km observed in the straits; the latter value may be smaller because of channeling effects.

For practical applications, such as optimizing marine transportation, the average separation of the satellite-sensed current boundary and the velocity core for all current speeds is probably adequate. The large variances in the separation of the surface front and the indicator isotherm (table 3.1) suggest that factors other than curvature are important. The satellite data, which are discussed in the next sections, are useful in providing synoptic observations of the current, but they are limited in providing details of some aspects of the flow patterns. This underscores the aphorism that remote sensing is an ancillary technique for studying ocean physics.

#### 4. RADIATION OBSERVATIONS

This section is devoted to analyzing the physics of the variables which relate to the satellite observations. First, the theoretical effect of the surface contribution to the upwelling radiance observed by ERTS is discussed and the importance of sea state is exemplified. Shipboard observations of ocean spectra are then studied to understand how different water types behave when integrated over the spectral response of the multi-spectral scanner's several channels. Next, actual ERTS observations are presented, and the technique for extracting useful oceanic information from the digital data by computer enhancement is discussed. Last, unexpected ERTS and Skylab data are used to show evidence of fine-scale features embedded in the current, as viewed by surface glitter patterns.

##### 4.1. Theoretical Effect of Sea State on Upwelling Light

Equation 2.1 identified three components to the radiation received by a satellite: diffuse radiation from beneath the sea, atmospheric radiation which is mostly scattered light, and the radiation reflected from the sea surface itself. Because the surface component to  $N$  can dominate the scene (i.e., sunglint), sea-state effects on upwelling spectral irradiance must be investigated.

Let  $\rho(\theta)$  be the Fresnel reflectance from a calm surface where  $\theta$  is the zenith angle (angle of incidence). Then the total reflectance ( $\rho$ ) from the ocean's surface, in the absence of foam, white caps, and glitter, is given by:

$$\rho = \frac{\int_0^{2\pi} \int_0^{\pi/2} \rho(\theta) N_a \sin\theta \cos\theta d\theta d\psi}{\int_0^{2\pi} \int_0^{\pi/2} N_a \sin\theta \cos\theta d\theta d\psi}, \quad (4.1)$$

where  $N_a$  is the radiance of the atmosphere, and the integration is over  $2\pi$  Steradians ( $\theta, \psi$ ). Even though  $N_a$  is strongly dependent on wavelength, Sauberer and Ruttner (1941) have shown that for zenith angles less than  $40^\circ$ ,  $\rho$  is essentially nondispersive; therefore, Anderson's (1954) value of  $\rho=0.03$  is adopted for zenith angles  $\leq 40^\circ$ , and it is assumed constant for the 400- to 700-nm interval of interest. The upwelling irradiance from the ocean above the sea surface ( $H(0,+)$ ) is the sum of the diffuse component from beneath the surface ( $R_d H(0,-)$ ) and the surface component ( $\rho H(0,-)$ ).

Cox and Munk (1954) have shown that for solar zenith angles less than  $70^\circ$ , Fresnel's law is valid in a Beaufort 4 wind ( $\sim 8 \text{ m sec}^{-1}$ ). As white caps and foam cover larger areas of the sea surface, however,  $\rho$  will be altered because these features are approximately Lambertian, nondispersive, and have an albedo

of 1; thus, they contribute uniform irradiance above the surface ( $f H(0,-)$ ) where  $f$  is the fraction of the sea covered by these diffuse reflectors. Therefore:

$$H(0,+) = R_d H(0,-) + (\rho(1-f) + f) H(0,-). \quad (4.2)$$

The computed spectrum of upwelling irradiance for solar zenith angles less than  $40^\circ$  as a function of  $f$  for the data in figure 2.2a is given in figure 4.1. To be consistent, the values of  $H(0,-)$  observed by Tyler and Smith (1970) in the Gulf Stream at  $25^\circ 45' N$  on 3 July 1967 are used.

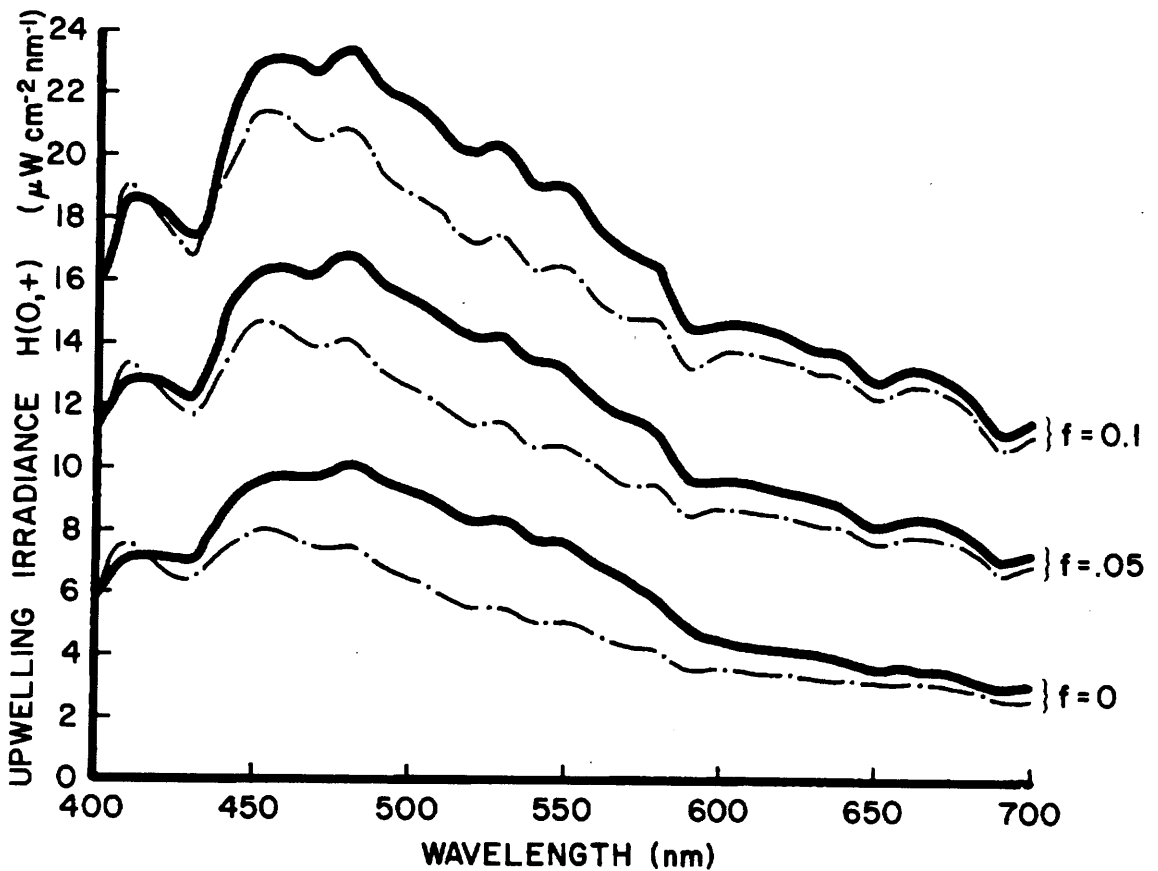


Figure 4.1 Theoretical spectra computed for three fractions of the sea surface covered with white caps, foam, or specular reflectors. Solid line uses the ratio of particle scattering to water-only scattering of 128; dashed line uses 32 for the ratio. Absorption coefficients used were 0.01 and 0.001 for the solid and dashed lines, respectively. This represents summer (low solar-zenith angle) conditions at the latitude of the Gulf of Mexico.

Upwelling irradiance values for  $f=0$ , 0.05, and 0.1 are given for the coastal water case (solid line) and the Gulf Stream (dashed line). Compare the spectrum where 10% of the sea is covered and the spectrum where no white caps or foam are present. Not only has the intensity changed, but the shape is also altered. The solar spectrum is fairly flat in the visible region:  $H(0,-) @ 550 \text{ nm} \div H(0,-) @ 650 \text{ nm} \approx 1.2$ . High sea states, which reflect non-selectively, will add relatively more long wavelength energy to the upwelling irradiance. Clark *et al.* (1970) have attempted to minimize these effects in the measurement of ocean spectra from aircraft by observing the ocean at Brewster's angle (directed away from the sun) through a polarizing filter. The degree to which these calculations effect their result is not known. For ERTS, the MSS views the earth at angles  $+5^\circ$  from the nadir without polarizing filters. The sun's glitter affects the upwelling radiance (Strong, 1973), and this is a function of the solar declination. Similarly, sea-state effects on the upwelling spectra change the radiance in an MSS band.

In figure 4.2a, the irradiance is plotted as a function of  $f$  for the central wavelength of the ERTS MSS band 4 (500-600 nm) and band 5 (600-700 nm). The curves are linear as expected from (4.2) and are wavelength dependent. At 550 nm, the irradiance increases more quickly with  $f$  than at 650 nm. This is caused by the shape of the solar spectrum and the ratio discussed above. In figure 4.2b is plotted the irradiance ratio  $H(0,-) @ 550 \text{ nm} \div H(0,-) @ 650 \text{ nm}$  as a function of  $f$ . The ratio decreases rapidly as the sea state builds, but then tends to level off. Further, the ratio is not the same for the two water types chosen here, which means that sea-state effects are not only a function of the fraction of white caps, but also the optical properties of the water itself. Unless the spot size of a remote sensor is small enough to exclude white caps, the effects of sea state will not only alter the interpretation of the *in situ* optical properties of the water, but will dominate the spectral variability.

The linear dependence of upwelling irradiance as a function of the fraction of white caps ( $f$ ) suggests that a simple correction scheme for sea-state effects is possible (fig. 4.2a). At longer wavelengths ( $>700 \text{ nm}$ ), the absorption coefficient for water becomes very large, and the  $N_s(\lambda)$  component of equation (2.1) is the dominant oceanic variable. At approximately 1000 nm in the reflected infrared, the absorption coefficient for water reaches a maximum and the transmittance of the atmosphere is also a maximum. If  $N_a(\lambda)$  can be obtained or reduced to a standard value (e.g., Curran, 1972), then an absolute measure of  $N$  at 1000 nm provides a measure of  $f$  in a cloud-free atmosphere.

Several investigators have proposed using the radiant energy at a few wavelengths to infer concentrations of chlorophyll-a in multispectral scanner outputs (Szekiela, 1973), in differential radiometers (Arveson, 1972), from slopes in aircraft spectra (Clark *et al.*, 1970), and in photographs (Baig and Yentsch, 1969). From the above discussion, it is seen that such ratios, differences, and slopes are strongly influenced by sea state; this factor was not considered in their work. The problem is further complicated because  $R_d$  is also dependent on  $w_0$  and  $B$  (equation (2.5)), as will be discussed in the next section.



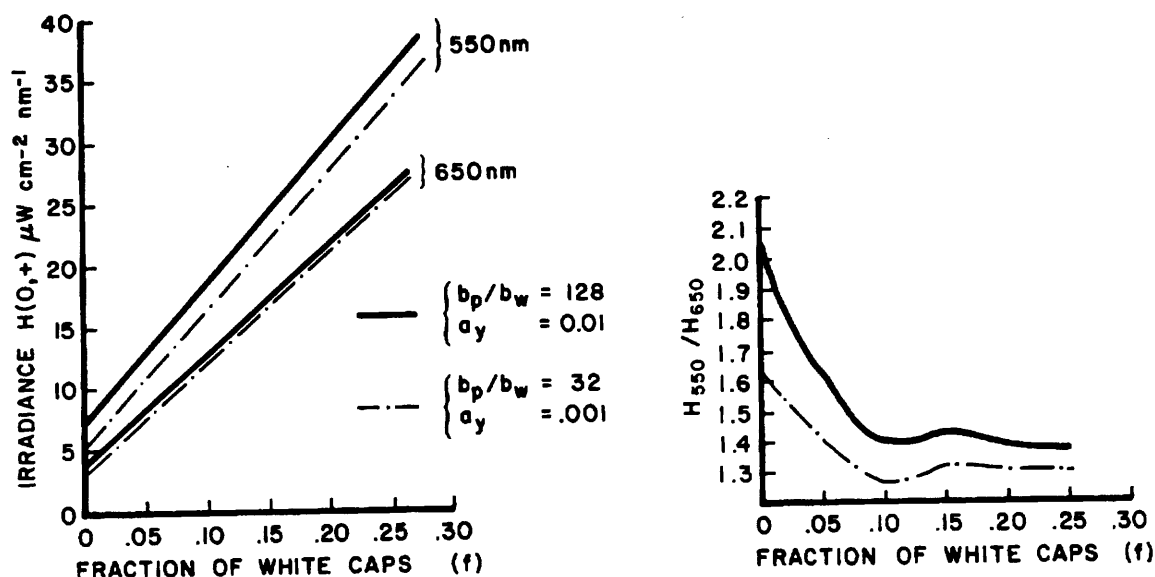


Figure 4.2a (left): Upwelling irradiance in the ERTS MSS-4 (550 nm) and MSS-5 (650 nm) intervals as a function of sea state for the two water types used in figure 4.1. Solid and dashed lines are as in other figures. Figure 4.2b(right): Irradiance ratio as a function of fraction of surface reflectors. The ratio is seen to be a function of both water type and sea state.

#### 4.2 Spectroradiometer Observations

Optical properties of the ocean, as they relate to the upwelling spectrum, must be understood at the sea surface before ERTS data can be interpreted. Upwelling irradiance from 3 m above the surface given in figure 4.3 was observed using the same  $\frac{1}{4}$ -m Ebert spectroradiometer used for the reflectance spectra in figure 2.2b. These observations were made during the time frame of figure 4.8 and represent the water types shown in that ERTS image. All spectra were carefully selected to represent approximately the same downwelling irradiance, sea state, sun angle, cloud cover, and absence of bottom influence. Specular reflection caused by waves was minimized by preselecting 10 spectra with similar shapes that did not contain anomalous random peaks. After digitizing the records, averages and standard deviations ( $\sigma$ ) were computed at 7-nm wavelength intervals; if values exceeded the average by  $1\sigma$ , they were rejected and a new mean computed. Absolute values of the spectra are traced to NBS through the 2-m integrating sphere at NASA's Goddard Space Flight Center; reported values have  $\pm 3\%$  error band (L. Blaine, personal communication).

The data in figure 4.3 can be used to interpret ocean color as measured by the multispectral scanner. The energy in an ERTS MSS band at the sea surface is

$$N(0,+) = \int_0^{\infty} \phi(\lambda)N(\lambda)d\lambda \quad , \quad (4.3)$$

where  $\phi(\lambda)$  is the filter function of the multispectral scanner;  $N$  is in units of  $\text{watts cm}^{-2}\text{sr}^{-1}$  and  $\phi$  is approximately a gate function for each MSS band ( $\phi(\text{MSS-5}) \approx 1$  for  $600 < \lambda < 700$ , and 0 otherwise). The spectra in 4.3 are upwelling irradiance ( $H(0, +)$ ) and are related to upwelling radiance ( $N(0, +)$ ) by equation (2.2). Using equation (4.3), the spectra were integrated over the MSS-4 (500-600 nm), MSS-5 (600-700 nm), and MSS-6 (700-800 nm) filter functions to investigate the properties of these three water types as ERTS ground truth. The highest irradiance values for the Gulf Stream, coastal water, and plankton bloom all occur in MSS-4; the lowest is in MSS-6 with MSS-5 midway between. The plankton bloom is distinguished by having the highest irradiance in each channel. The coastal water has a higher irradiance in MSS-4 than the Gulf Stream, but the situation is reversed in MSS-5.

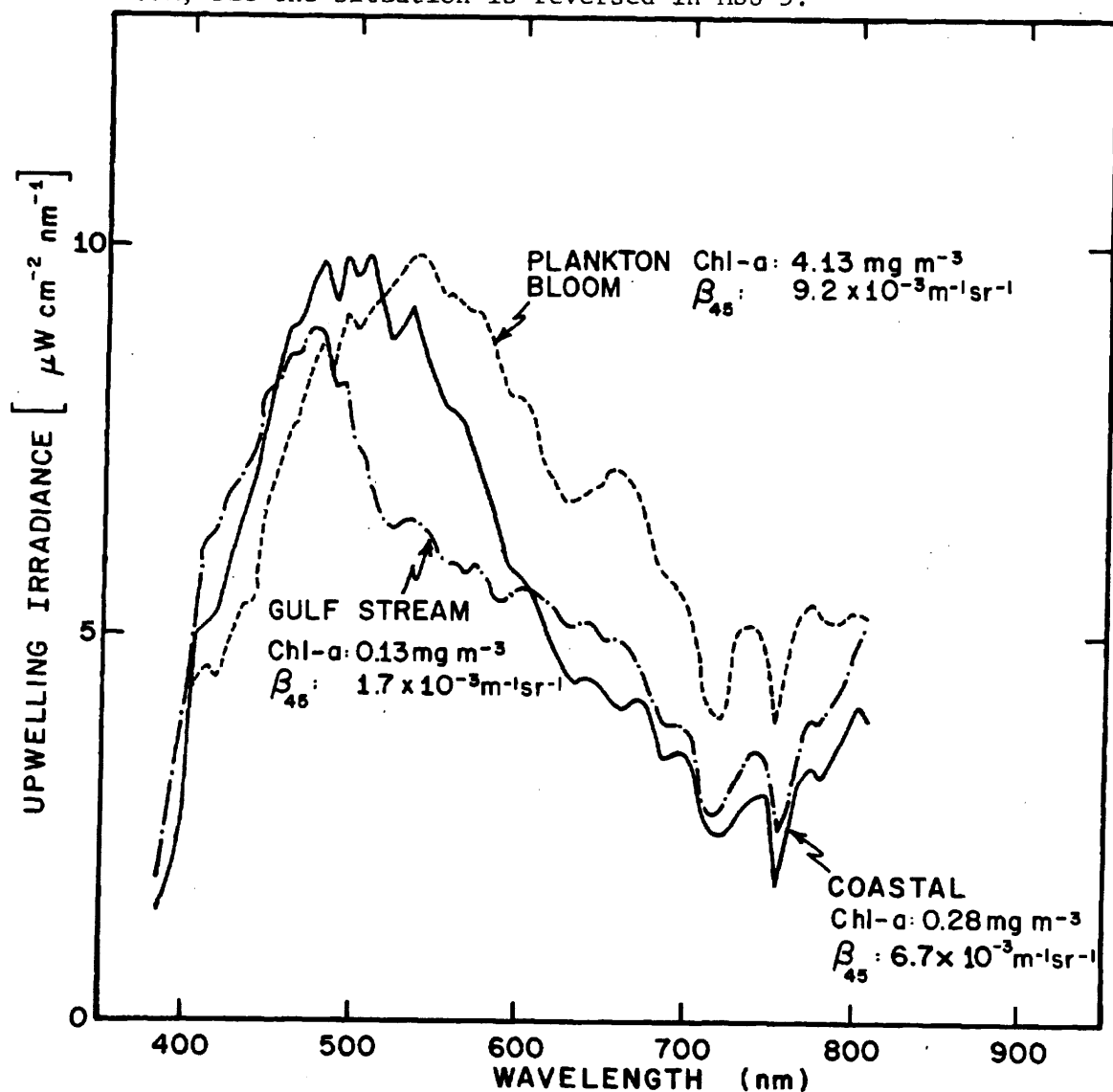


Figure 4.3 Observed upwelling spectral irradiance in the Gulf of Mexico, November 1972. The three spectra represent typical observations during the time series and show the shift of the dominant wavelength to larger values with increased surface chlorophyll-a. These spectra include the surface component  $N_s$ .

In section 4.1, the effect of sea state on using ratios and differences was discussed. To test techniques of ratios, sums, and differences on comparable spectra, a series of numerical tests were made from the integrated irradiances. Combinations of all three channels for one water type were compared with the same combinations for the other water types. It was quite easy to differentiate on the basis of such calculations between the Gulf Stream waters and the coastal waters, and between the coastal waters and the plankton bloom; however, it was not possible to distinguish between the Gulf Stream and the plankton blooms. For example,  $MSS-4 \div MSS-5$  is 1.4 for the Gulf Stream, 1.7 for the coastal water, and 1.4 for the plankton bloom. This suggests, as the theory implies (equation (2.5)), that even in the absence of sea-state changes, the ratio test ( $MSS-4 \div MSS-5$ ) is not likely to be successful in specifying the chlorophyll-a concentration.

Multispectral identification and classification of scenes is well developed in agriculture and forestry. The technique consists of clustering radiances from known targets in n-dimensional histograms, where n is the number of wavelength increment bands. Unknown targets are then "identified" by comparing the radiances in these same n-channels with the statistics of known radiances. If a value falls within a given cluster, it is considered identified within certain error bounds which vary with the statistical spread of a cluster. The data from figure 4.3 were tested in this way for ERTS channels MSS-4, MSS-5, and MSS-6 in the same manner as described above. The location of the three water types in MSS-4, MSS-5, and MSS-6 Cartesian space is plotted in figure 4.4. The circle represents the upwelling radiance from the Gulf Stream, the triangle from the coastal water, and the square from the plankton bloom. Now it can be seen graphically why the ratio test failed: Both the Gulf Stream water and the plankton bloom water lie near the same diagonal in each two-dimensional space; however, when a vector is used to identify the water types, a clear distinction can be made. The length of the vector will depend on sea state, and this result must be used with caution. The more dimensions used, the closer the vectors are to representing the spectra (Baig and Yentsch, 1969). This is an example of how clustering can be used for automatic classification of water types in the ocean. It requires first that many spectra can be observed, that surface effects be accounted for, and that in situ properties be correlated.

Clark et al. (1970) noted that the slopes of their aircraft spectra correlate quite closely with chlorophyll concentrations. They did not specify the spectral region where the slopes were calculated. The spectra in figure 4.3 have peaks at 470 nm in the Gulf Stream and at 530 nm in the plankton bloom. From the discussion in section 2.2 on the effects of  $\omega_0$  and B on  $R_d$ , it would be fortuitous if these slopes represented changes in the chlorophyll<sup>d</sup> only. There may, of course, be biogeographic regions where chlorophyll and spectra are canonically related (Duntley, 1972). However, since the data in figure 4.3 represent near-surface spectra, any ocean-color-multispectral scanner should have channels centered near 470 and 530 nm. The effect of the atmosphere (Hovis et al., 1974; Curran, 1972) is to alter markedly the upwelling radiance at satellite altitudes, particularly at shorter wavelengths (<500 nm). The fact remains that significant ocean information is contained between 470 and 530 nm, and these wavelengths must be considered along with a sea-state channel at 1000 nm.

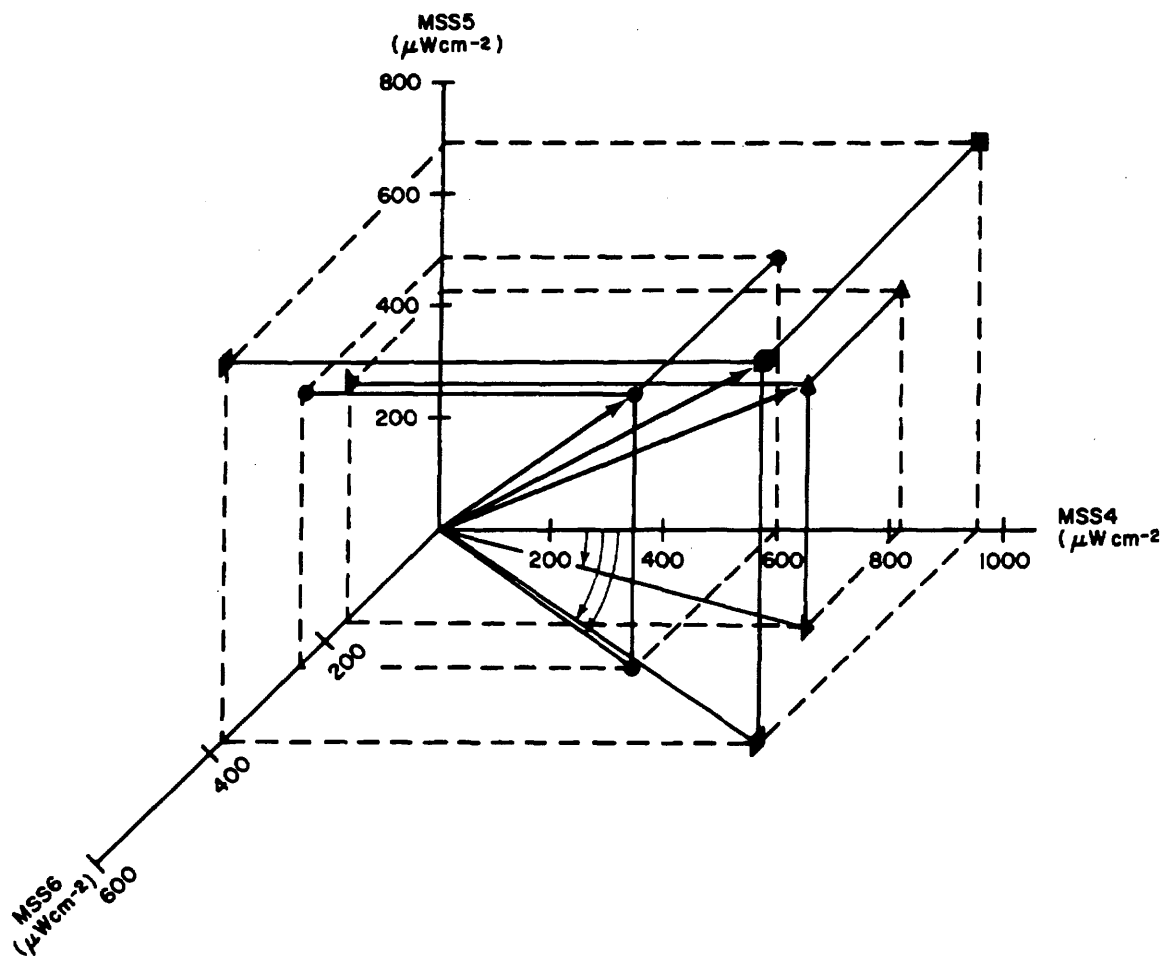


Figure 4.4 Three-dimensional clustering of the data in figure 4.3 when integrated over the filter of three MSS bands. The symbols represent the location in each of the three planes of the Gulf Stream (circle), coastal water (triangle), and the plankton bloom (square). A common location by vector can be given, with statistically derived bounds, to identify automatically a target.

The peak in the plankton bloom spectra at 675 nm (fig. 4.3) has been explained by Gordon (1974) as being caused by anomalous dispersion in the particles that causes scattering near the chlorophyll-a absorption band. The maximum in the absorption band occurs at 665 nm (equation (2.7)). The effect on the upwelling radiance is to cause the spectra to behave like the negative derivative of the absorption in the vicinity of 665 nm, i. e., a minimum in  $R_d$  occurs at 655 nm and a maximum at 675. This suggests that two very narrow channels at 655 nm and at 675 nm in an ocean color sensor would be useful in identifying plankton blooms and determining whether the absorbing pigments are in the particles or dissolved in the water.

Probably the most efficient method of determining the concentration of the constituents in the ocean will be to compare theoretical and experimental spectra, adjusting the constituent concentrations in the theoretical spectra until agreement is found. This, of course, requires a basic understanding of the optical properties of the constituents which can be derived only from careful in situ and laboratory experiments. At the present time, much energy and money are being expended for optical methods to locate and study materials with nearly unknown optical properties suspended or dissolved in a medium with only poorly known optical properties. Lack of knowledge of the optical parameters affecting reflectance must be overcome before significant progress can be made.

#### 4.3 ERTS Observations of the Gulf Loop Current

Several examples of ERTS observations of the current are given in figures 4.8 through 4.12. The location of each of these images is given in figure 4.5, which also includes pathlines of the 22°C isotherm at 100-m depth made during satellite transit. Significant variability exists in these two pathlines, only 36 days apart, which emphasizes the need for synopticity in oceanographic baseline measurements for remote sensing.

Diffuse reflectance from beneath the ocean is rarely more than 0.05 (cf., fig. 2.2). Reflectance from the ocean's surface, which is independent of this diffuse reflectance, has been shown to be comparable or even substantially larger depending on sea state. Reflectance from clouds and agricultural scenes, however, is sometimes an order of magnitude greater than from the ocean, even in the 500- to 600-nm wavelength region. For the NASA Data Processing Facility (NDPF) to produce an image for an average scene radiance, the ocean signal is compressed into the lowest few gray scales. This is clearly illustrated in figure 4.6, which is a scanline plot across the boundary of the Loop Current from the multispectral scanner. The large spikes in all four channels (MSS-4 upper) are clouds; there seems at first glance to be very little change in digital number (DN), which is proportional to radiant intensity, as a function of the sample number. Careful examination shows that the average value of the DN at samples greater than number 950 is slightly larger than those before this point. It will be shown that this marks the transition to higher radiances caused by increased sea state in the current.

To display graphically this small change over a two-dimensional region, computer enhancement is necessary. Techniques for ocean radiance levels have been studied by Maul, Charnell, and Qualset (1974), and an extension of their results will be used here. Evolution of the results to be discussed is shown in figure 4.7 a, b, c, and d. Figure 4.7 is the raw data from the original NDPF for MSS-5.

The ocean radiance from MSS-7 (800-1100 nm) is all constrained to  $0 < \text{DN} < 4$  ( $0-29 \text{ mW cm}^{-2} \text{sr}^{-1}$ ). The low radiances are caused by the very large values of the absorption coefficient of water at these wavelengths. Clouds and land (cf., fig. 4.6), however, have large near-infrared reflectance and are almost always above the DN range cited. This allows the computation of a binary mask wherein all  $\text{DN} > 4$  are set to 0 and all others are set equal to 1. The data matrix of an MSS band of interest when masked leaves only the ocean values for statistical analysis. Figure 4.7b is the mask computed for this purpose.

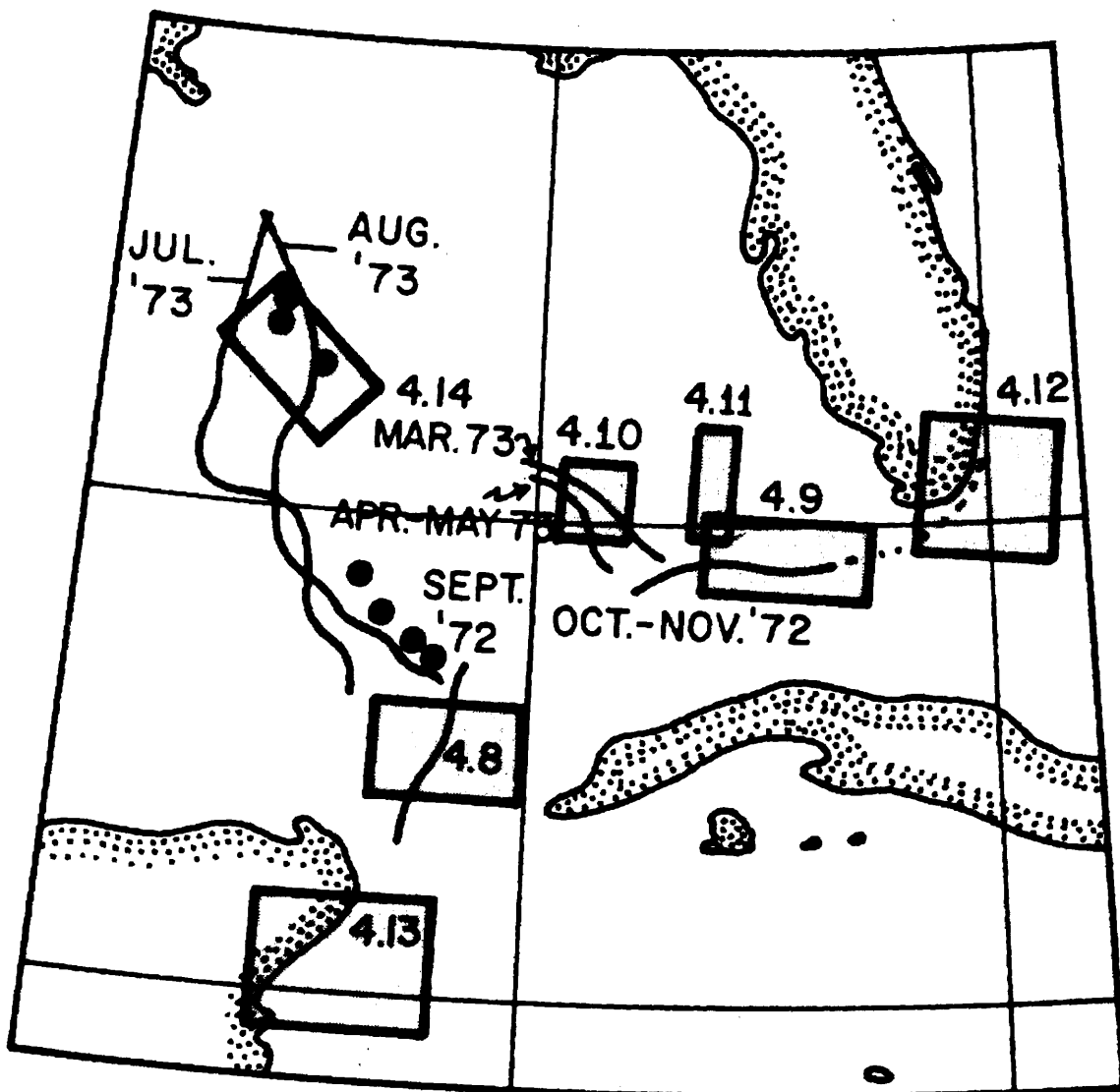


Figure 4.5 Location of observations for figures 4.8 through 4.14. The appropriate pathline for figure 4.8 is September 1972; for figure 4.9 is October-November 1972; for figure 4.10 is March 1973; for figures 4.11 and 4.12, there is no ship track; for figures 4.13 is August 1972; and for the Skylab photographs, figure 4.14, the pathlines are July and August 1973. Complete pathlines are given in figure 3.2.

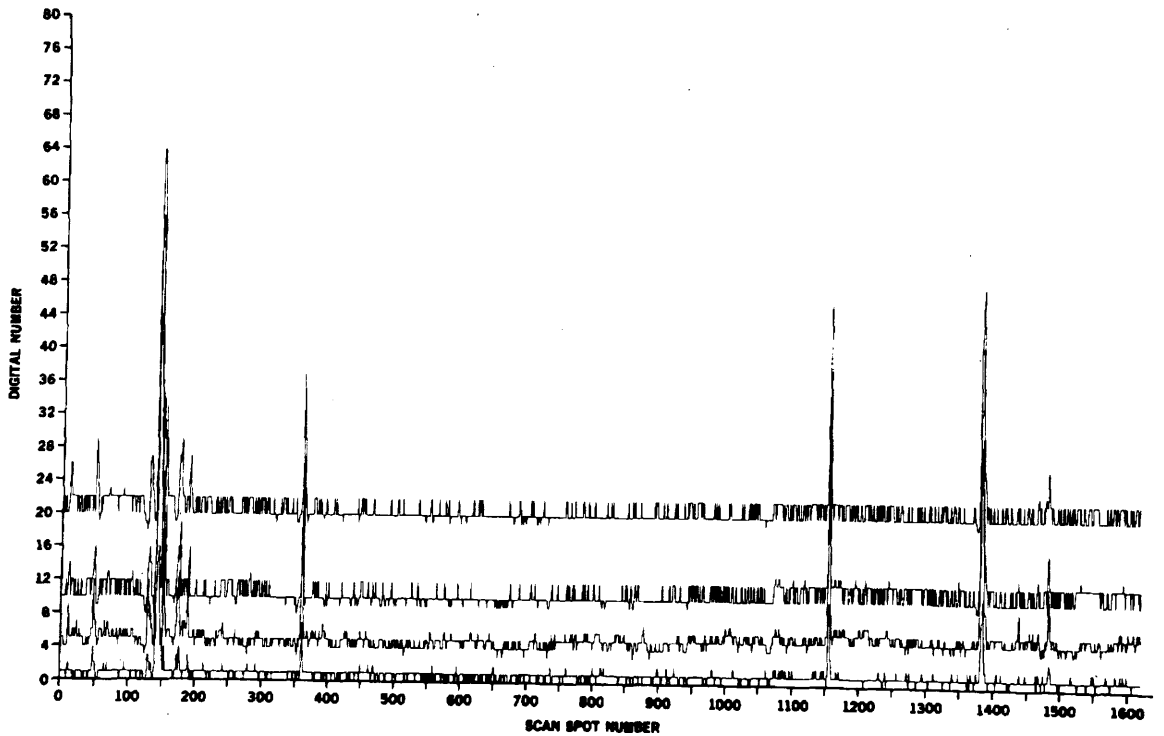


Figure 4.6 ERTS scanline plot across the Loop Current Front. Top scanline is MSS-4, next MSS-5, MSS-6, and MSS-7 on the bottom. The large energy spikes are clouds. At scan spot number 950, there is an increase in the average value of the digital number of 1 or 2; this marks the cyclonic edge of the current.

Cox and Munk (1954) have shown that the frequency distribution of ocean radiances is Gaussian to a very good approximation. Within the limits of resolution of the spacecraft data, histograms of masked MSS-4 or MSS-5 radiances are also approximately Gaussian, which is consistent with Cox and Munk's results. Gaussian properties will be used, but with the reservation that the coarse radiance quantization of ERTS over the ocean may depart from the continuous function especially at large standard deviations. The masked matrix is contrast-stretched by computing a stretch variable ( $\zeta$ ) from

$$\zeta = M \left[ \frac{(\overline{DN} + \kappa\sigma) - DN}{2\kappa\sigma} \right]^n, \quad (4.4)$$

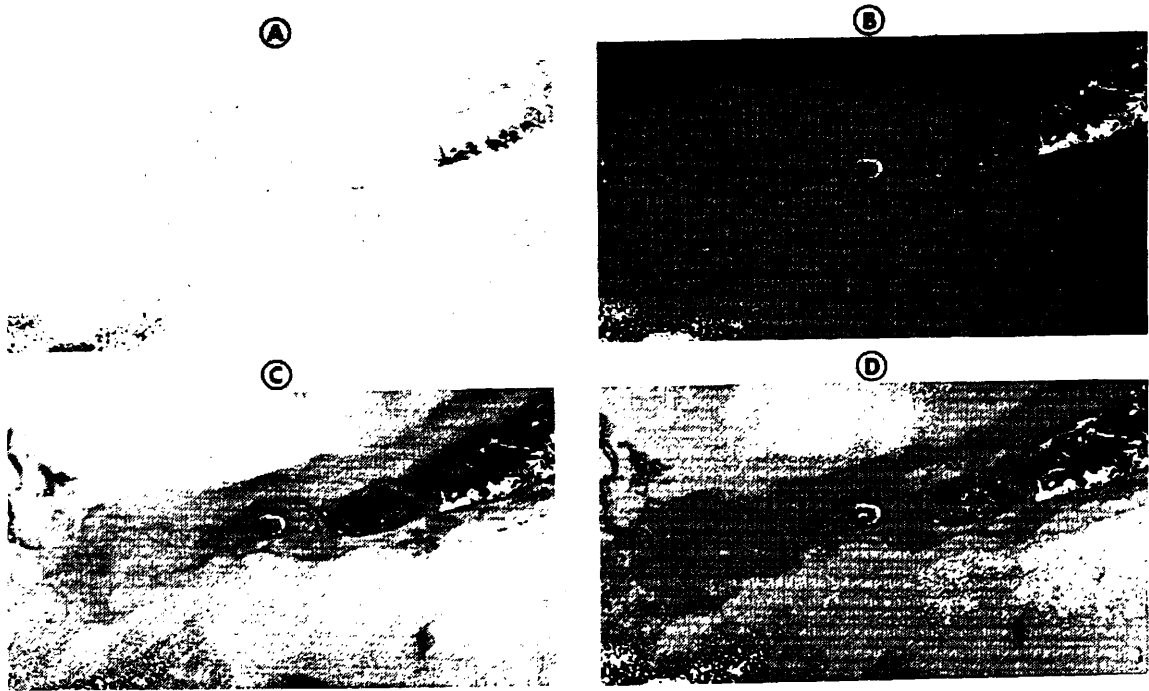


Figure 4.7a Raw data output of the NASA data-processing facility. The MSS-5 band is reproduced in the NOAA format which has an aspect ratio of 1.3 and thus is slightly distorted into the horizontal. b) Binary mask computed from simultaneous MSS-7 (reflected infrared) data. Land and clouds are set to zero; water features set to unity. c) Masking of 4.7a by 4.7b and contrast stretched according to 4.3;  $n=1$ ,  $k=2$ . Compare with 4.7a for improvement in features in the ocean. d) Application of  $19 \times 19$  Fourier filter to 4.7c. Filtering eliminates the banding in 4.7c, but reduces the spatial resolution from 100 to 1000 m.

where  $M$  is the maximum value allowed by the digital-to-analog output device,  $\overline{DN}$  is the average scene radiance,  $\kappa$  is a constant,  $\sigma$  is the standard deviation about  $\overline{DN}$ , and  $n$  is a constant. If it is desired to include 95% of the masked data,  $\kappa=2$ ; for 99%,  $\kappa=3$ , etc. All values of  $DN > \overline{DN} + \kappa\sigma$  are set to  $\overline{DN} + \kappa\sigma$ , and similarly those values of  $DN < \overline{DN} - \kappa\sigma$  are clipped. The results of stretching the data in figure 4.7a are given in figure 4.7c. The range  $7 \leq DN \leq 15$  was used here; significantly, more detail in the ocean features are clearly brought out by this technique as will be further discussed below.

Maul et al. (1974) also studied the power spectra of ERTS scanline data and were able to show that the banding in these images has significant energy at every six data samples. This is caused by the MSS design. They showed that the banding could be effectively eliminated by the use of a  $19 \times 19$  Fourier filter which was 6 db down at 10 sample points and 90% effective at 14 and 6 sample points. Results of convolving that two-dimensional filter with the stretched matrix in figure 4.7a are given in figure 4.7d. The



filtered image contains spatial changes greater than 800 to 1000 m on the Earth's surface. Note the improvement in the removal of horizontal striping and the removal of high spatial variability. These filtered images are most effectively being exploited in the coastal zone, but are not used extensively in this study as it requires several hours of computer time to perform the convolution.

Equation (4.4) produces a negative image of the input digital image. Positive whole integers  $n$  further stretch the low radiance values, but this produces a nonlinear output and must be avoided when comparing images to ocean spectra. The graphic result of using this equation on the scanline data from which figure 4.6 was taken is given in figure 4.8.

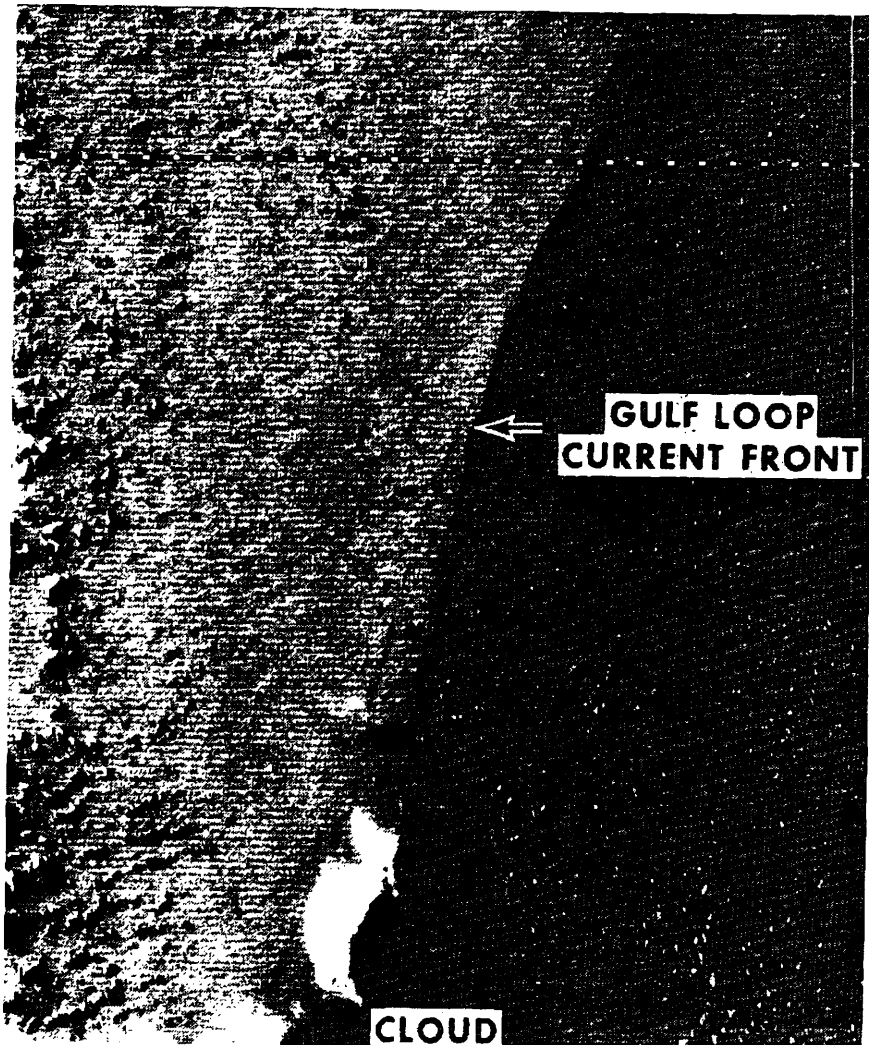


Figure 4.8 Negative print of computer-enhanced ( $9 \leq DN \leq 13$ ;  $n=1$ ) MSS-5 image of the cyclonic boundary of the Gulf Loop Current. Surface vessel track confirmed the location of the current to be the darker shade (higher radiance) region on the right-hand side of the image (ERTS ID 1065-15411). Scanline plot in figure 4.6 is taken along the dashed line in the middle of the scene. Horizontal distance across the image is 90 km.

Figure 4.8 is a negative print of the area due north of the Yucatan Straits using MSS-5 data. Computer enhancement in this image uses only five gray scales of the 128 levels available; all values below  $(DN - 2\sigma)$  are set to 127 and all above  $(DN + 2\sigma)$  are set to 0. The boundary between the resident gulf waters (left) and the current (right) is seen as a transition from light to dark tones, respectively. The exponent  $n$  was set equal to 1 for this experiment. Figure 4.9 is an enhancement of the Loop Current boundary in figure 4.7c, but which uses the MSS-4 data instead. In this negative image of the western Florida Keys, water from Florida Bay extends into the Straits of Florida and is entrained by the Florida Current. Comparing figures 4.9 and 4.7c, it is clear that more detail in the surface waters is seen in the MSS-4 image than in the MSS-5. MSS-4 can detect both absorption and scattering changes, whereas MSS-5 is essentially limited to scattering effects. The current boundary in both figures 4.8 and 4.9 was delineated by surface vessel tracks during the day of the satellite transit.

During the observations leading to figure 4.8, the winds were from the northeast at 12 to 14  $\text{m sec}^{-1}$ , whereas in figure 4.9, they were easterly at 3 to 5  $\text{m sec}^{-1}$ . When wind and waves run in opposition to a current, the waves quickly steepen, break, and generate white caps and foam on the surface. For weather conditions such as encountered during the trackline used to support figure 4.8, Ross and Cardone (1974) reported that as much as 10% of the sea surface will be covered with these diffuse reflectors. Shipboard records confirm this, but the sea state was much higher in the current than in the resident Gulf waters. The effect of these conditions on the upwelling irradiance was given in figure 4.1. Consider that the sea state in the current causes the  $f = 0.1$  spectrum and that in the resident Gulf waters is given by the  $f = 0.05$  spectrum labeled coastal water. In the MSS-5 bandpass, interval  $H(0,+)$  is larger in the current than in the coastal water; the high radiance values on the right-hand side of figure 4.8 come from the current. MSS-5 is more sensitive to small sea-state changes than MSS-4. MSS-5 then is a better choice for locating the Gulf Loop Current in the open sea because there the optical properties of the current and surrounding waters are not significantly different.

In the observations of figure 4.9, a different conclusion is drawn. Shipboard records show that the sea state was the same in both waters. Here the upwelling radiance is dominated by the  $R_d H(0,-)$  component, and the color change allows detection of the current's boundary. Thus, it is seen that the current can be detected with opposite radiance distribution depending on the dominance of surface or subsurface variables. This can work against locating the current if both sources of energy, in and out of the current, add up to the same net radiance. This means that sea-state changes the spectrum of upwelling light from the ocean, and absolute values of radiance will vary with low level winds; conversely, sea state should be estimable from radiance where the spectra are known.

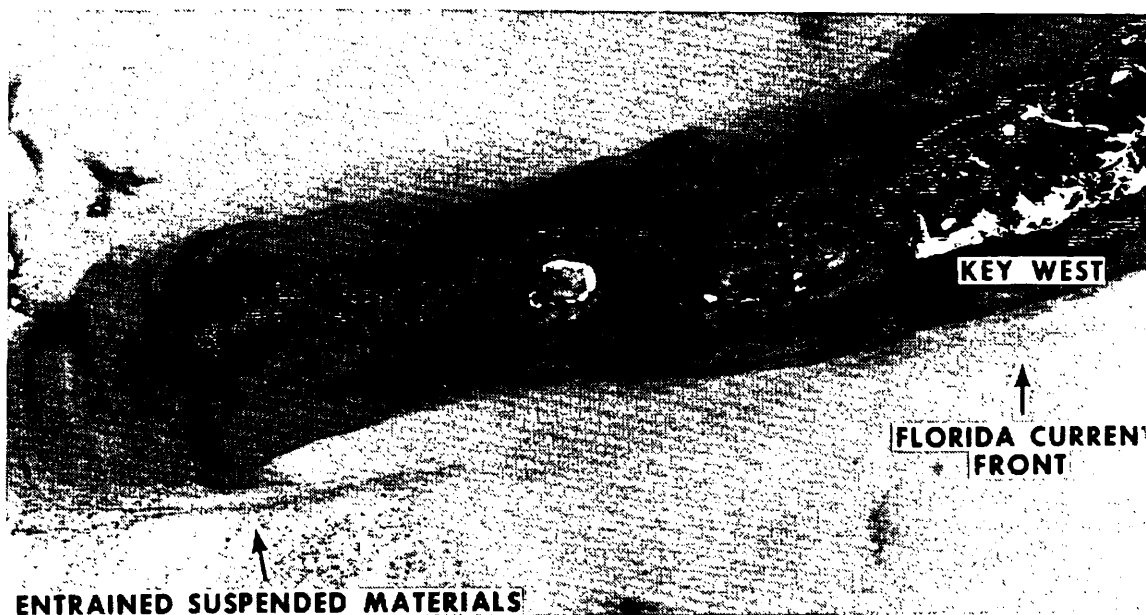


Figure 4.9 Negative print of computer-enhanced ( $12 \leq \text{DN} \leq 32$ ;  $n=1$ ) MSS-4 image of Marquesa Key and Key West (ERTS ID 1099-15293). Change in radiance southwest of Marquesa from dark to light coincides with the ship-located boundary between the higher intensity Florida Bay water and the lower intensity Gulf Stream. Bottom depth is in excess of 100 m at the cyclonic edge and does not contribute to the radiance. Horizontal distance across the image is 135 km.

Figures 4.10, 4.11, and 4.12 are important ERTS images obtained in this series for which either no vessel tracks are available or the image was obtained during the off 18-day transit. Figure 4.10 is an MSS-5 image of the current observed in the deep sea showing a double front. The fronts are approximately 10 km apart and can be seen to extend for 75 km from northwest to southeast. In this image, the boundaries appear to be made visible by two local areas of disturbed water which may represent two steps in the velocity shear profile as noted by Maul and Hansen (1972) in the Gulf Stream off Cape Hatteras. The radiance change here is quite small, one or two DN, as is the case with figure 4.8. It would be almost impossible to distinguish such streaks if there were any clouds present. Using MSS-7 to make cloud-free masks can lead to misinterpretation under these conditions because sea-state changes can sometimes be noticed in this channel. Usually sea-state values do not exceed  $\text{DN} > 4$  in MSS-7, and the condition is not serious; however, the user must be cognizant of the potential loss of ocean current information in an automatic masking scheme as outlined above.

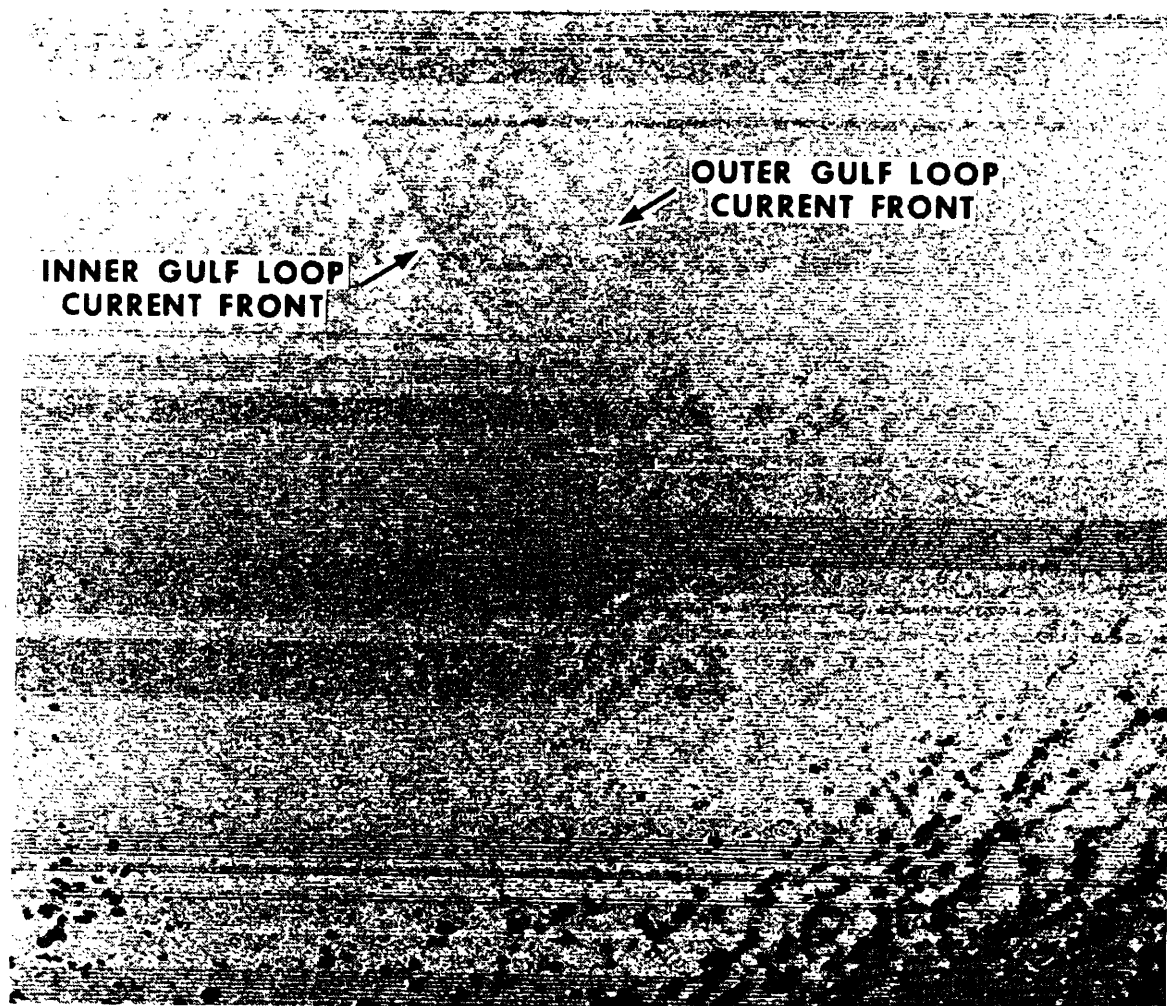


Figure 4.10 Negative print of computer-enhanced ( $10 \leq DN \leq 13$ ;  $n=1$ ) MSS-5 image (ERTS ID 1262-15355) of a double front in the Gulf Loop Current observed on 11 April 1973. This image was observed during the 18-day cycle when no ship track was obtained, but little translation of the indicator isotherm occurred between cruises. Horizontal distance across the image is 90 km.

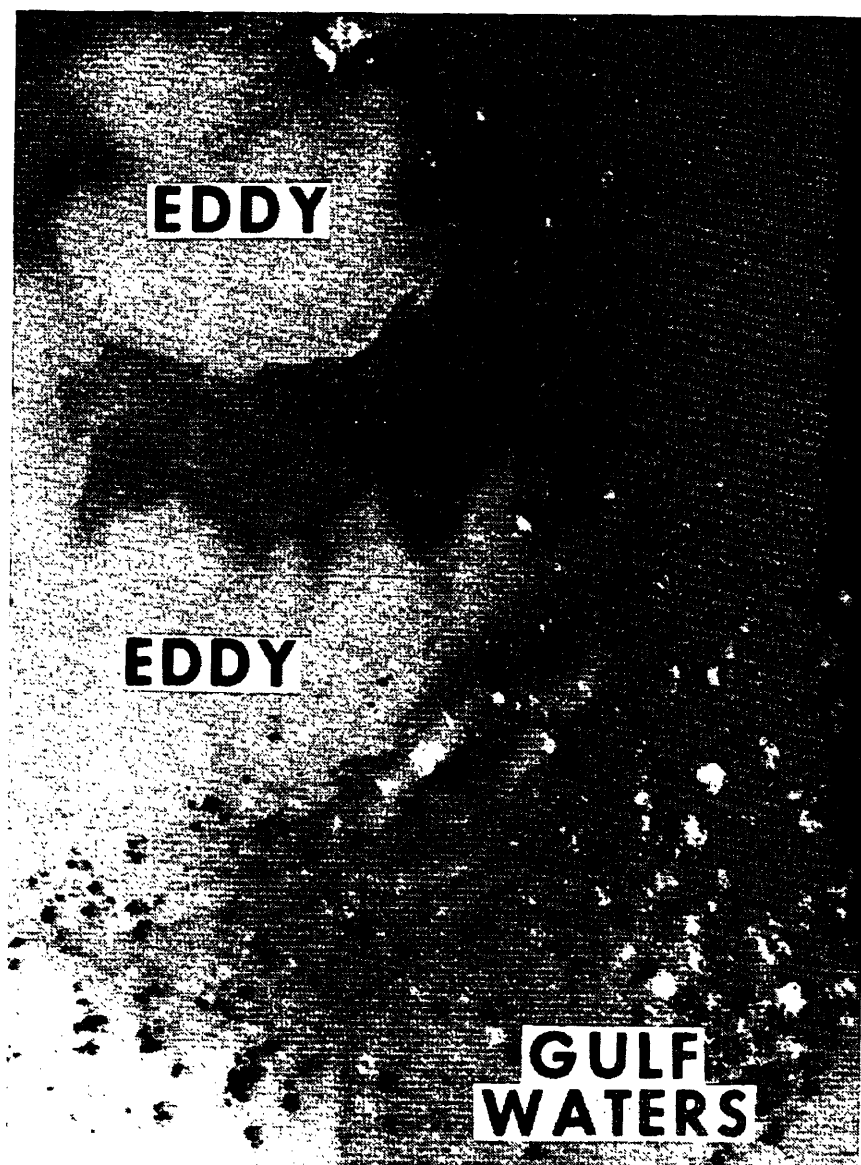


Figure 4.11 Negative print of computer enhanced ( $16 \leq DN \leq 24$ ;  $n=1$ ) MSS-4 image (ERTS ID 1153-15292) of detached eddies on the west Florida shelf observed on 22 December 1972. Details of the boundary of these 20-km diameter Gulf Loop Current eddies show significant irregularity and nonsymmetry. Horizontal distance across the image is 45 km.

In figure 4.11, an MSS-4 image of two eddies on the west Florida Platform is shown. No vessel tracks are available to substantiate this conclusion; however, on the basis that these features are not visible in any other channel, it requires that the light areas on the negative print represent blue water. Here is another example (cf., Austin, 1971) of the interaction of this scale eddy with the coastal water. Austin noted that several eddies of this 20- to 50-km range were observed around the perimeter of the current in a survey in 1970. This is the first evidence that these features drift onto the shelf where they must exchange significant quantities of salt, heat, and momentum. Eddies such as these could interact to bring cyst stages of G.breve into the photic zone and contribute to the offshore initiation of a destructive plankton bloom.

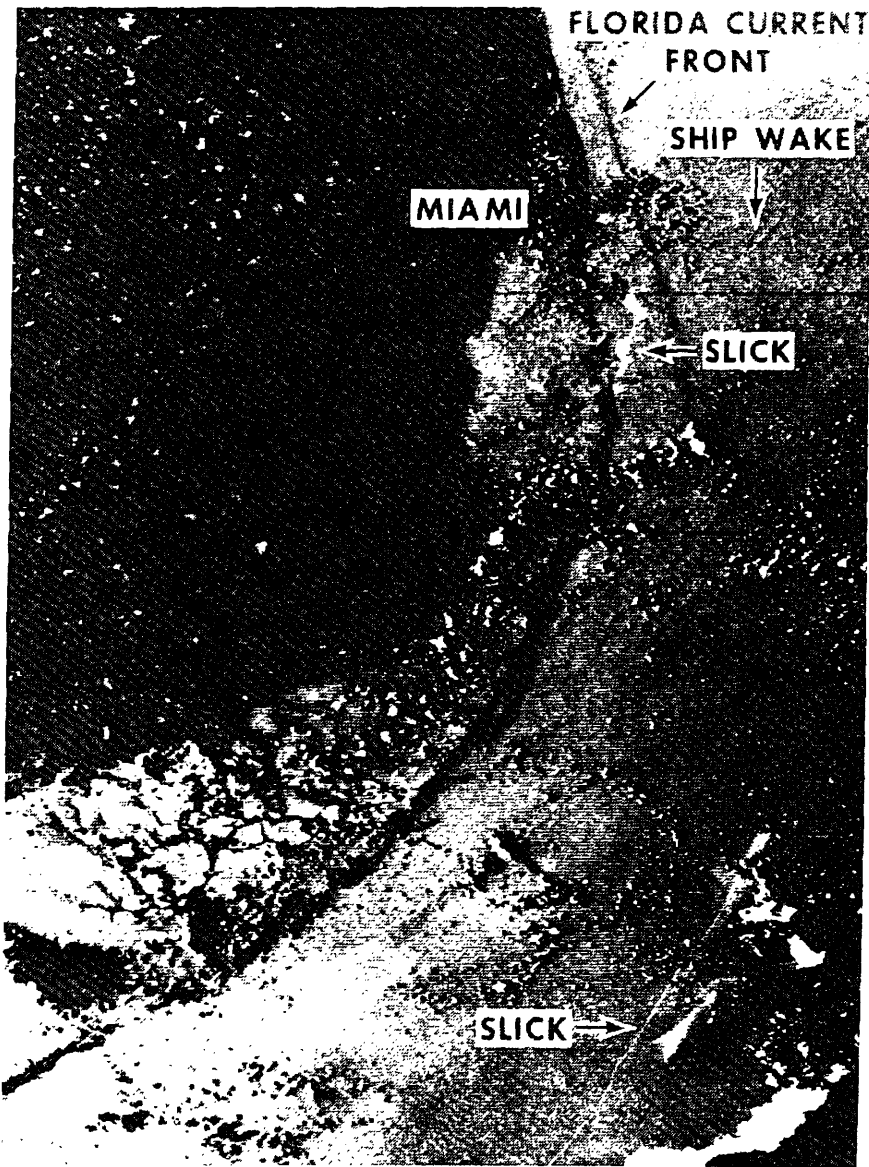


Figure 4.12 Negative print of computer-contrast-stretched ( $7 \leq DN \leq 15$ ;  $n=2$ )

ERTS image of South Florida (ERTS ID 1026-15230). The Florida Current can be seen as a line of dark lineation parallel to the coast; bottom is essentially invisible in the MSS-6 scene. A ship can be seen by its characteristic V-shaped wake just offshore of Miami Beach. Possibly the Virginia Key sewer outfall area can be observed by its low reflectance due to an organic slick. Horizontal distance across the image is 90 km.

An interpretation of coastal observations from ERTS is given in figure 4.12 which is a computer-enhanced MSS-6 negative image of southeastern Florida. The dark lineation paralleling the coast in the upper portion of the image is a zone of high reflection caused by locally increased  $N_s$  along the edge of the Florida Current. The increase in surface reflectance is probably caused by surface wave interaction with the cyclonic boundary and is not bottom influence. Another example of the dominance of  $N_s$  is the bright slick areas (low  $N$ ) off the Virginia Key sewer treatment plant. This probably is caused by the dampening of the glitter, causing capillary waves in the oil film associated with the organic slick. The slick, which appears to have drifted south past the popular Key Biscayne beaches, offers an explanation of the narrow lineation offshore in the Straits of Florida. A passing oil tanker heading south which is pumping her bilges would cause a similar feature on the image. Note that the organic slicks observed here strongly affect the upwelling radiance, and this must also affect the ratios discussed in sections 4.1 and 4.2. The glitter pattern's nonuniformities further contribute to the complication in analyzing ERTS data for quantitative results.

#### 4.4 Satellite Evidence of Fine-Scale Features in the Current

Cochrane (1965) noted that the surface velocity field of the Yucatan Current had double maxima. It was also noted by Pillsbury in 1890 in this area and by Stommel (1966, pp. 55-59) in other portions of the Gulf System. It does appear distinctly in Cochrane's geomagnetic-electrokinetograph profiles north of the Strait. Cochrane postulated that it occurs when the cyclonic edge of the Yucatan Current is found against the Mexican coast, and the main flow is bifurcated by Isla Cozumel; one branch passes between the island and the mainland, and the other branch passes to the east of this topographic wedge. He thus implied that the surface velocity profile may be caused by a turbulent vortex street downstream of Cozumel, which represents a disturbance in the current's vorticity field.

In this section, ERTS imagery and Skylab vertical photography are examined as evidence for this interpretation. In figure 4.5, a computer-enhanced MSS-5 image of the Yucatan-Cozumel area (fig. 4.13) and a Skylab photograph (fig. 4.14) in the central Gulf are located. The photograph and its interpretation are from a report by Maul *et al.* (1974) and is rediscussed here in order to offer a unified explanation of the eddies observed therein.

Figure 4.13 is a negative print and thus dark tones represent areas of high radiance. The water outside the current is seen to be of lower radiance than that in the current, and once again the radiance is dominated by a higher sea state or different glitter pattern in the current. Here the edge of the current can be seen leaving the coast northwest of Cozumel. In the wake of the island is a spacecraft observation of an oceanic von Karman vortex street; this is clearly the oceanographic analog to similar observations in the atmosphere, taken by Gemini and Apollo astronauts of the cloud cover over the Guadeloupe Islands in the equatorial Pacific Ocean. Figure 4.13 was imaged on 21 August 1972. The August 1972 pathline was observed at this time, and the current's edge and the vortex street are ocean features.

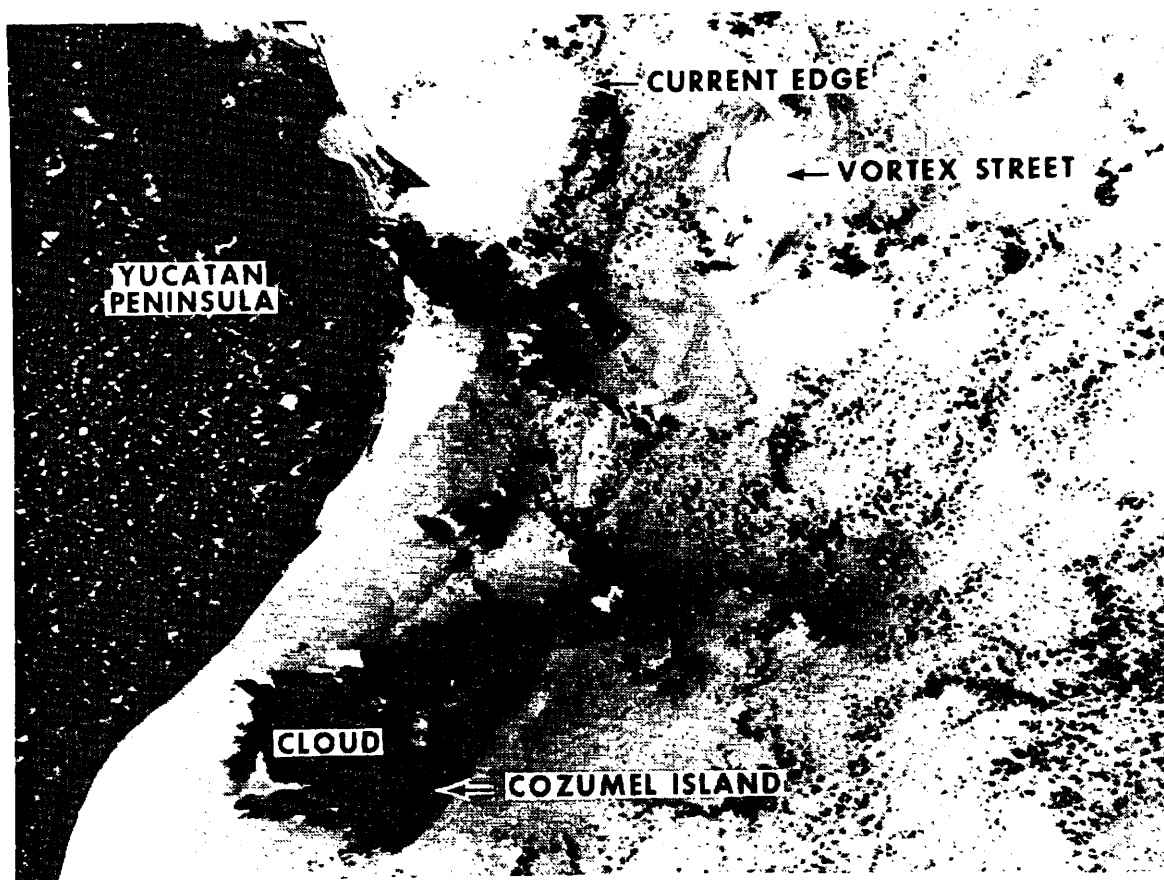


Figure 4.13 Negative print (ERTS ID 1029-15413) of computer-contrast-stretched ( $8 \leq DN \leq 16$ ;  $n=2$ ) MSS-5 image of Yucatan and Cozumel, Mexico, observed on 21 August 1972. The Yucatan Current's cyclonic edge can be seen emerging from between the island and the mainland. In the lee of Cozumel is a vortex pattern which causes a disturbance in the surface velocity profile well downstream. Horizontal distance across image is 135 km.

Surface current velocities were determined by the geostrophic method from the hydrographic transect of Yucatan Strait on 21-22 August 1972; station location is given in figure 2.4. Station spacing was very nearly 18 km, and the north component of the surface speeds relative to 700 dB, from Yucatan to Cuba, were: 103, 145, 80, 119, 73, 88, 62, and 35  $\text{cm sec}^{-1}$ . The low value of 80  $\text{cm sec}^{-1}$ , bracketed by higher values of 145 and 119  $\text{cm sec}^{-1}$ , is in the middle of the vortex zone shown in figure 4.13. This cross correlation of hydrographic and satellite data is taken as evidence that the observed double maxima is caused by topographic-induced vortex generation, and it explains one type of fine-scale structure as eddies imbedded in the main flow of the Yucatan Current.





Figure 4.14 Portion of vertical photograph from Skylab showing mesoscale eddies (arrows) associated with the Gulf Loop Current. Relationship of these eddies to the current is given in figure 4.5. Film was high-resolution aerial color type SO-356 which is responsive in the 400- to 700-nm interval. Photograph is available from EROS Data Center, reference number SL3-22-124. Positive print.

Figure 4.14 shows a portion of a photograph taken vertically from Skylab at an altitude of 434 km at 1735 G.m.t. on 4 August 1973. Solar azimuth at this time was  $175^{\circ}$  and the zenith angle was  $10^{\circ}$ . The sun's glitter pattern, or sunglint, permits the observation of the eddies which are located by arrows in the figure. In figure 4.5, the centers of the three eddies in figure 4.14 are located by dots. Four other eddies of the same size range, approximately 12 to 32 km in diameter, were photographed several seconds later northeast of the Yucatan Peninsula; their centers are located by dots near  $24^{\circ}\text{N}$ ,  $80^{\circ}\text{W}$ . The bright feature dominating the lower left of figure 4.14 is part of a large cloud region, the height of which may be estimated from its shadow to be 12,000 m. Lower clouds, however, are difficult to separate from ocean surface sunglint. The photographs were spaced so that 18% of the area appears in the adjacent photograph. This provides the parallax for a stereographic analysis

which insures that the eddies are indeed water surface features.

The specular point of the sun is outside the field of view, but surface waves spread the glitter pattern past the photograph's nadir point. During periods of light winds ( $2$  to  $4 \text{ m sec}^{-1}$  for these data), alternating slicks made visible by changes in reflectance can delimit the circulation pattern (Ewing, 1950). Reflectance differences are caused by slicks with suppressed capillary waves in which organic films are compacted because of lower surface tension under the film.

The most probable generation mechanisms of eddies are shear instability, topographic influence, or current meandering. Ocean eddies whose diameters are in the range  $10$  to  $100 \text{ km}$  are known to be quasigeostrophic and confined to the upper  $100$  to  $200 \text{ m}$  of the water column. Considering the size, shape, and position of the eddies, it seems reasonable to propose that they are associated with the horizontal velocity shear of the Gulf Loop Current (Lee, 1974) and appear to be instabilities at a surface of separation (Prandtl and Tietjens, 1957). According to this interpretation, the eddies are cyclonic; that is, the water on the right of figure 4.14 is moving toward the top of the photograph relative to that at the left.

Because the indicator isotherm has undergone a large eastward translation between July and August, exact relation of the eddies to the current is difficult to ascertain, however, the data suggest that these eddies may be in the main body of the current. The four eddies northeast of the Yucatan Peninsula are to the right of both indicator isotherms and within the current's characteristic width of  $100 \text{ km}$ . Hence, they appear to be embedded in the main flow near the current axis. This is in agreement with the observations taken 1 year earlier wherein it was observed that the fine-scale structure from the island is in midstream. These eddies, however, do not appear to be genetically the same as the vortex sheet eddies, which would make alternating vorticity downstream.

The possibility that the eddies in mid-Gulf are generated by Isla Cozumel cannot be dismissed based on these data. Photographic observations such as these are chance opportunities that may not capture the entire field of flow. If these eddies were shear instability features, then one could expect to find them in other areas of the stream as Stommel (1966) reported. If Cozumel was the only source of disturbance vorticity, then these eddies have been advected  $600 \text{ km}$  downstream and may be found many thousands farther. The latter seems unreasonable because of Cochrane's report that velocity profiles well upstream of Cozumel do not often exhibit these features. This may be dependent on the season of the year because the current does not always flow as close to the Mexican coast as it seems to in mid-summer.

## 5. DISCUSSION

The first section of this chapter addresses the capability of ERTS itself, and ocean color data in general, to observe pathlines of the Gulf Loop Current. Several factors limit the capability of ERTS to reproduce the ship tracklines; the reasons for the shortcomings are analyzed, and suggestions are made on the proper temporal, spatial, and spectral requirements for accomplishing the task. The pathlines of the current obtained by the ships are then discussed as though they were satellite observations in order to investigate the usefulness of such data to physical oceanography. Finally, suggestions for future research are made.

### 5.1 Evaluation of Ocean Color Data for Locating the Gulf Loop Current

During the course of observing the pathlines given in figure 3.2, over 250 ERTS scenes (>1000 images) were received, studied, and compared to the research vessel data. Approximately 60% of the ERTS scenes received for the Gulf of Mexico were not usable because of atmospheric conditions. Weather records for Key West during 1972 show that cloud cover was  $\leq 3/10$ , 39% of the time. The coincidence of these statistics suggests that when more than 3/10 of a scene is cloud-covered, interpretation of the data for ocean currents is impossible or inconclusive. The original ERTS data order placed an automatic rejection limit at 75% cloud cover. This appears to be too liberal, and significant processing and sorting time could have been saved if the upper limit were placed more conservatively at 40 to 50%.

Some images were disappointing because the sky was clear and yet there was no indication of the current, even though the surface observations indicated good Forel-color changes or sea-state changes. One explanation is to ascribe this to the gain settings on ERTS as being incorrect for the ocean. Incorrect gain settings also made distinguishing between thin clouds and subtle oceanic features impossible even with ground truth. This is perspicuous from the contrast-stretching (section 4.3) requirements; computer enhancement is necessary only because the dynamic range of ERTS was not set for the ocean. Hovis *et al.* (1974) have studied gain settings in the development of an ocean color sensor. If that instrument is incorporated on NIMBUS G as planned, the Gulf Loop Current will be observed more frequently.

The chlorophyll-a data given in table 3.1 show that there are at least 3 months of the year when no surface color change can be expected because there was a lack of chlorophyll-a change. Austin's (1971) maps of indicator organisms support the deep-sea chlorophyll observations made during these trackings, in that lower levels of change are found in deep water; that is, the values reported herein should be considered upper limits and perhaps even influenced by the proximity of coastal waters, especially in the Yucatan Strait. This implies that there are times when no significant color signature of the current exists. These data indicate that the color signature is lost during the winter. This is the time of year when temperature signatures are useful. Thus, a combination of color and infrared sensing is potentially capable of locating the Gulf Loop Current throughout the seasons.

Several important ancillary sensors are thus required which would overcome some of the shortcomings discussed above. An infrared channel (10.5-12.5  $\mu\text{m}$ ) is mandatory for identification of clouds in the absence of ocean thermal gradients, particularly when subtle color or sea-state changes occur. Stereographic cloud identification, which was so valuable in section 4.4, could also eliminate this problem. Cloud identification by stereographic means requires two scanners: one normal viewing and one with an angled view along the satellite trackline in order to duplicate the effect of overlapping photography.

The current was identified in 5% of the ERTS scenes which geographically coincided with the ship locations. ERTS reoccupies each suborbital track only once in 18 days and this has contributed to the sparsity of useful data. If ERTS obtained observations on a daily basis, then 5% data return would provide a useful observation every 20 days. This is entirely acceptable because, as the discussion in sections 1.2 and 3.2 indicate, the Gulf Loop Current was adequately located at 36-day intervals. This observation frequency, which satisfies needs in the eastern Gulf Of Mexico, is not a general statement of temporal requirements of the Gulf Stream System.

Temporal scales can best be discussed in light of a frequency spectrum. In figure 5.1, a kinetic energy spectrum of current meter records is shown. These data were collected by the Woods Hole Oceanographic Institution at site "D," which is located in deep water between the New England continental shelf and the Gulf Stream (Webster, 1967). Plotted on the upper abscissa is the period; the corresponding frequency in cycles per hour is plotted on the lower abscissa. The ordinate is in units of kinetic energy,  $\text{cm}^2 \text{sec}^{-2}$ . Causality of the several peaks is labeled on the diagram.

The Nyquist sampling theorem requires that a random variable must be sampled at a frequency at least twice the maximum frequency at which significant energy is found. Energy at higher frequencies will be folded at the Nyquist and alias the spectrum unless it is initially removed by the sampling technique. The local sea and swell shown in figure 5.1 will not be observable in remotely sensed imagery unless very high spatial resolution (1 m for 1-sec waves) is used. A large scanspot is equivalent to a low pass filter which cuts off the local sea. The spectrum can be considered to have a spectral gap at about 40 hr separating the energetic fluctuations at tidal and midlatitude inertial periods from the rest of the continuum, higher frequencies not being observable due to scanspot size.

If a sampling scheme were chosen with daily observations, the spectrum would be folded about 48 hr and the semidiurnal energies would be aliased into the spectrum at 96 hr. In the open sea, the energy in the tidal periods is quite small compared to that in Gulf Stream meanders (periods of about 45 days, Hansen, 1970). Therefore, a daily observational schedule for the open ocean is not a significant compromise. As the coast is approached, however, this no longer is valid. Here the tidal currents have a great deal more energy, and the use of the spectral gap at less than 6 hr is required. Except for tides, the Nyquist criterion is probably not adequate for resolving a geophysical random variable, and one would like to sample at 3-hr intervals in order to define other semidiurnal processes.

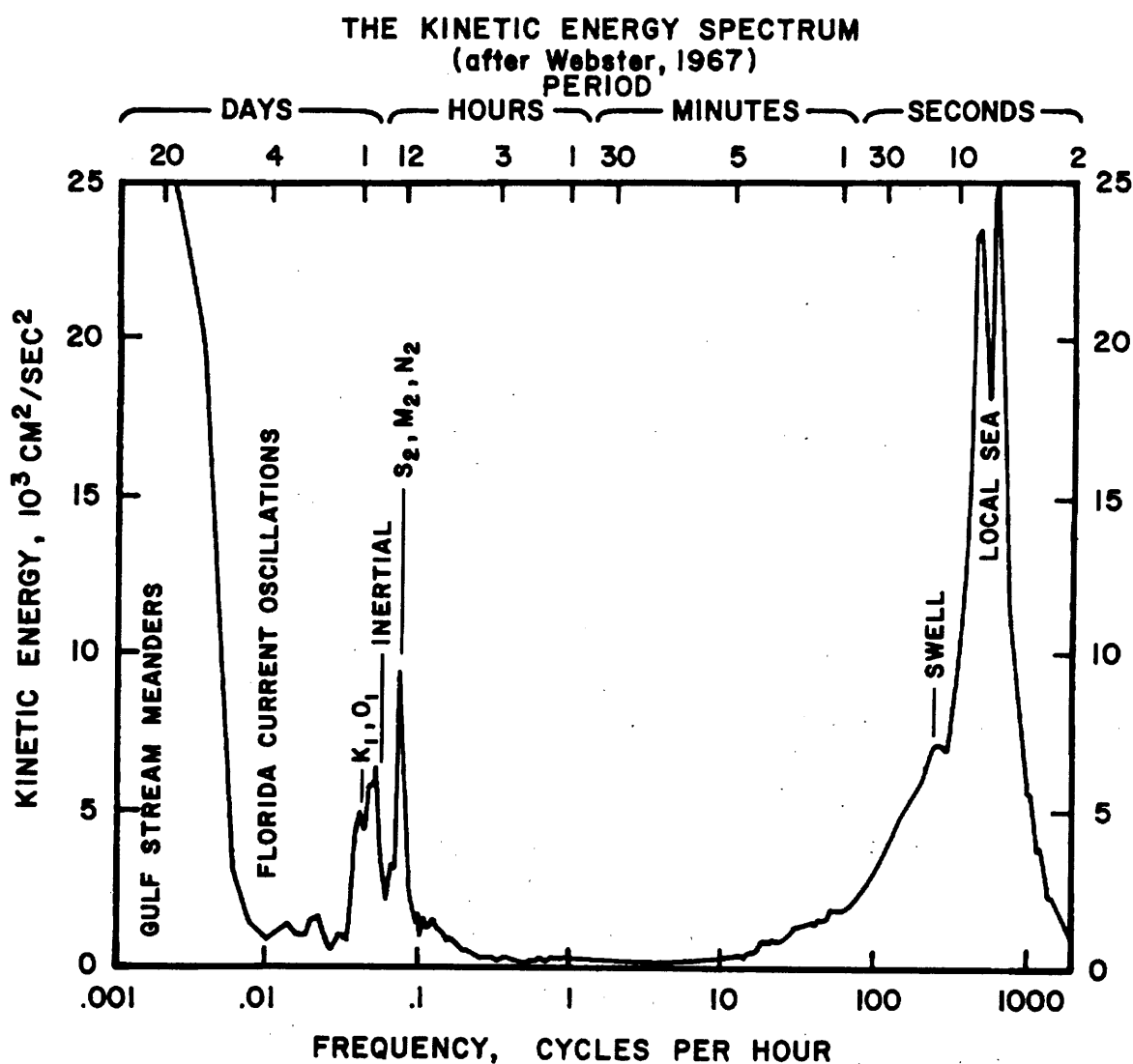


Figure 5.1 Kinetic energy spectrum of current meter records taken in water 2600-m deep at 39.3°N, 70°W by the Woods Hole Oceanographic Institution. The area under the spectral curve is kept proportional to total kinetic energy in this energy versus log frequency plot. Note that a displacement spectrum differs from this kinetic energy spectrum in that high frequency data would be much lower in amplitude.

As alluded to earlier, the spatial resolution can be used to limit what high frequency processes are observable. For example in deep water, swell with a period of 10 sec has a wavelength of 156 m. Since the radiance (N) in a scanspot is the integral of each element dN, the reflection pattern of sunlight, which varies with wave height within the scanspot, is lost. Most of the high frequency energy has periods less than 20 sec; to eliminate waves of that period, a spot size of 625 m is required.

A study of the effect of different spatial scales is given in figure 5.2. Figure 5.2a is an S190B Skylab photograph of the Straits of Florida showing a mass of Florida Bay water which has flowed through the pass just west of Marquesa Key into the strait. Figure 5.2b is an S190A Skylab photograph of the same feature taken on 8 January 1974. Spatial resolution of S190A is ~30 m and that of S190B is ~10 m. An ERTS image at the same time was not available; however, on 31 October 1972, an observation of a similar event occurred (fig 5.2c; see also fig. 4.9). ERTS has a scanspot size of approximately 80 m at the nadir. The ERTS resolution could be degraded by averaging the scanspot matrix into blocks of 2, 5, and 10. This corresponds to equivalent scanspot sizes of 160, 400, and 800 m for figures 5.2d, e, and f, respectively. All images in figure 5.2 are printed at the same scale.

Major features in the bottom topography are discernable up to 160-m resolution, but degrade rapidly after that. The shoreline of Marquesa Key loses its distinctiveness for mapping and identification purposes when the resolution is less than that in figure 5.2d. However, the major circulation feature in the sequence is still clear at 400-m resolution and somewhat less distinct at 800-m resolution. Thus, water mass features of this scale in the coastal zone are usefully detected with resolutions of about 400 m. Judging from other images (not shown) that show river plumes and waste dumping sites, the 400-m resolution is an appealing near upper limit. A spot size of this magnitude should be considered in light of the signal-to-noise requirements of an ocean color sensor which must have narrower optical spectral bandwidth than ERTS and indeed may specify those bandwidths (see also section 4.2).

The above considerations were all made without acknowledging one fundamental assumption: The data flow was assumed to be continuous. This is an unrealistic assumption for any sensor in the 0.4- to 16- $\mu$ m wavelength region of the electromagnetic spectrum because the normal state of the atmosphere is cloudy. To fill the gaps caused by the opaqueness of clouds, both temporal and spatial compositing is required. In midlatitudes, where atmospheric cyclonic waves have periods of about 5 days, variations in ocean color or temperature of not less than 10 days are then observable; this is adequate for Gulf Stream meanders and eddies. In the subtropics and tropics, the cloudiness is more nearly a diurnal event and higher frequencies can be detected such as Florida Current oscillations (periods of 4 to 6 days, Duing, 1973). Further, the subtropical clouds are typically 1 km in diameter and can be identified individually with a 400-m resolution scanspot; this is not the case in the higher latitudes where cloud cover is more extensive areally.

The spatial resolution requirements for ocean currents must then be broken down into what area is being studied and for what reason.

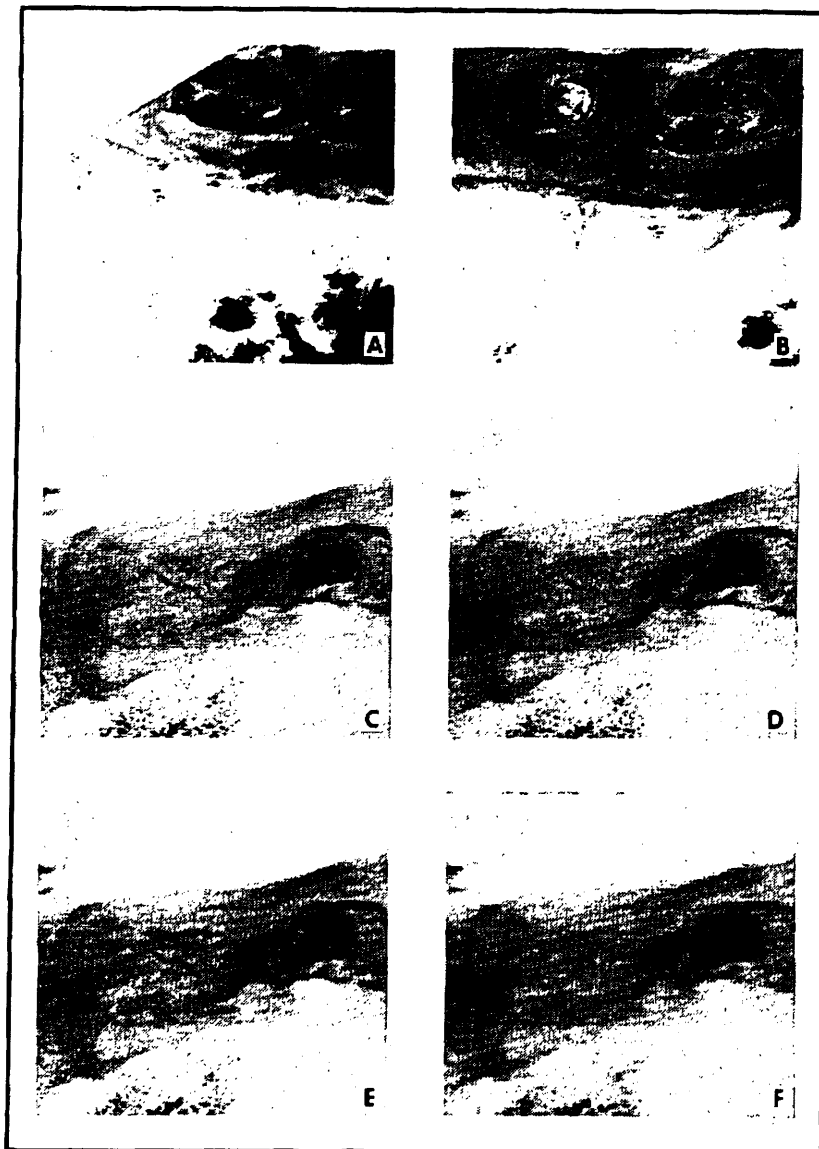


Figure 5.2 Negative prints of Marquesa Key in the Florida Keys showing water from Florida Bay to the north flowing into the straits. a) S190B black and white contrast-enhanced photograph. b) S190A color photograph, printed in black and white and contrast-enhanced. c) Original ERTS MSS-4 image, computer-contrast-stretched. d) ERTS image in (c) with data matrix blocked off in 2x2 units of original enhanced image. e) ERTS image in (c) with 5x5 blocking. f) ERTS image in (c) with 10x10 blocking. Photographs were taken by Skylab on 8 January 1974; ERTS images on 31 October 1972.

Certainly the 8-km resolution of the SMS-GOES infrared sensor or the NOAA scanning radiometer is adequate for location of the major features of the Gulf Stream. It is not adequate for studies of the fine-scale (10-15 km) eddies along the stream's cyclonic front or for Florida Current oscillations whose lateral extent may be of the order of 10 km. For such scale phenomenon, the NOAA-VHRR or Air Force DAPP data are spatially acceptable. On the other hand, ERTS data are more than adequate for the major coastal circulation features spatially, but temporally it is wholly inadequate because of its 18-day observation schedule.

In summary, there is a direct correlation between temporal and spatial requirements, and any sensing system must have the observational flexibility to accomplish the goal. Specifically, the following minimum requirements are noted: scanspot size for the open ocean and shelf areas not more than 10 km with periods not more than 24 hr; scanspot size for the coastal zone not more than 500 m with periods of about 3 hr; as an aside, scanspot size for internal wave observations not more than 25 m with periods of about 10 min and, for surface waves, 1-m resolution and 1-sec periods. ERTS data are spatially adequate for oceanography including certain internal wave observations, but they are not adequate temporally except for the utility of chance observations and to demonstrate the feasibility of sensing ocean color through the atmosphere.

## 5.2 Some Features of the Current Usefully Observed From Satellites

As discussed in the previous section, the ERTS data would be capable of providing adequate observations of the Gulf Loop Current if the orbital parameters of the vehicle were different. To assess the usefulness of a satellite time series, the pathlines of the 22°C isotherm at 100 m will be discussed as if they were remotely sensed data. Since the pathlines are about 15 km to the right of the cyclonic edge (facing downstream), they will be treated as if they were that edge for this analysis.

As shown in figure 4.13, both the direction of the current and the proximity to the Yucatan coast can be observed by remote sensing. Several investigators have related the behavior of the Yucatan Current and the Gulf Loop Current to the direction of flow through the Yucatan Strait: Simple dynamic models of the Gulf Loop Current such as those by Ichiye (1962) and Reid (1972) suggest that the penetration of the Yucatan Current into the Gulf depends on the flow direction. Molinari and Cochrane (1972) studied the influence of bottom topography and concluded that when the Yucatan Current is close to the coast, topography controls the flow through the conservation of potential vorticity.

The potential vorticity conserving model of Ichiye and Reid, in natural coordinates for a two-layer ocean with the lower layer at rest, is given by

$$\frac{KV - \frac{\partial V}{\partial n} + f}{D} = \text{constant}, \quad (5.1)$$



where  $K$  is curvature,  $V$  is velocity along a streamline,  $\hat{n}$  is the coordinate normal to the velocity vector, positive to the left facing downstream,  $f$  is the Coriolis parameter, and  $D$  is the depth of the upper layer. In the pathlines given in section 3.2,  $D$  is a constant 100 m. If it is assumed that the velocity core is a streamline whose neighboring streamlines are nearly equidistant,  $\partial V / \partial n$  is also constant. For that case, Ichiye and Reid's work gives

$$V = \frac{1}{2} p^2 \beta, \quad (5.2)$$

where  $p$  is the penetration of the streamline into the Gulf, and  $\beta$  is the meridional variation of  $f$ . To apply such a two-layer model to nature, the velocity in the upper layer is considered an average value. For the range of penetration distances observed in this work, 210 to 750 km,  $V$  would have to vary from 44 to 562 cm sec<sup>-1</sup> at Yucatan.

Reid was careful to point out that the model only holds in deep water, that is, north of Campeche Bank. A simple translation of the coordinates to account for this would make the lower velocity limits too small. If, however, the model is applied north of Campeche during those months when bottom topography controls the flow as far as 23°30'N (Molinari and Cochrane, 1972), and at the latitude of Cabo San Antonio at other times, then the velocity range is 44 to 303 cm sec<sup>-1</sup> (excluding August 1973). For the cyclonic turning from the Gulf into the Straits of Florida, velocities would have to be less than 50 cm sec<sup>-1</sup> to match the curvature. 44 to 50 cm sec<sup>-1</sup> is a reasonable value for the average surface value, but 303 cm sec<sup>-1</sup> is beyond the range of observations. These data suggest that a geostrophic deep-water potential vorticity-conserving model is not an adequate explanation.

During the February, March, April-May, June, and July 1973 cruises, the 22°C indicator closely follows the 100-m isobath from the Yucatan Strait almost to 24°N. Molinari and Cochrane used (5.1) to study the effect of topographic control; they assumed a homogeneous fluid with water depth  $D$ . From figure 3.2, it can be seen that the bottom topography of Campeche Bank does not control the current during August, September, October-November, and December 1972, or September 1973. The Yucatan Current is farther to the west during periods when surface velocities are highest, and these are also the months where the indicator hugs Campeche Bank. Thus, when the current is strongest, in spring and summer (Molinari and Cochrane did their analysis on data observed in May 1962, 1965, and 1966), and is farther to the west, the velocity near the bottom may be sufficient for equation (5.1) to describe the dynamics coarsely.

It is useful to compare pathlines of the 22°C isotherm with historical data averaged by months. Robinson's (1973) atlas clearly shows that the minimum penetration of the Loop occurs in March and April, whereas the maxima are in August and September. Whitaker's (1971) averages show that the minimum is in November and the maxima are in May and October. Leipper found minima in August 1965 and November 1965 and a maximum in August-October 1966. From figure 3.2, it is seen that the minimum here occurred in October-November and the maximum in July-August. This summary points out the high degree of

temporal variability in the Gulf Loop Current and emphasizes that the data obtained in this study are not to be considered as a final description of the cycle.

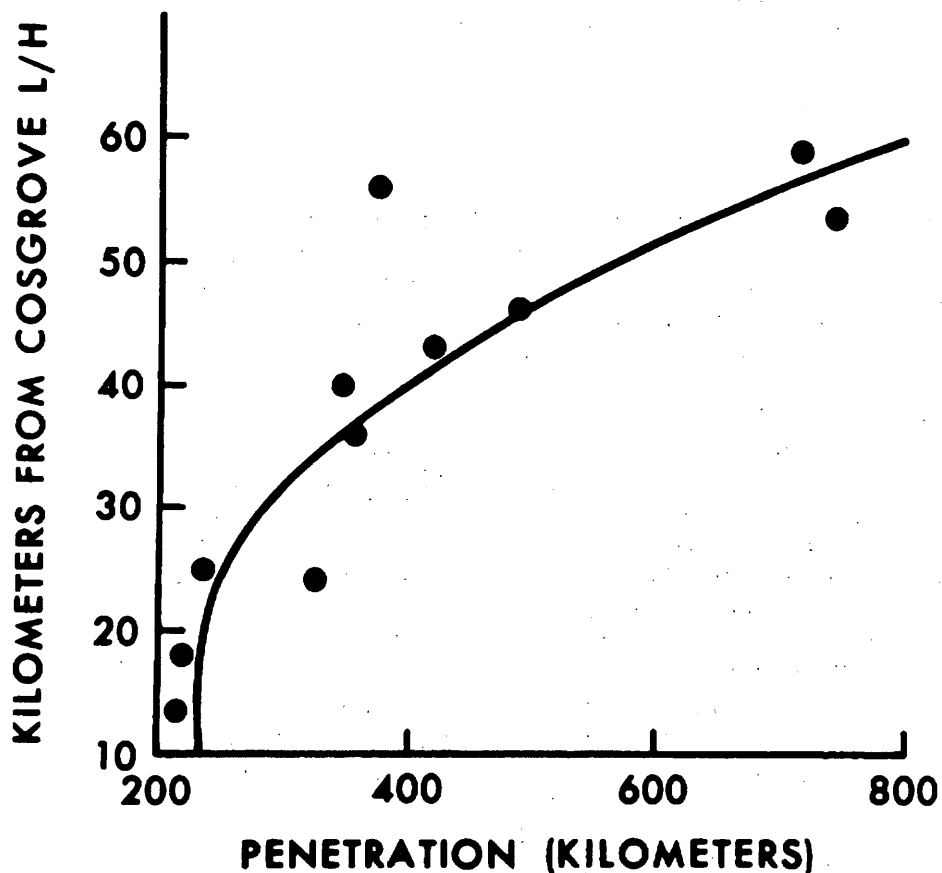


Figure 5.3 Distance that the 22°C isotherm at 100-m depth was found from Cosgrove Lighthouse (northern terminus of the Straits of Florida transects) versus distance from Cabo San Antonio to the northern penetration of the current into the Gulf of Mexico. The heavy line is the least-squares fit to the data. The point at 55 and 400 km represents a case where the indicator was near 100 m for three STD stations, but was chosen to be the first crossing from north to south for consistency.

One interesting kinematic result is summarized in figure 5.3. The northern terminus of the Florida-Cuba section was near Cosgrove Lighthouse. The horizontal distance between the navigation aid and the 22°C isotherm at 100-m depth is plotted against the northern extent of the indicator into the Gulf as measured from Cabo San Antonio. The solid line through the data is the second-degree least-squares polynomial. The farther north that the current penetrates into the Gulf, the farther south it was found in the Straits of Florida. This relationship eventually must break down. Topography is a limiting factor in causing this, since the current must be turned by the Cuban coast (see especially the July and August 1973 cruise tracks). Paskausky and Reid's (1972) numerical model also shows that the current flows close to Cuba when the penetration of the Loop Current is greatest. This suggests that topography limits the description of this current as an inertial flow and contributes to the apparent curvature of the data in figure 5.3. There are no analytic models of inertial currents that incorporate bottom topography against which these observations can be tested.

The salt and heat balance in the Gulf of Mexico is a problem to which satellite data may be applied. The volume of water necessary to make the Loop grow can be estimated from the length of the pathlines which can be measured from satellite images. Assuming a mean depth of 500 m, pathline measurements show that 64,000 km<sup>3</sup> of resident Gulf water must be displaced by Yucatan water in the 6 months that the Loop grows. The excess transport of Yucatan water into the Gulf in this period averages 4.1 x 10<sup>6</sup> m<sup>3</sup> sec<sup>-1</sup>. Continuity requires that this inflow must be balanced by a discharge as will be discussed below.

As an independent check on the above value, sea-level records were studied. Cochrane (1965) showed that there is a good correlation between the monthly sea-level difference between Habana and Progreso and the average ship drift in the western Yucatan Strait. Approximately the transport (T) difference between Yucatan and Florida should be reflected in the sea-level data. Marmer's (1954) mean monthly sea-level data, uncorrected for barometric differences, are used. The stations are Habana (1947-1950), Key West (1930-1948), and Progreso (1947-1950). Each of these stations show a characteristic rise in sea level to a maximum in September or October and a minimum in February or March in response to the annual steric cycle range of ± 15 cm. For a geostrophically balanced barotropic flow, the transport difference between the Habana-Progreso (T<sub>H</sub>-K) is given by

$$T_{H-P} - T_{H-K} = \frac{gz}{f} (h_K - h_P) + C, \quad (5.3)$$

where g is gravity, z is depth, h<sub>K</sub> is the monthly sea level at Key West, h<sub>P</sub> is at Progreso, and C = (h̄<sub>K</sub> - h̄<sub>P</sub>)gz/f, where the overbars denote mean annual sea level. Progreso and Key West are on the same side of the current, and it is assumed that mean sea level along the coast is approximately the same; therefore C=0. During the period that the Loop is growing, the difference h<sub>K</sub>-h<sub>P</sub> = 4.88 cm. The transport difference calculated from (5.3), assuming again the current to be 500 m deep, is 3.8 x 10<sup>6</sup> m<sup>3</sup>sec<sup>-1</sup> during this period.

By two independent methods, it is shown that there must be an excess inflow of Yucatan water. Jacobs (1951) estimated that evaporation exceeds precipitation in the Gulf by 35 cm per year. This would account for only  $0.02 \times 10^6 \times \text{m}^3 \text{ sec}^{-1}$  excess of inflow. Sea level in the Gulf does not rise 34.5 m in 6 months as implied by excess inflow, and Wennekens estimated very little Gulf of Mexico water exits the Straits of Florida. This implies that Hansen's (1972) and Schlitz's (1973) direct measurements of a net south drift at the bottom of the Yucatan Strait may have detected the major source of discharge. Schlitz's estimate of the southward transport through the Yucatan Strait, based on April 1970 data, is  $4 \times 10^6 \text{ m}^3 \text{ sec}^{-1}$  which is in excellent agreement with this discussion.

The area enclosed by the  $22^\circ\text{C}$  isotherm at 100-m depth along the line from Cosgrove Lighthouse to Habana, along the Cuban coast to Cabo San Antonio and across to Isla Contoy, was estimated using a polar planimeter from figure 3.2. The area enclosed by the Loop Current defines a volume of Yucatan water, and its annual cycle should be related to volume transports. As a first estimate, the transports are assumed proportional to current velocities through the Yucatan Strait, as estimated from Cochrane's ship drift studies. The comparative results are plotted in figure 5.4. The sharp decrease in area between August and September 1973 is due to the separation of the anticyclonic eddy discussed in section 3.2. A clear correlation exists between area and current velocities, with little phase lag between transport and the area covered by the current system. The numerical models of Wert and Reid (1972) and Paskausky and Reid (1972) attempted to relate the penetration of the Gulf Loop Current to changes in the vorticity distribution or velocity field of the Yucatan Current, but they kept the volume transport constant; Ichiye (1972) used changes in the Yucatan velocity in a rotating tank model, but did not relate the velocities to the penetration. There are no established relationships between velocity or vorticity fields in the Yucatan Current with transports, nor are there any models (except indirectly Reid (1972) or Ichiye (1962)) which use changes in transport to drive the circulation in the Gulf of Mexico.

If the difference in area between August and September 1973 in figure 5.4 is used as an estimate of the eddy size,  $89,000 \text{ km}^2$  of Yucatan water has been exchanged into the Gulf. A characteristic length scale for the eddy is its diameter ( $L$ ). The Austausch coefficient is proportional to  $L^2/t$  and, for a  $t$  of 1 year, this calculates to be a coefficient of  $3.6 \times 10^7 \text{ cm}^2 \text{ sec}^{-1}$ . Paskausky and Reid used  $1 \times 10^6 \text{ cm}^2 \text{ sec}^{-1}$  in their barotropic model; Wert and Reid selected  $5 \times 10^6 \text{ cm}^2 \text{ sec}^{-1}$  for the lateral friction coefficient in their baroclinic model. Ichiye (1972) chose parameters in a physical model that make the corresponding horizontal Austausch coefficient  $1.8 \times 10^6 \text{ cm}^2 \text{ sec}^{-1}$ . These values are approximately an order of magnitude less than estimated from the eddy separation. It would be a useful theoretical problem to relate surface areas such as this to estimates of exchange coefficients and processes.

In summary, treating the time series as if it were satellite data has illustrated several useful applications to physical oceanography. Potential vorticity-conserving models, used for estimating penetration (5.2) and topo-

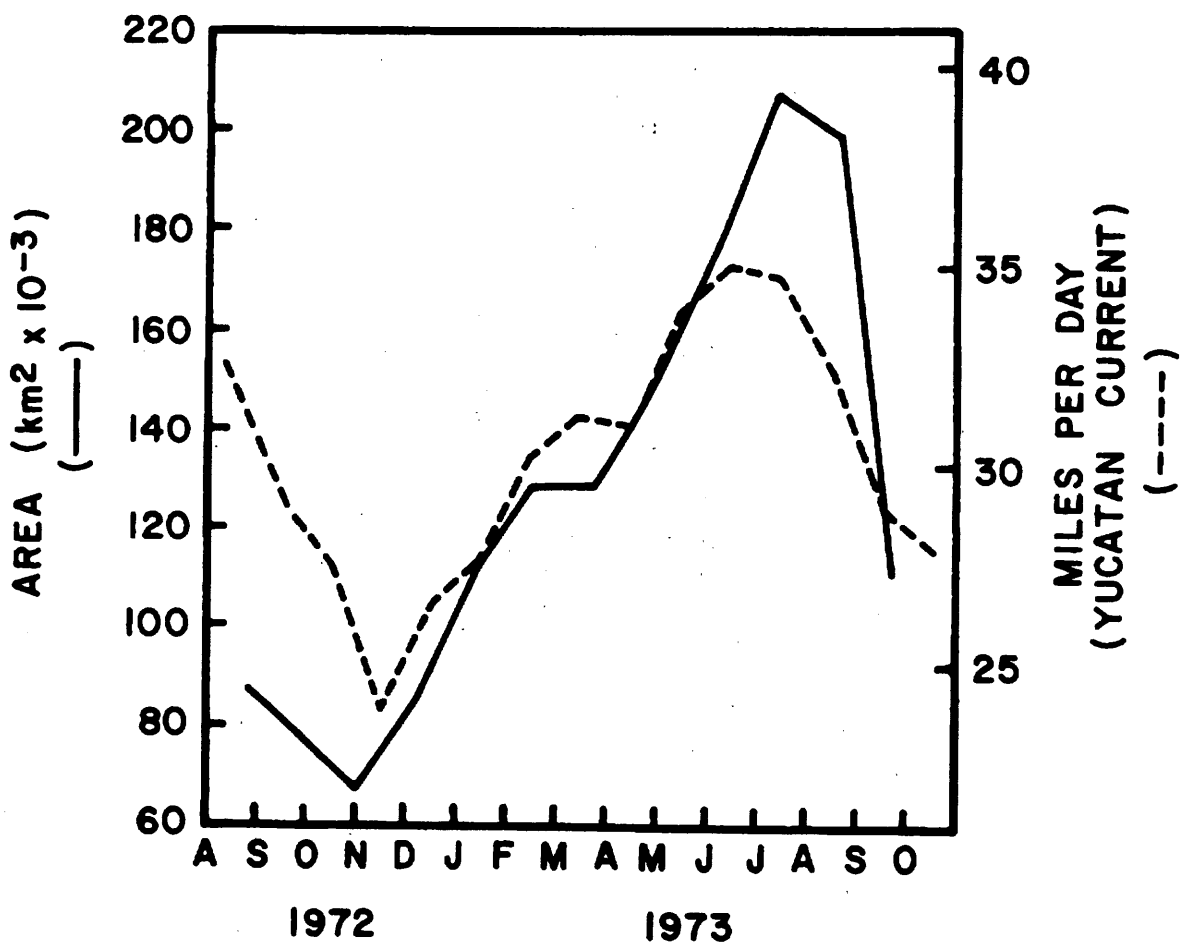


Figure 5.4 Annual cycle of surface area, enclosed by the 22°C isotherm in the Gulf and the Key West-Habana-Cabo San Antonio-Isla Contoy boundary, is the solid line. Dashed line is the annual cycle of surface velocities as estimated by Cochrane (1965) for the Yucatan Current from ship drift reports.

graphic control, are not adequate in explaining the data set obtained as part of this research (fig. 3.2). Comparisons with atlases and Leipper's (1970) sequence show that there is a great deal of variability in the current pattern; that variability could be investigated with continued satellite studies. The kinematic observation given in figure 5.3 suggests that a productive interplay between remote sensing and conventional oceanography is the usefulness of satellite data in "tuning" numerical models. Finally, estimates of the excess inflow of Yucatan water during Loop growth can be made by areal measurements of satellite-sensed coverage.

### 5.3 Suggestions for Future Research

The ship pathlines observed in this study were planned to give adequate ground truth for the satellite observations. Their contribution to the physical oceanography of the Gulf of Mexico has not been fully exploited. Figure 5.4 suggests that the cycle of the Gulf Loop Current is related to the changing transport of the Yucatan Current. The numerical models referred to in section 5.2 used changing distributions of the velocity field or the vorticity field in the Yucatan Strait as a varying boundary condition. The hydrographic data across this channel should be studied to determine if there is a relationship between transport, surface velocity, and vorticity and thus to specify the dominant driving mechanisms for the annual cycle.

As noted in section 5.2, the Gulf of Mexico has a net excess of evaporation over precipitation ( $E > P$ ). It is for this reason that the basin is called the American Mediterranean. C.G.H. Rooth (personal communication) has raised the question of the salt balance problem for the Gulf since not only does  $E > P$  contribute to higher salinities, the separation of an anticyclonic eddy contains the core of the Subtropical Underwater must also add salt. Since there is no evidence that the Gulf of Mexico salinities are increasing, a Mediterranean-type circulation may be superimposed. The other possibility is that salinity in the Straits of Florida is slightly higher than in the Yucatan Strait. Estimates of the net salt flux may be possible from the hydrographic transect data.

During the January-June 1973 phase of this study, infrared and visible data from the NOAA-2 satellite scanning radiometer were archived. The ERTS visible data have been shown to have a Gaussian frequency distribution in section 4.3. An initial evaluation of the NOAA-2 visible data show that the distribution is positively skewed when clouds partially fill the scene. Skewness then is applicable as a test for determining the radiance range of visible data that are cloud-free. This allows a scanspot-by-scanspot test as to whether an infrared data point is cloud-free. The acceptable infrared data can then be corrected for atmospheric transmittance, using the technique proposed by Maul and Sidran (1973), and then mapped with consideration to objective analysis (Gandin, 1963).

During the course of this research, approximately 325 reflectance spectra were observed in the eastern Gulf of Mexico. This data set represents spectra from these waters, for which the chlorophyll-a concentration and volume-scattering function are known. Baig and Yentsch (1969) have shown that a suite of spectra can be represented by linear combination of their average and three

eigenvectors. Using a multiple forward-selection procedure, it is possible to extend Baig and Yentsch's results and specify several wavelengths (say three or four) needed to reconstruct a spectrum (S. Baig, personal communication). Thus, the specification of the most important wavelengths for an ocean color sensor, needed to reconstruct the spectrum, can be accomplished in an objective manner.

The study of climate is fast becoming an important and popular research topic. An important variable in climate modelling is the albedo of the Earth. The data in figure 4.8 and the discussion in section 4.1 on the effect of sea state on upwelling radiation show that the albedo of the sea changes with changing wind speed. Thus, a feedback mechanism in climate studies (that has not been addressed) is the air-sea interaction effect on climate. If the mean wind speed changes as the climate changes, the albedo of the Earth will also change, and this will cause a change in the radiation balance of the Earth in the visible region of the spectrum. The importance of this has not been assessed in the recent literature and could very profitably be studied by satellite techniques.

Finally, as noted in section 4.1, the most efficient means of analyzing spectra will probably be to compute best fits of theoretical spectra to observations. These spectra must then be related to the biological and optical aspects of the water under study. Phytoplankton samples have been obtained and sorted by Ednoff (1974) for many of the spectra. Thus, a catalog of spectra for the area can be initiated for which the theoretical parameters and observational variables are known. It is not until sufficient spectra with known relationships to the marine environment are available that spacecraft observations can be utilized to their full potential.

## 6. CONCLUSION

This research has been primarily undertaken to evaluate the use of an ocean-color-sensing satellite (ERTS) for observing currents in the subtropics. The Gulf of Mexico was chosen as a test site because there the cyclonic boundary of the Gulf Loop Current cannot be detected by infrared techniques during the summer, and this current is the major circulation feature of the eastern Gulf. The ground-truth pathlines (fig. 6.1) provide measurements of the seasonality of several optical properties across the current as well as a proper history of the flow itself for comparison with satellite data and for basic oceanography.

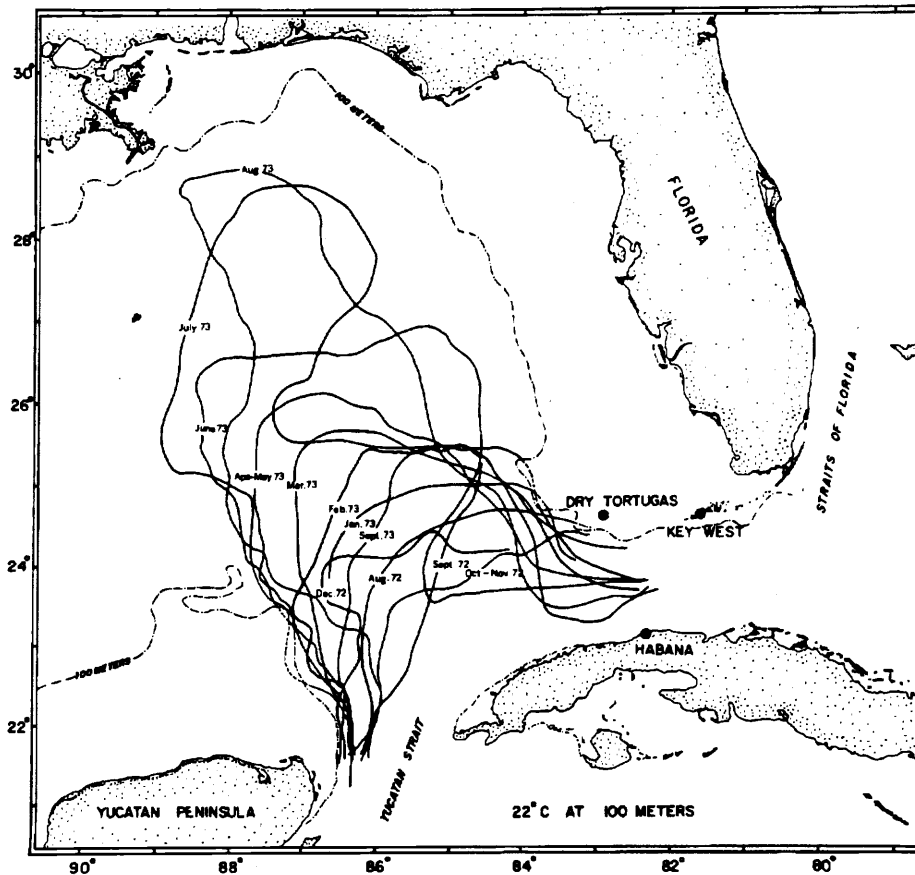


Figure 6.1 Compilation of pathlines of the 22°C isotherm at 100-m depth from August 1972 through September 1973 (see also fig. 3.2). Where the indicator isotherm intersected the bottom topography, a dashed line is used to estimate its position from the other thermal data. Where the cruise started in 1 month and ended in another, both months are indicated. 100-m isobath is indicated by a dash-dot line and it represents very closely the shelf break and escarpment zone.



From the results of this study, it has been shown that:

- (1.) Using color-sensing satellites to detect the Gulf Loop Current (and other baroclinic flows) is feasible, but ERTS is not an ideal vehicle because of sensor gain settings, multispectral scanner channel wavelengths, and the 18-day revisit cycle (section 5.2).
- (2.) Currents can be detected by color sensing satellites in three ways: by a color change across the cyclonic boundary (changes in the optical properties of the water), by a change in sea state at that boundary (changes in surface albedo), and by changes in the glitter patterns which delimit circulation patterns (sections 4.3 and 4.4).
- (3.) Variations in chlorophyll-a concentrations and volume-scattering function throughout the year are such that there is not a significant permanent color signature of the cyclonic boundary at all times. This data set, however, suggests that a combination of visible and infrared remote sensing can potentially locate the Gulf Loop Current throughout the year (sections 3.1 and 4.3).
- (4.) Shipboard observations of upwelling spectral irradiance show that clustering techniques can differentiate between Gulf Stream water, coastal waters, and plankton blooms, but the ratio or difference of radiance methods gives ambiguous results. Important wavelengths identified for future ocean color sensors are: 470, 530, 655, 675, and 1000 nm (sections 4.1 and 4.2).
- (5.) Evidence for turbulence embedded in the core of the Gulf Loop Current is obtained from comparing velocity profiles across the Yucatan Strait with satellite imagery. Two sources of turbulence are tentatively identified: shear instability and topographic influence (section 4.4).
- (6.) The average separation between the satellite-sensed front of the Gulf Loop Current and the 22°C isotherm at 100 m or the 15°C isotherm at 200 m is approximately 15 km. Curvature effects have been shown to alter significantly the separation between the surface front and the indicator isotherms (sections 3.1 and 3.3).
- (7.) An unambiguous time series of the Gulf Loop Current based on ship observations shows that Leipper's (1970) proposition is correct in that there is an annual cycle of growth and decay, but that year-by-year variability in the patterns is significant. An anticyclonic eddy separation is shown to have occurred at least once each year in the last 5 years (section 3.3).

- (8.) The annual cycle of growth, eddy separation, and decay is in phase with the annual cycle of transport of the Gulf Stream System. During the period that the Gulf Loop Current is growing, resident Gulf of Mexico waters must be displaced; this requires that  $4 \times 10^6 \text{ m}^3 \text{ sec}^{-1}$  more Yucatan water enters the basin in the upper layers than leaves through the Straits of Florida (section 5.2).
- (9.) Radiance range of ERTS bandpass sensors for the ocean is estimated from the computer-enhanced images to be (cf. table 2.1):

MSS	Range ( $\text{m W cm}^{-2}\text{sr}^{-1}$ )
4	0.15 - 0.75
5	0.05 - 0.35
6	0.05 - 0.25
7	0.05 - 0.40

Contrast-stretching is required to obtain useful oceanographic information from ERTS (section 4.3).

## 7. ACKNOWLEDGMENTS

The data in this time series were obtained by the R/V BELLOWS and the R/V VIRGINIA KEY and are a testimony to the dedication and seamanship of the crews of these 65-ft vessels, and particularly to their masters, F. Davis, G. Hood, and B. Neill. I received valuable assistance in data collection from M. Ednoff, G. Dingle, J. Holmes, C. Bernier, I. Velez, D. Mayer, J. Festa, B. Kolitz, E. Murphy, C. Thacker, and J. Hazelworth. Much of the data processing was ably assisted by R. Qualset, M. McCaslin, R. DeVivo, and I. Burden. Drafting and advice on figures and layout were done by R. Carrobus, D. Senn, and S. O'Brien; photography was by A. Ramsay.

I have had many fruitful discussions on these data with colleagues and friends from the Texas A & M University, the Florida State University, the Florida State University System Institute of Oceanography, the National Aeronautics and Space Administration, and the University of Miami as well as the Atlantic Oceanographic and Meteorological Laboratories. Particularly, I would like to acknowledge J. Cochrane, M. Ednoff, M. Rinkel, D. Norris, W. Johnson, A. Leetmaa, R. Molinari, F. Chew, and my mentors, H. Gordon, C. Rooth, D. Hansen, E. Corcoran, K. Hanson, and W. Duing.

This research was in part supported by contract GSFC-C0315 through the National Aeronautics and Space Administration's Earth Resources Program and the National Environment Satellite Service's Environmental Sciences Group. The author of this manuscript wrote the original proposal to NASA and was awarded the contract by NASA as principal investigator. Results reported herein are due to direct supervision by the principal investigator.

## 8. REFERENCES

- Anderson, E. R. (1954), Energy budget studies. In: Water Loss Investigations Lake Hefner Studies. U. S. Geological Survey Professional Papers 269, pp. 71-117.
- Arvesen, J. C. (1972), Airborne differential radiometer measurements of chlorophyll in water. Fourth Annual Earth Resources Review, Vol. IV. NASA MSC-05937, pp. 104-1 to 104-2.
- Austin, H. R. (1971), The characteristics and relationships between the calculated geostrophic current component and selected indicator organisms in the Gulf of Mexico Loop Current System. Ph. D. Dissertation, Florida State University, Department of Oceanography, Tallahassee, 369 pp.
- Baig, S. R., and C. S. Yentsch (1969), A photographic means of obtaining monochromatic spectra of marine algae. Appl. Opt., 8 (12), pp. 2566-2568.
- Beardsley, G. F., H. Pak, K. Carder, and B. Lundgren (1970), Light scattering and suspended particles in the eastern equatorial Pacific Ocean. J. Geophys. Res., 75 (15), pp. 2837-2845.
- Capurro, L. R. A., and J. L. Reid, Editors (1972), Contributions on the Physical Oceanography of the Gulf of Mexico. Gulf Publ., Houston, 288 pp.
- Chandrasekhar, S. (1960), Radiative Transfer. Dover, New York, 393 pp.
- Charnell, R. L., and G. A. Maul (1973), Oceanic observation of New York Bight by ERTS-1. Nature, 242 (5398), pp. 451-452.
- Chew, F. (1974), The turning process in meandering currents: A case study. J. Phys. Oceano., 4 (1), pp. 27-57.
- Clark, G. L., G. C. Ewing, and C. J. Lorenzen (1970), Spectra of back-scattered light from the sea obtained from aircraft as a measurement of chlorophyll concentration. Science, 167, pp. 1119-1121.
- Cochrane, J. D. (1965), The Yucatan Current. In: Annual Report, Project 286. Texas A & M University, Ref. 65-17 T, College Station, pp. 20-27.
- Corcoran, E. A., and J. E. Alexander (1963), Nutrient, chlorophyll, and primary production studies in the Florida Current. Bull. Mar. Sci. Gulf and Carib., 13 (4), pp. 527-541.
- Corwin, T. L., and H. R. Richardson (1974), Preliminary Report to the Commandant of the Coast Guard on the Gulf of Mexico Cyanide Barrel Spill. Daniel H. Wagner Assoc., Paoli, Pa., 36 pp.

- Cox, C., and W. Munk (1954), Measurements of the roughness of the sea surface from photographs of the sun's glitter. J. Opt. Soc. Am., 44 (11), pp. 838-850.
- Curran, R. J. (1972), Ocean color determination through a scattering atmosphere. Appl. Opt., 11 (8), pp. 1857-1866.
- Duing, W. (1973), Some evidence for long-period barotropic waves in the Florida Current. J. Phys. Oceano., 3 (3), pp. 343-346
- Duntley, S. Q. (1972), Detection of ocean chlorophyll from earth orbit. Fourth Annual Earth Resources Review, Vol. IV. NASA MSC-05937, pp. 102-1 to 102-25.
- Ednoff, M. E. (1974), Surface phytoplankton communities and their relationship to the Loop Current in the Gulf of Mexico. Master's Thesis, Florida State University, Department of Oceanography, Tallahassee, 187 pp.
- Ewing, G. (1950), Slicks, surface films, and internal waves. J. Mar. Res., IX, (3), pp. 161-187.
- Ford, W. L., J. R. Longard, and R. G. Banks (1952), On the nature, occurrence and origin of cold low salinity water along the edge of the Gulf Stream Front. Deep-Sea Res., 3, pp. 46-65.
- Fuglister, F. C. (1951), Annual variations in current speeds in the Gulf Stream. J. Mar. Res., 10, pp. 119-127.
- Fuglister, F. C., and A. D. Voorhis (1965), A new method of tracking the Gulf Stream. Limnol. Oceanogr., 10, pp. R115-R124.
- Galtsoff, P. S., Editor (1954), Gulf of Mexico--It's Origin, Waters, and Marine Life. Fishery Bulletin 89, Fish and Wildlife Service, 604 pp.
- Gandin, L. S. (1963), Objective Analysis of Meteorological Fields. National Technical Information Service, TT 65-50007, Springfield, Va., 242 pp.
- Gordon, H. R. (1973), A simple calculation of the diffuse reflectance of the ocean. Appl. Opt., 12, pp. 2804-2805.
- Gordon, H. R., O. B. Brown, and M. M. Jacobs (1974), Computed relationships between the inherent and apparent optical properties of a flat homogeneous ocean. Submitted to Appl. Opt.
- Gordon, J. R. (1974), Spectral variations in the volume scattering function at large angles in natural waters. J. Opt. Soc., 64, (6), pp. 773-775.
- Gordon, H. R., and W. R. McCluney (1974), Estimation of the depth of sunlight penetration in the sea for remote sensing. Submitted to Appl. Opt.

- Hansen, D. V., and G. A. Maul (1970), A note on the use of sea surface temperature for observing ocean currents. Remote Sensing of Environ., 2, pp. 161-164.
- Hansen, D. V. (1970), Gulf Stream meanders between Cape Hatteras and the Grand Banks. Deep-Sea Res., 17, pp. 495-511.
- Hansen, D. V. (1972), Deep currents in the Yucatan Strait. EOS, Transactions, A.G.U., 53 (4), p. 392.
- Hanson, K. J. (1972), Remote sensing of the ocean. In: Remote Sensing of the Troposphere (V. G. Derr, Ed.). U.S. Govt. Print. Off., Washington, pp. 22-1 to 22-56.
- Hovis, W. A., M. L. Forman, and L. R. Blaine (1974), Detection of ocean color changes from high altitudes. NASA GSFC X-652-73-371, Greenbelt, Md., 25 pp.
- Ichiye, T. (1962), Circulation and water mass distribution in the Gulf of Mexico. Geofis. Inter., 2 (3), pp. 47-76.
- Ichiye, T. (1972), Experimental circulation modelling within the Gulf and the Caribbean. In: Contributions on the Physical Oceanography of the Gulf of Mexico. Gulf Publ., Houston, pp. 213-226.
- Jacobs, W. C. (1951), The energy exchange between sea and atmosphere and some of its consequences. Bull., Scripps Inst. Oceanogr., 6 (2), pp. 27-122.
- Jerlov, N. G. (1968), Optical Oceanography. Elsevier, New York, 194 pp.
- Kalle, K. (1938), Zum problem der Meeres wasserfarbe. Ann Hydrol. Marine Mitt., 66, pp. 1-13.
- Lee, T. N. (1974), Florida Current spin-off eddies. Submitted to Deep-Sea Res.
- Leipper, D. F. (1970), A sequence of current patterns in the Gulf of Mexico. J. Geophys. Res., 75 (3), pp. 637-657.
- Leipper, D. F., and D. Volgenau (1970), Hurricane heat potential of the Gulf of Mexico. EOS, Transactions, A.G.U., 51 (4), p. 312.
- Lorenzen, C. J. (1971), Continuity in the distribution of surface chlorophyll. J. du Conseil Inter. Pour l'Exploration de la Mer, 34 (1), pp. 18-23.
- Mairs, R. L. (1970), Oceanographic interpretation of Apollo photographs. Photogrammetric Engr., pp. 1045-1058.
- Maul, G. A. (1973), Remote sensing of ocean currents using ERTS imagery. Symposium on Significant Results Obtained from the Earth Resources Technology Satellite--1. NASA SP-327, Vol. 1(B), pp. 1365-1375.

- Maul, G.A. (1974), A one year time series of the Gulf Loop Current. EOS, Transactions, A.G.U., 56(4), p. 283.
- Maul, G.A., and D.V. Hansen (1972), An observation of the Gulf Stream front structure by ship, aircraft, and satellite. Remote Sensing of Environ., 2, pp. 109-116.
- Maul, G.A., and M. Sidran (1973), Atmospheric effects on ocean surface temperature sensing from the NOAA satellite scanning radiometer. J. Geophys. Res., 78 (12), pp. 1909-1916.
- Maul, G.A., and H.R. Gordon (1974), Relationships between ERTS radiances and gradients across oceanic fronts. Third Earth Resources Technology Satellite-1 Symposium. NASA SP-351, Vol. 1(B), pp. 1279-1308.
- Maul, G.A., and R.L. Charnell, and R.H. Qualset (1974), Computer enhancement of ERTS-1 images for ocean radiances. Remote Sensing of Environ. (In press).
- Maul, G.A., D.R. Norris, and W.R. Johnson (1974), Satellite photography of eddies in the Gulf Loop Current. Geophys. Res. Ltrs. (In press).
- Molinari, R.L., and J.D. Cochran (1972), The effect of topography on the Yucatan Current. In: Contributions on the Physical Oceanography of the Gulf of Mexico. Gulf Publ., Houston, pp. 149-155.
- Murphy, E., K. Steidinger, B. Roberts, J. Williams, and J. Jolley (1974), An explanation of the Florida East Coast Gymnodinium breve red tide, November 1972. Limnol. Oceanogr. (In press).
- NASA (1971), Earth Resources Technology Satellite Data Users Handbook. NASA Document No. 71SD4249.
- Neumann, G., and W. J. Pierson, Jr. (1966), Principles of Physical Oceanography. Prentice-Hall, Englewood Cliffs, N.J., 545 pp.
- Niiler, P.P., and W.S. Richardson, Jr. (1973), Seasonal variability of the Florida Current. J. Mar. Res., 31 (3), pp. 144-167.
- Nowlin, W.D., Jr., and H.J. McLellan (1967), A characterization of the Gulf of Mexico waters. J. Mar. Res., 25 (1), pp. 29-59.
- Parker, C.E. (1972), Some direct observations of currents in the Gulf Stream. Deep-Sea Res., 19 (12), pp. 879-893.
- Paskausky, D.F., and R.O. Reid (1972), A barotropic prognostic numerical circulation model. In: Contributions on the Physical Oceanography of the Gulf of Mexico. Gulf Publ., Houston, pp. 163-176.
- Prandtl, L., and O.G. Tietjens (1957), Fundamentals of Hydro- and Aeromechanics. Dover, New York, pp. 221-223.

- Reid, R. O. (1972), A simple dynamical model of the Loop Current. In: Contributions on the Physical Oceanography of the Gulf of Mexico. Gulf Publ., Houston, pp. 157-159.
- Robinson, M. K. (1973), Atlas of Monthly Mean Sea Surface and Subsurface Temperature and Depth of the Top of the Thermocline Gulf of Mexico and Caribbean Sea. Scripps Inst. Oceanogr. Reference 73-8, 105 pp.
- Ross, D. B., and V. Cardone (1974), Observations of oceanic whitecaps and their relation to remote measurements of surface wind speed. J. Geophys. Res., 79, (3), pp. 444-452.
- Sauberer, F., and F. Ruttner (1941), Die Strahlungsverhältnisse der Binnengewässer. Akademie Verlag, Berlin, 240 pp. .
- Schlitz, R. J. (1973), Net total transport and net transport by water mass categories for Yucatan Channel based on data for April 1970. Ph.D. Dissertation, Texas A & M University, Department of Oceanography, College Station, 107 pp.
- Smith, R. E., Editor (1974), Proceedings of Marine Environmental Implications of Offshore Drilling Eastern Gulf of Mexico; 1974. Florida State University System Institute of Oceanography, St. Petersburg, 455 pp.
- Stommel, H. (1966), The Gulf Stream. Univ. of California, Berkeley, 248 pp.
- Strong, A. E. (1973), ERTS-1 anomalous dark patches. National Technical Information Service, NASA CR-1333115; E73-10747, Springfield, Va.
- Strickland, J. D. H., and T. R. Parsons (1968), A Practical Handbook of Seawater Analysis. Fisheries Research Board of Canada, Ottawa, 311 pp.
- Szekielski, K. H. (1973), Distribution pattern of temperature and biomass in the upwelling area along the NW coast of Africa. In: Proceedings of the Fall Convention ASP-ASCM October 2-5, 1973, pp. 664-719.
- Tyler, J. E., and R. C. Smith (1970), Measurements of Spectral Irradiance Underwater. Gordon and Breach, New York, 103 pp.
- Uda, M. (1938), Researches on "Siome" or current rip in the seas and ocean. Geophys. Mag., 11 (4), pp. 307-372.
- von Arx, W. S., D. Bumpus, and W. S. Richardson (1955), On the fine structure of the Gulf Stream front. Deep-Sea Res., 3, pp. 46-65.
- Webster, F. (1967), A scheme for sampling deep-sea currents from moored buoys. Transactions, 2nd International Buoy Technology Symposium. Mar. Tech. Soc., Washington, pp. 419-431.



- Wert, R. T., and R. O. Reid (1972). A baroclinic prognostic numerical circulation model. In: Contributions on the Physical Oceanography of The Gulf of Mexico. Gulf Publ., Houston, pp. 177-209.
- Wennekens, M. P. (1959), Water mass properties of the Straits of Florida and related waters. Bull. Mar. Sci. Gulf and Carib., 9 (1), pp. 1-52.
- Whitaker, R. E. (1971), Seasonal variations of steric and recorded sea level of the Gulf of Mexico. Master's Thesis, Texas A & M University, Department of Oceanography, College Station, 109 pp.
- Yentsch, C. S. (1960), The influence of phytoplankton pigment on the color of the sea. Deep-Sea Res., 7, pp. 1-9.
- Yentsch, C. S. (1962), Measurement of visible light absorption by particulate matter in the ocean. Limnol. Oceanogr., 7 (2), pp. 207-217.

## 9. APPENDIXES

### APPENDIX A

In this section, several ERTS-1 images of the Gulf Stream System are summarized. Each of the selected images used in this report are located in figure A.1. Frame numbers 1, 2, 3, 4, and 5 were discussed in the body of the text and will not be repeated here. The selected images are from the area of concern as stated in the title; this does not mean that these were the only good images of the current. About 10% of the images received that passed the 60% cloud cutoff criterion actually had ocean current information. The rest were either in the wrong area or the current was not visible; the latter cause accounted for about 25% of the null information.

Figure A.2 was used by Maul and Gordon (1974) to study the capability of ERTS to determine the particle concentration. In that study, they showed that if

$$\frac{\text{MSS-4}}{\text{MSS-5}} = \text{constant}, \quad (\text{A.1})$$

then

$$\nabla \text{MSS-4 or-5} \propto \nabla b_p / b_W, \quad (\text{A.2})$$

which is in turn proportional to the gradient of the particle concentration. Along the scanline shown in figure A.2, the gradient in MSS-4 and MSS-5 has been computed using several filters; the correlation coefficient (r) has been computed for each filter pair as well. The results of using different low pass filters and filter lengths are summarized in figure A.3.

The general trend is that r increases with longer filter kernels and with lower pass filters. This means that the gradient on the Earth's surface with 8-km (100 sample low pass) spatial scale has greater coherence between bands. It is not certain as to why the small-scale correlation coefficient is so low. This area has significant amounts of coastal sediments which are rich in organics, and thus the Gelbstoff concentrations probably vary over a wide range.

In the images to follow, the interpretations given are based on the discussion in the text. Only one band is given in the appendix, but all were studied for interpretation. Clouds were identified in MSS-6 and MSS-7 and were optically masked out of the image before study, so that the data discussed are water phenomenon and not an atmospheric contribution. Water color shift from green to blue was made by studying whether the variation in MSS-4 disappeared in MSS-5; if so, the color of low radiance scanspots in MSS-4 must be bluer than the higher radiance data. Similarly sediments are not seen in MSS-7 or frequently even in MSS-6; clouds are always seen in all four channels. The images are presented for the general use of other marine scientists without discussion except for the figure captions.

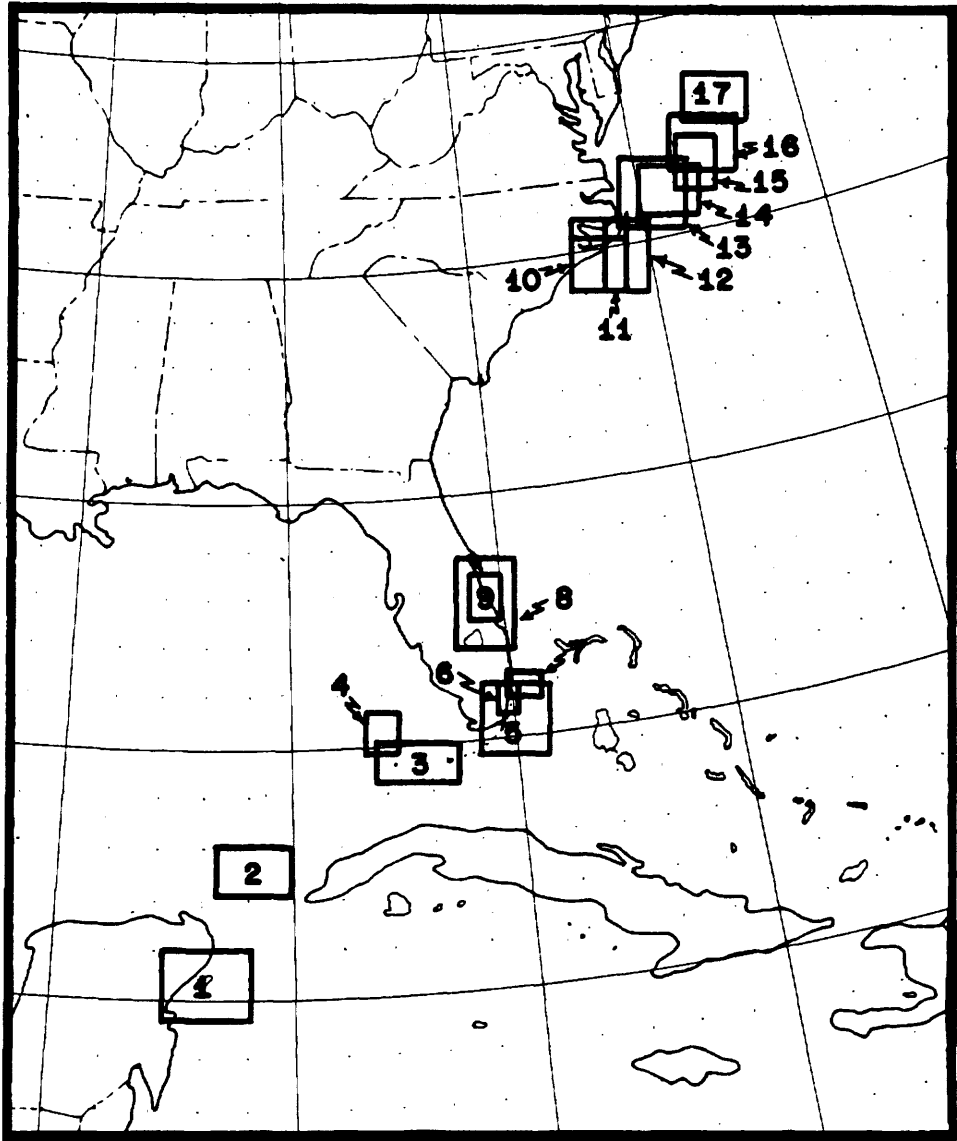


Figure A.1 Location map of selected images in appendix A. Images 1, 2, 3, 4, and 5 were discussed in the text and are not repeated here. Images 6-17 are labeled figures A.6-A.17: There is no figure A.5, and figures A.1 and A.4 are used for introductory discussion.

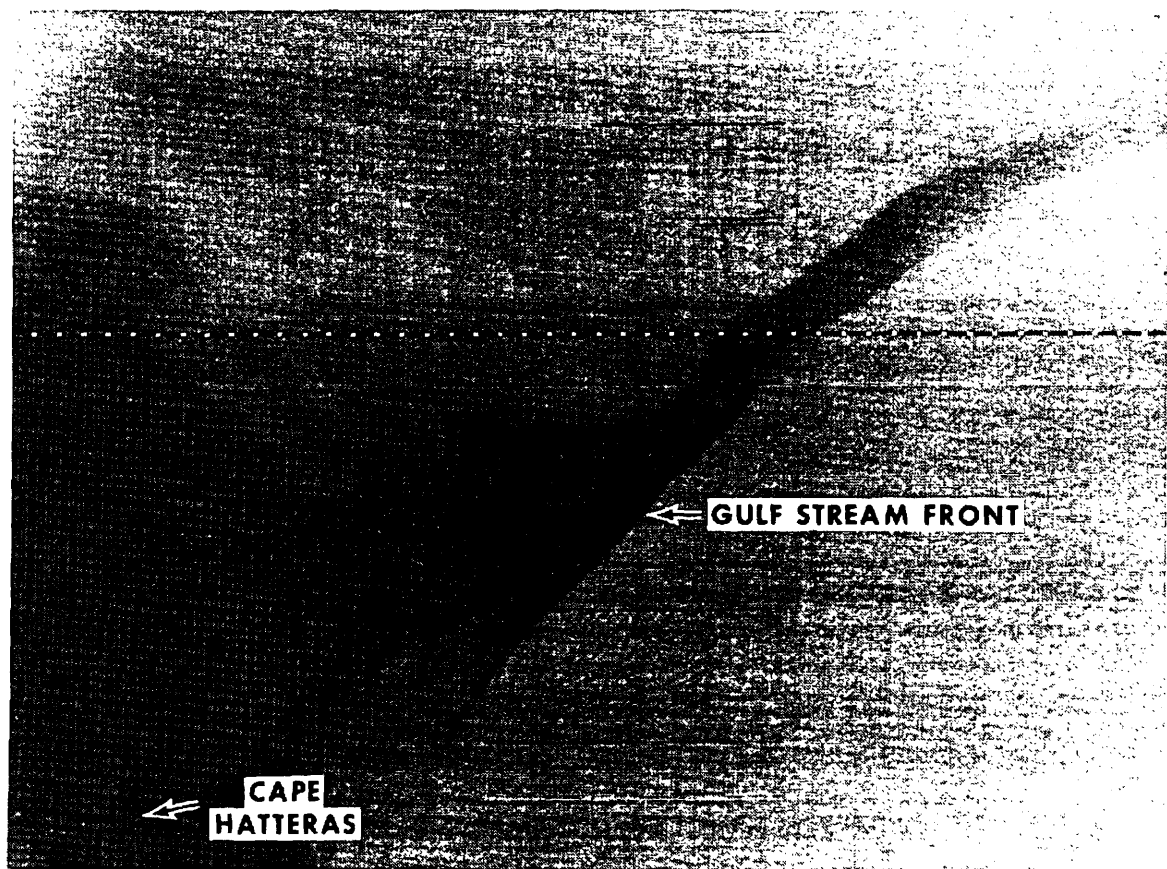


Figure A.2 Contrast-stretched ( $4 \leq DN \leq 12$ ;  $n=2$ ) negative MSS-5 image of the ocean area offshore of Cape Hatteras (ERTS ID 1132-15042), observed on 2 December 1972. The Gulf Stream can be seen as the bright area to the south of the entrained sediment from the coastal estuaries. The least-squares fit of (A.1) was done along the scanline north of the Cape and extending from nearshore, through the suspended sediment, and into the current. Extensions of this plume were observed for 150 km farther east on other ERTS images. Horizontal distance across the image is 135 km.

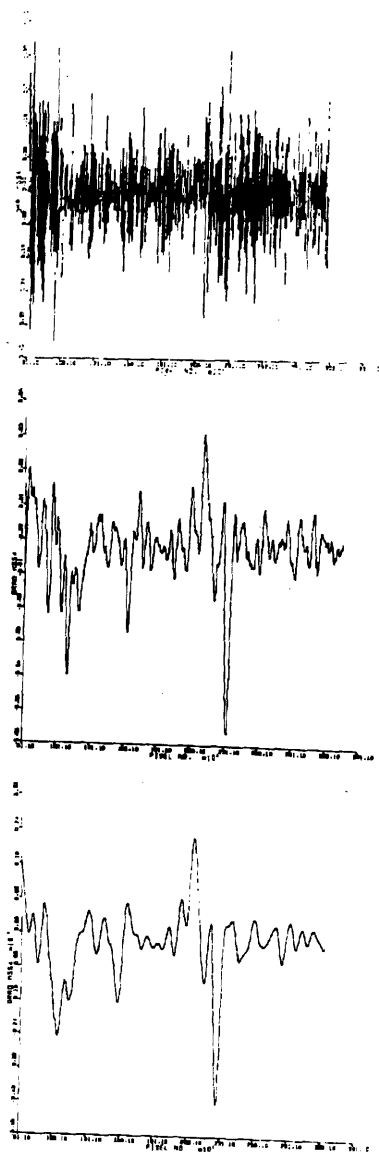


Figure A.3 Gradient of radiance received at the satellite in MSS-4 along the scanline shown in figure A.2. Scanspot numbers arbitrarily start at 1 which is just off the image in the previous figure and over the coast. Correlation coefficient ( $r$ ) for the MSS-4, MSS-5 linear correlation is: upper - 10 sample low pass (199 element kernel),  $r=0.085$ ; middle - 100 sample low pass (59 element kernel),  $r=0.398$ ; lower - 100 sample low pass (159 element kernel),  $r=0.698$ . Compare with figure A.4 for 100 sample low pass using 199 elements in the filter kernel, where  $r=0.740$ .

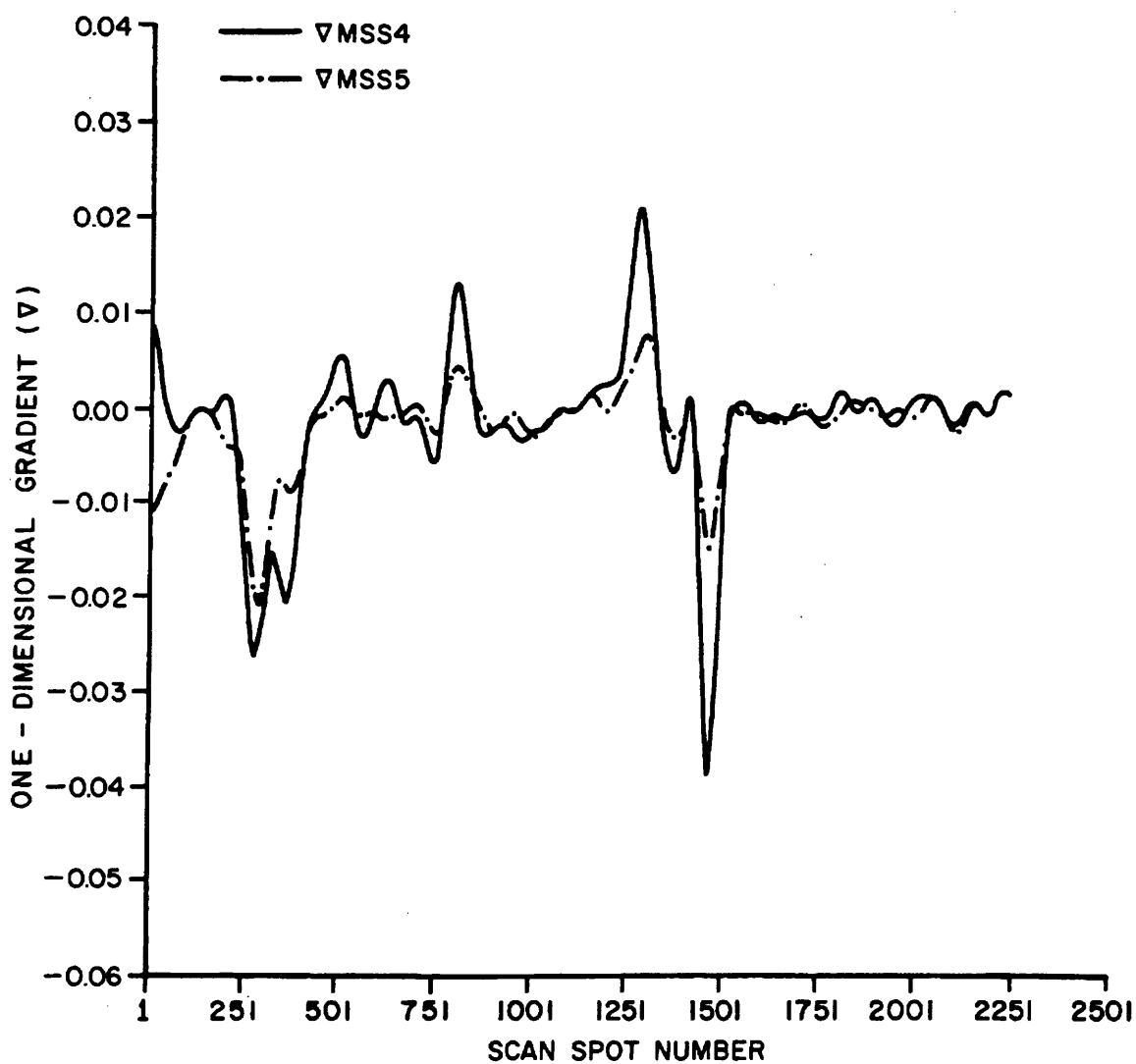


Figure A.4 Gradient of radiance in MSS-4 and MSS-5 along the scanline shown in figure A.2, using a 100 sample low pass filter (199 element kernel). The linear correlation coefficient ( $r$ ) is 0.740 for this filter. These data suggest that  $\nabla\text{MSS-4}$  or  $\nabla\text{MSS-5}$  is a good estimate of the gradient of the particle concentration.

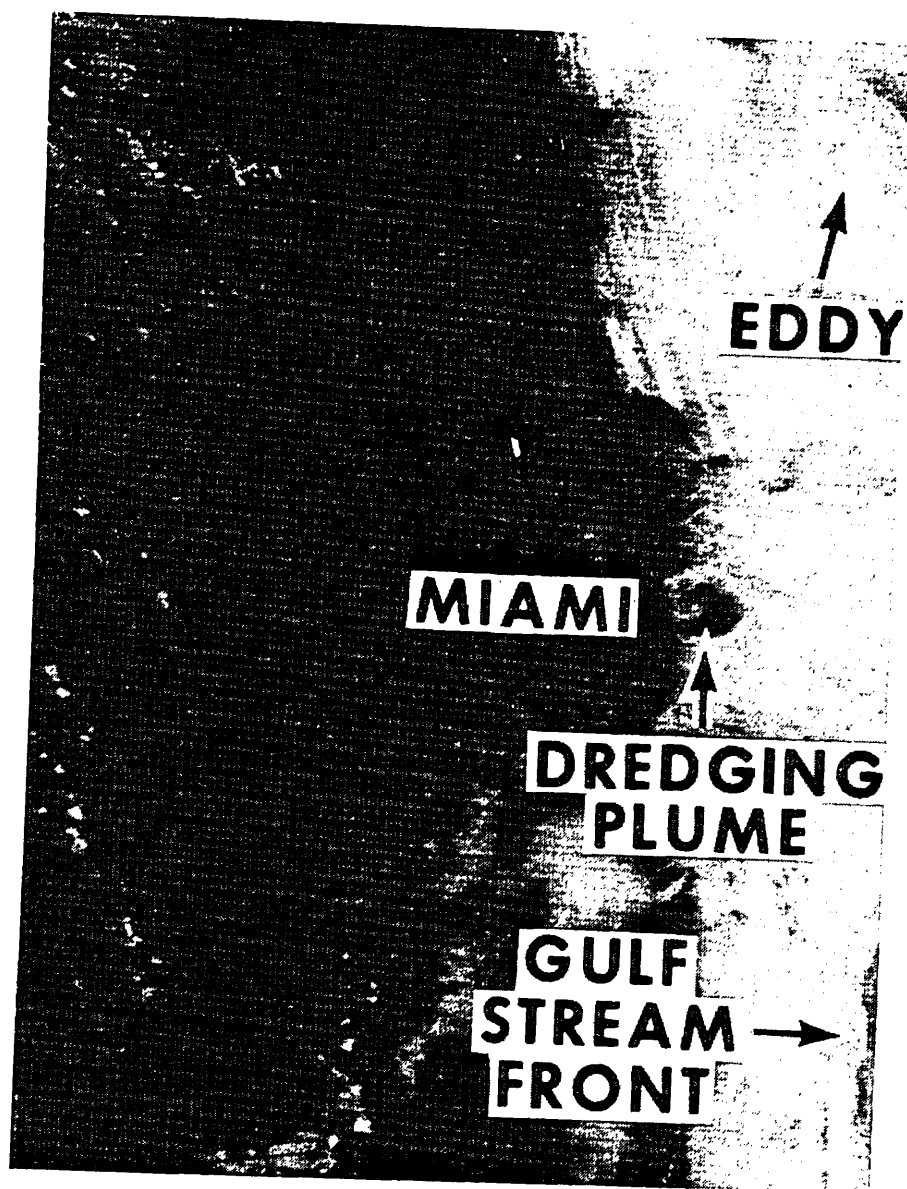


Figure A.6 Contrast-stretched ( $12 \leq DN \leq 21$ ;  $n=1$ ) negative MSS-5 image of Miami, Florida (ERTS ID 1350-15231), observed on 8 July 1973. Government Cut and the Miami harbor basin were being dredged when this image on the ebb tide was taken. The dredge spoil can be seen as a jet flowing out into the shelf where a cyclonic circulation is caused by the Longshore drift. A cyclonic eddy, either spinoff or shear-induced (Lee, 1974) by the Gulf Stream, is seen in the upper right due to changes in surface reflectance. The Gulf Stream front at the lower right is seen due to higher radiance in the current. Complications of nearshore currents can be deduced because of the offshore eddy, and the northern inlets have a southward inshore drift that has reversed or slackened near the dredging plume. Horizontal distance across the image is 45 km.

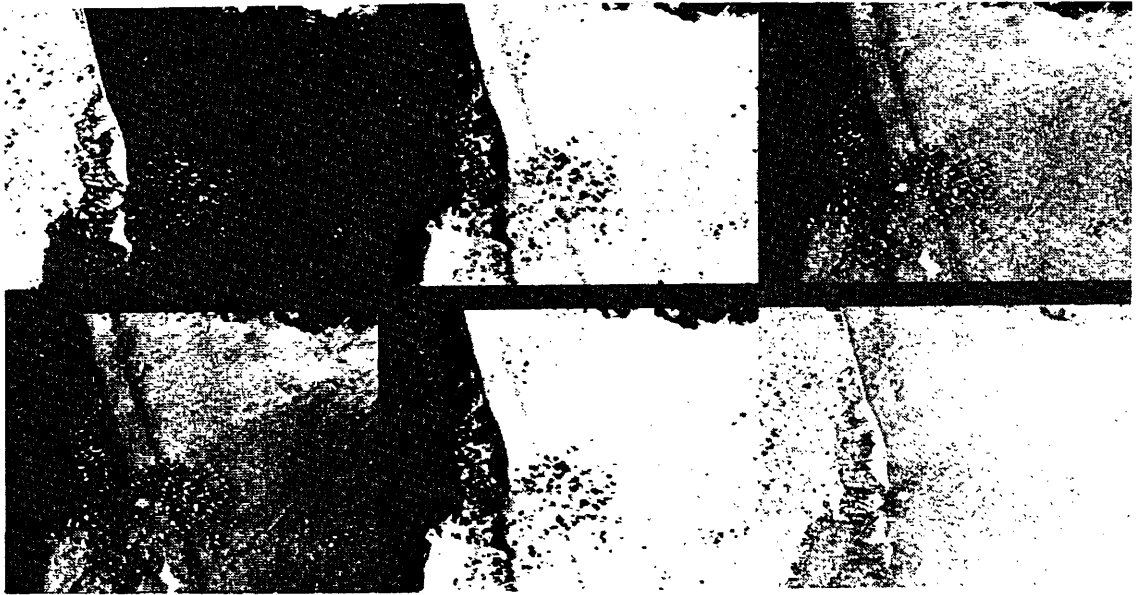


Figure A. 7 Contrast-stretched sequence of MSS-6 data off Miami Beach, Florida (ERTS ID 1026-15230), observed on 18 August 1972. Sequence shows the effect of varying the DN range and  $n$  in the contrast equation. a) Upper left: Raw data, positive print. b) Upper middle:  $7 \leq \text{DN} \leq 15$ ;  $n=1$ . c) Upper right:  $7 \leq \text{DN} \leq 15$ ;  $n=3$ . d) Lower left:  $7 \leq \text{DN} \leq 11$ ;  $n=1$ . e) Lower middle:  $9 \leq \text{DN} \leq 13$ ;  $n=1$ . f) Lower right: MSS-6 minus MSS-7, then  $5 \leq \text{DN} \leq 13$ ;  $n=3$ . Note that using powers of  $n$  brings out water details (cf. b & d). Water details in e are less distinct than in b which uses the statistically determined limits. Sea state only is observable in MSS-7, so MSS-6-MSS-7 should minimize the surface contribution as is shown in f. Horizontal distance across each image is 45 km.



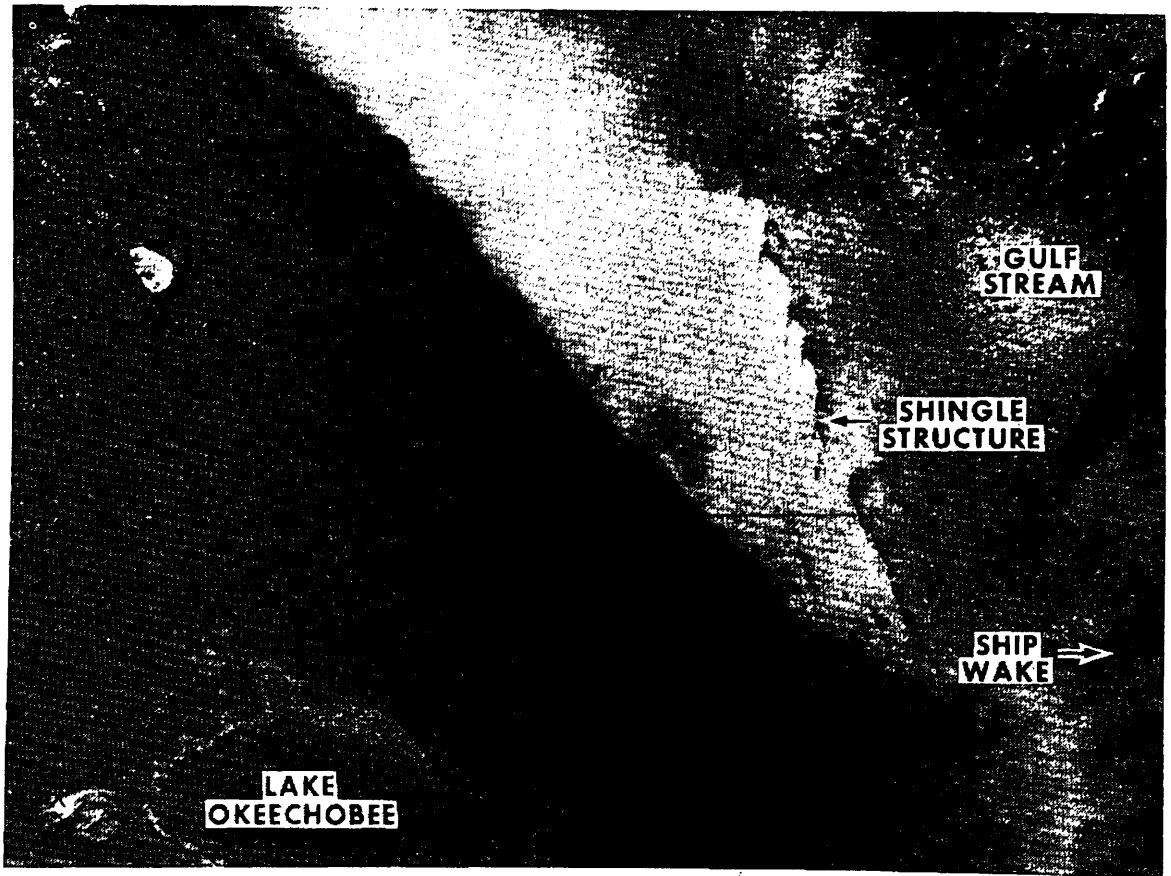


Figure A.8 Contrast-stretched ( $9 \leq DN \leq 17$ ;  $n=1$ ) negative MSS-5 image of the region offshore of Cape Canaveral, Florida (ERTS ID 1260-15233), observed on 9 April 1973. Fine-scale "shingle structure" (von Arx, Bumpus, and Richardson, 1955) can be seen along the cyclonic edge of the Gulf Stream. The shingel structure in this image is at least an order of magnitude less than the von Arx *et al.* description off the Carolinas. Wind streaks and a ship wake can be observed in the Gulf Stream which is leaving the coast at the lower right. Loss of water detail in Lake Okeechobee is caused by the contrast stretch limits and shows that the very high radiance from this water body is due to a turbidity about equal to the coastal inlet plume in the upper left. Horizontal distance across the image is 135 km.

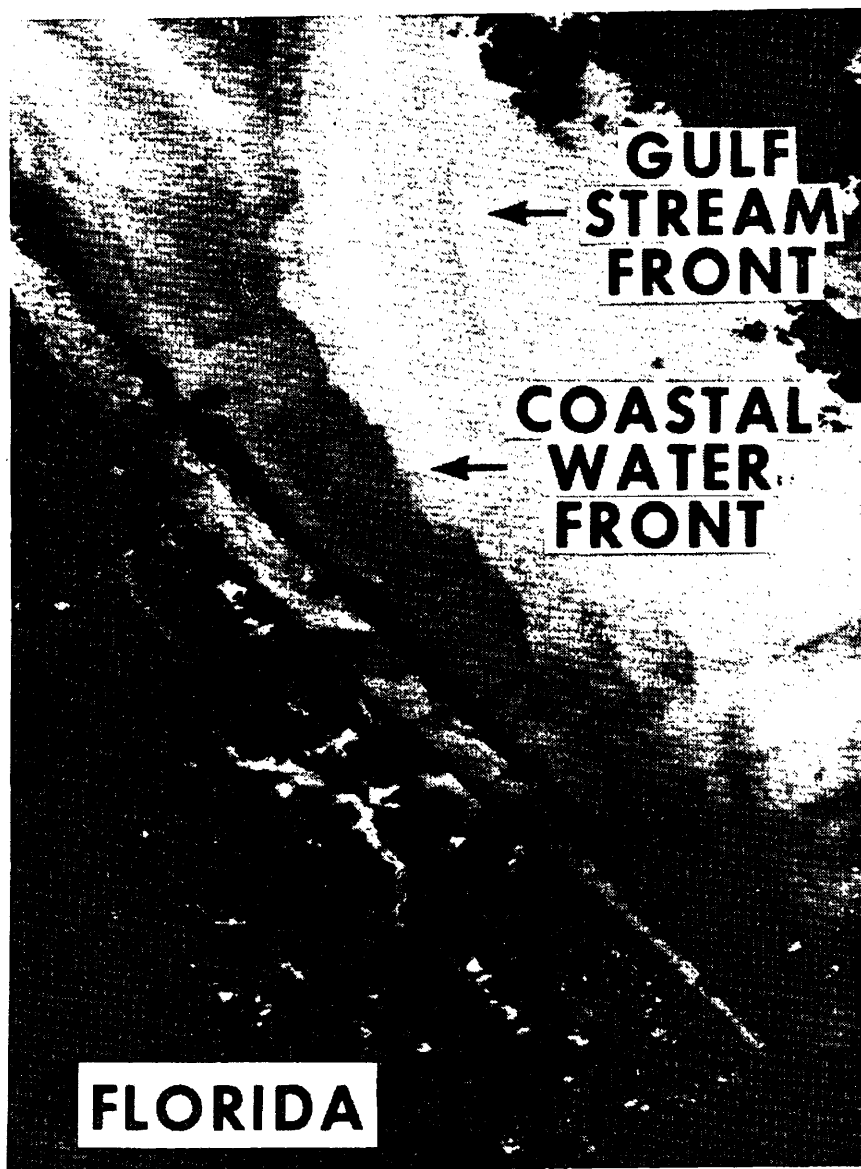


Figure A.9 Contrast-stretched ( $8 \leq \text{DN} \leq 16$ ;  $n=1$ ) negative MSS-5 image of the Florida coast south of Cape Canaveral (ERTS ID 1206-15232), observed on 18 August 1972. Plumes of water from behind the barrier islands can be seen ebbing through the inlets. Complicated patterns of coastal sedimentation show a multifronted boundary between the nearshore water and the Gulf Stream. Changes in the radiance appear to be dominated by changes in suspended sediments. Horizontal distance across the image is 45 km.



Figure A.10 Contrast-stretched ( $7 \leq DN \leq 15$ ;  $n=2$ ) negative MSS-5 image of Cape Lookout, North Carolina, (ERTS ID 1115-15152), observed on 14 November 1972. The shoals offshore of the promitory are shallow and keep sediments in suspension. By comparing the sediment pattern over such areas (cf., fig. A.11), an estimate of the bottom topography can be made and, conversely, the variability of the suspended load as well. There is no evidence of the Gulf Stream front in this image. Horizontal distance across the image is 135 km.

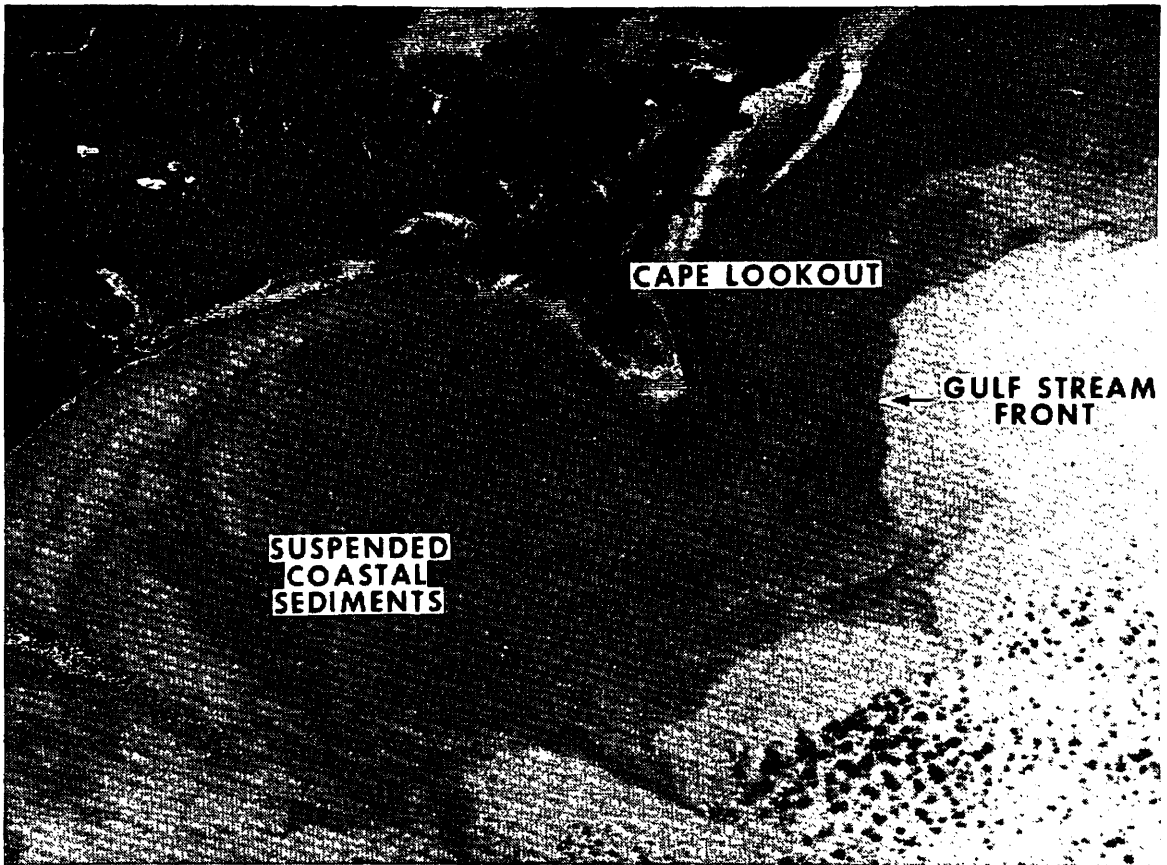


Figure A.11 Contrast-stretched ( $4 \leq \text{DN} \leq 11$ ;  $n=1$ ) negative MSS-5 image of Onslow Bay, North Carolina (ERTS ID 1205-15153), observed on 13 February 1973. Complex patterns of turbidity do not appear to be well correlated with the bottom topography. The white pixels near the coast are an artifact of the contrast stretch routine, wherein the NOAA computer assigns a negative zero to the upper cutoff value ( $\text{DN}=11$  in this case). When the negative zero is reformed onto the digital to analog tape, it inadvertently becomes a maximum value which appears on the image as a white pixel. The scene appears gray because black ( $\text{DN} \geq 11$ ) and white ( $\text{DN}=11$ ) values are intermixed. This does not appear in images with  $n \geq 2$  and has been corrected for. Horizontal scale distance across the image is 135 km.

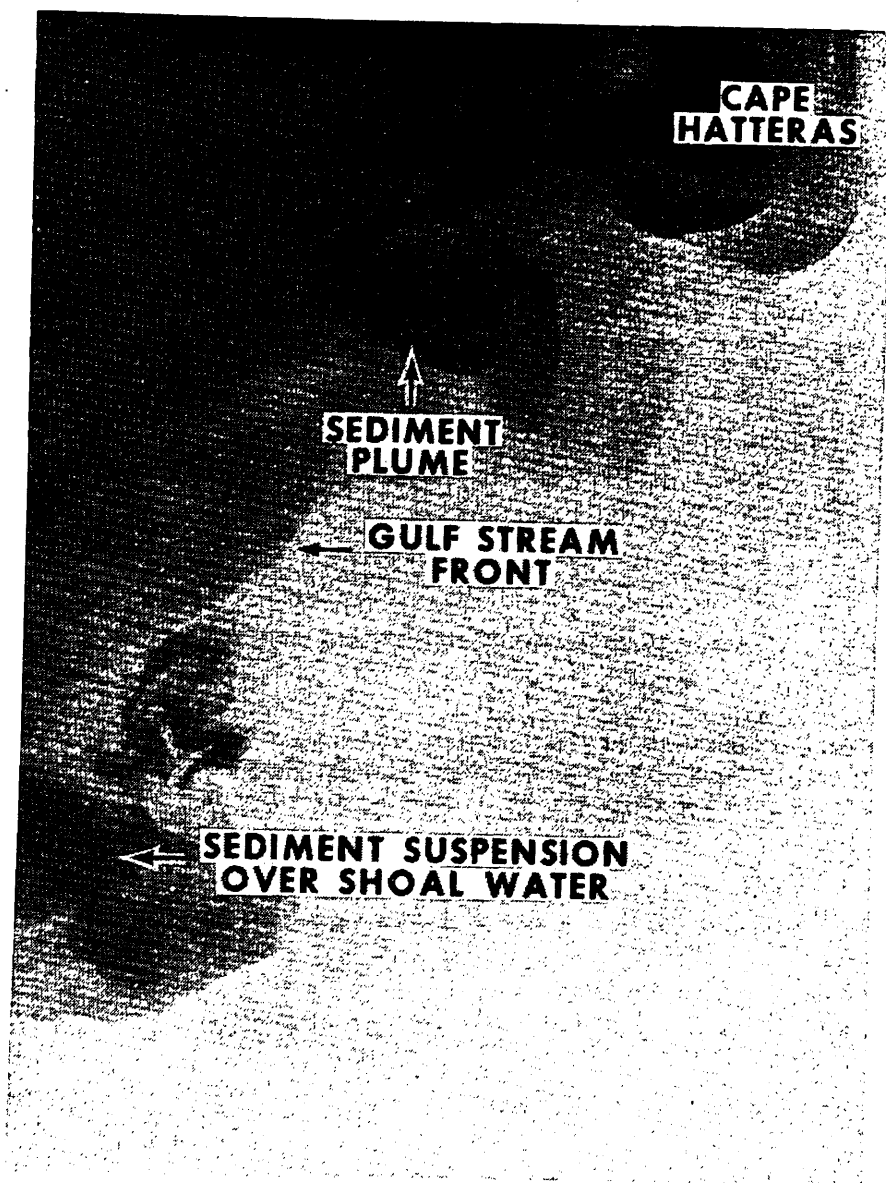


Figure A.12 Contrast-stretched ( $5 \leq DN \leq 13$ ;  $n=2$ ) negative MSS-5 image of the Cape Hatteras, North Carolina area (ERTS ID 1132-15094), observed on 1 December 1972. Mairs (1970) correlated the pulses in the Ocracoke Inlet sediment plume to several stages in the tide. The Cape Hatteras materials are transported from farther north, and an eddy has been observed in several ERTS images in the Hatteras region. Compare again the sediment suspension over Lookout Shoals with the scene in figures A.10 and A.11; detail changes are due to both different stretch limits as well as environmental conditions. Horizontal distance across the image is 90 km.

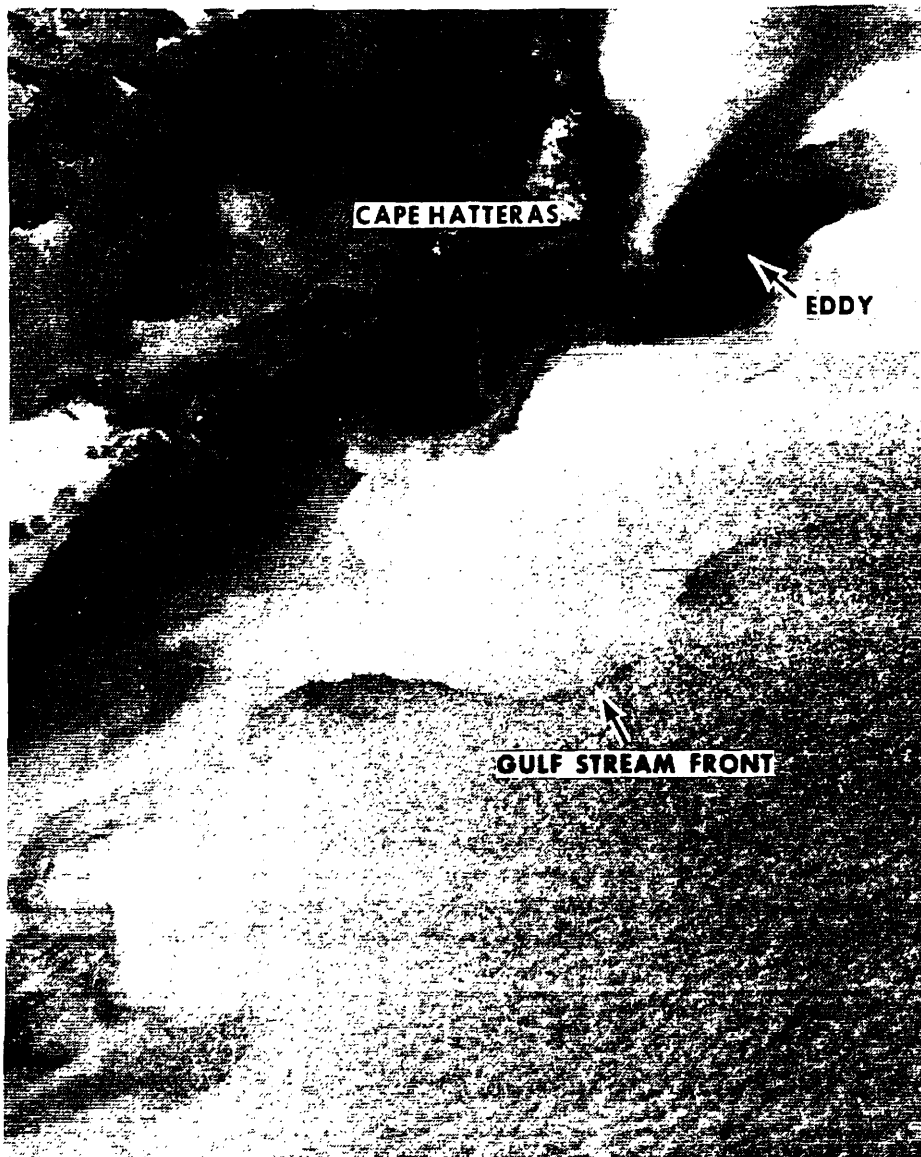


Figure A.13 Contrast-stretched ( $14 \leq DN \leq 22$ ;  $n=2$ ) negative MSS-4 image of an eddy over Diamond Shoals, North Carolina (ERTS ID 1186-15093), observed on 25 January 1973. A deep penetration of water from north of Cape Hatteras can be seen as part of the cyclonic eddy developing over the shoals. The Gulf Stream front appears to be well offshore of the eddy front. Meander scale in the Gulf Stream appears to be about 50 km with an amplitude of about 10 km. Details in the sediment suspension patterns support the notion of multiple fronts, probably tidally pumped and advected by alongshore current patterns. Streaks can be seen in the current at the lower right and may be internal wave activity. Horizontal distance across the image is 90 km.

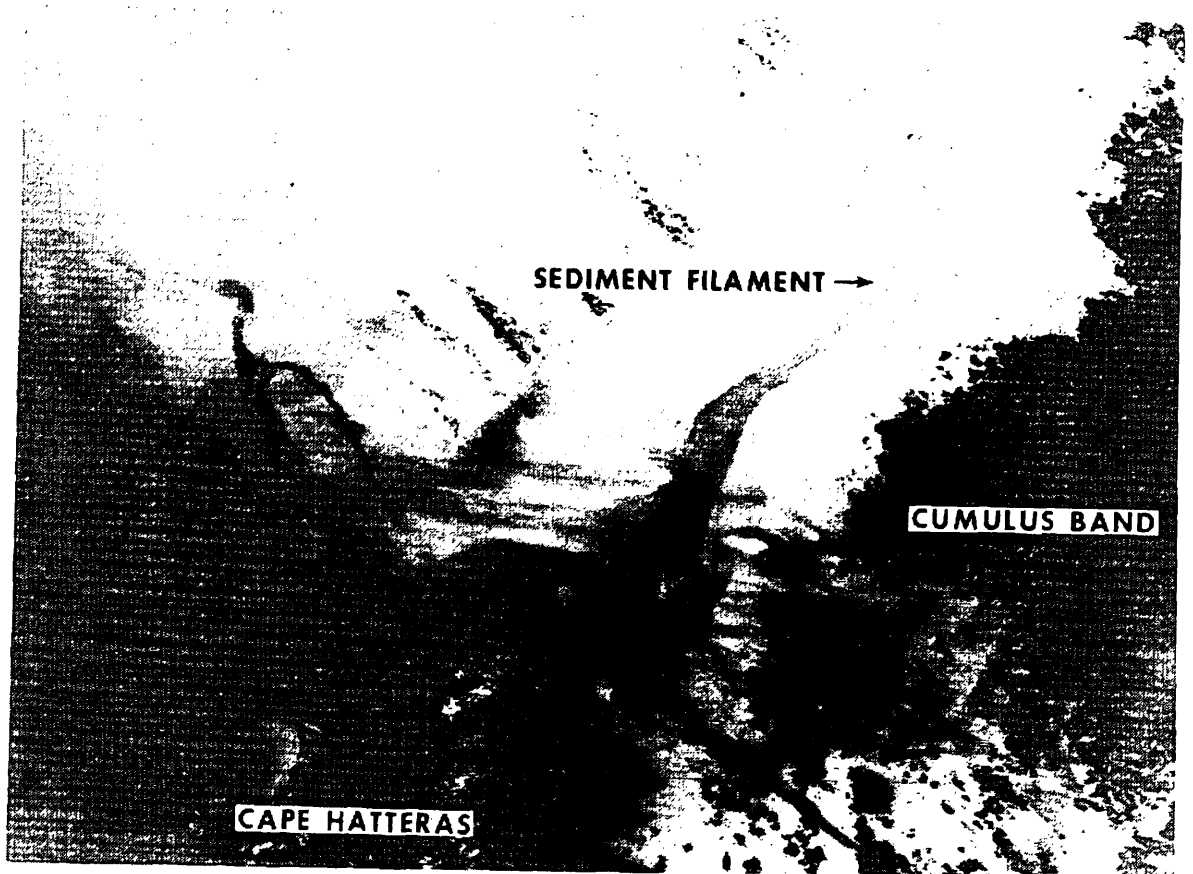


Figure A.14 Contrast-stretched ( $7 \leq DN \leq 15$ ;  $n=2$ ) negative MSS-5 image of a sediment filament in the offing of Cape Hatteras, North Carolina (ERTS ID 1222-15093), observed on 2 March 1973. The squaring in the stretch equation overaccentuates the low radiance features so that details at Cape Hatteras are lost; generally  $n=1$  is a better choice because it is linear with radiance for spectral comparison purposes. The sediment filament extends 120 km off-shore and is probably material from Pamlico Sound as Ford, Longard, and Banks (1952) have suggested in their entrainment studies. Horizontal distance across the image is 135 km.

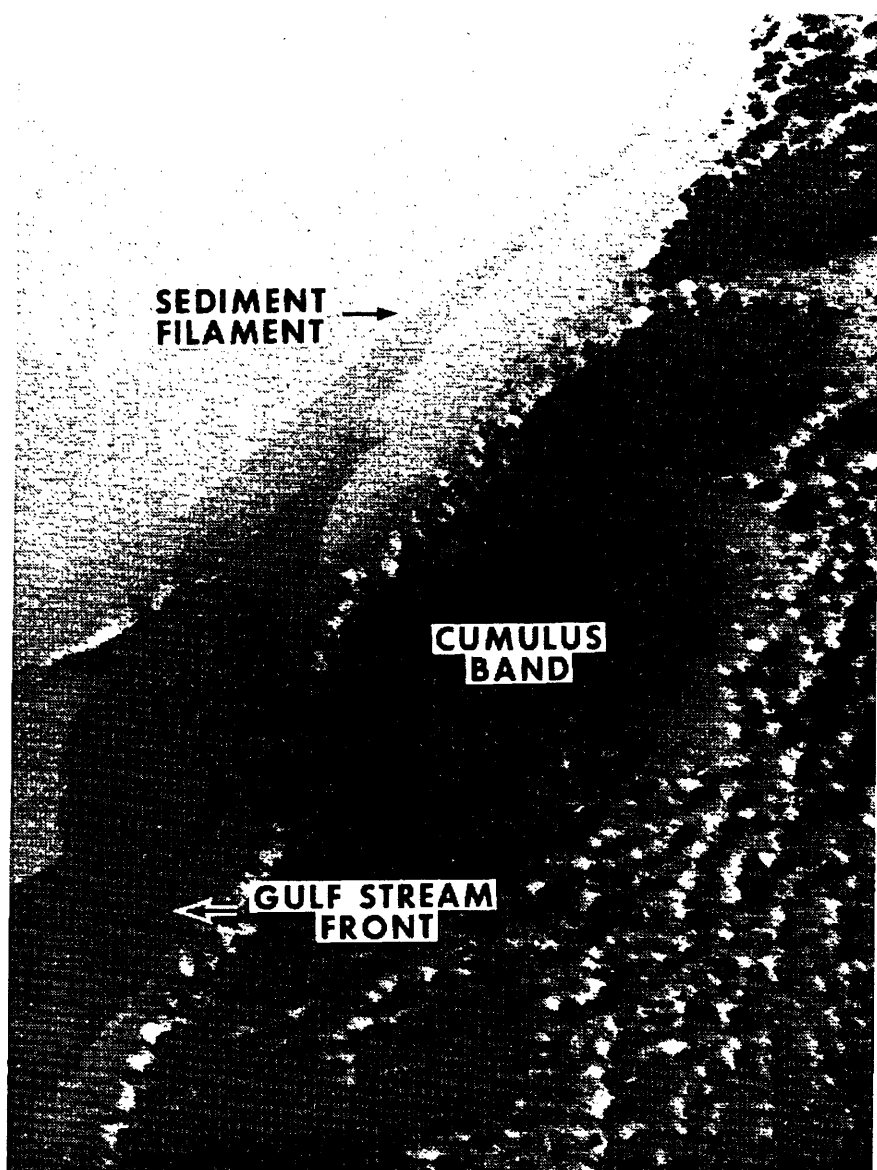


Figure A.15 Contrast-stretched ( $16 \leq \text{DN} \leq 24$ ;  $n=3$ ) negative MSS-4 image of the Gulf Stream in deep water off Cape Hatteras (ERTS ID 1221-15035), observed on 1 March 1973. Taken 1 day earlier than figure A.14, this plume is over 180 km long on this image and extends over 300 km from Cape Hatteras. The cumulus band is a frequent feature of the stream from space and is caused by the convection when cool dry continental air is heated by the stream. This feature follows the Gulf Stream front quite well as seen in the image and can be used as an ancillary feature for identification of the stream. Horizontal distance across the image is 90 km.



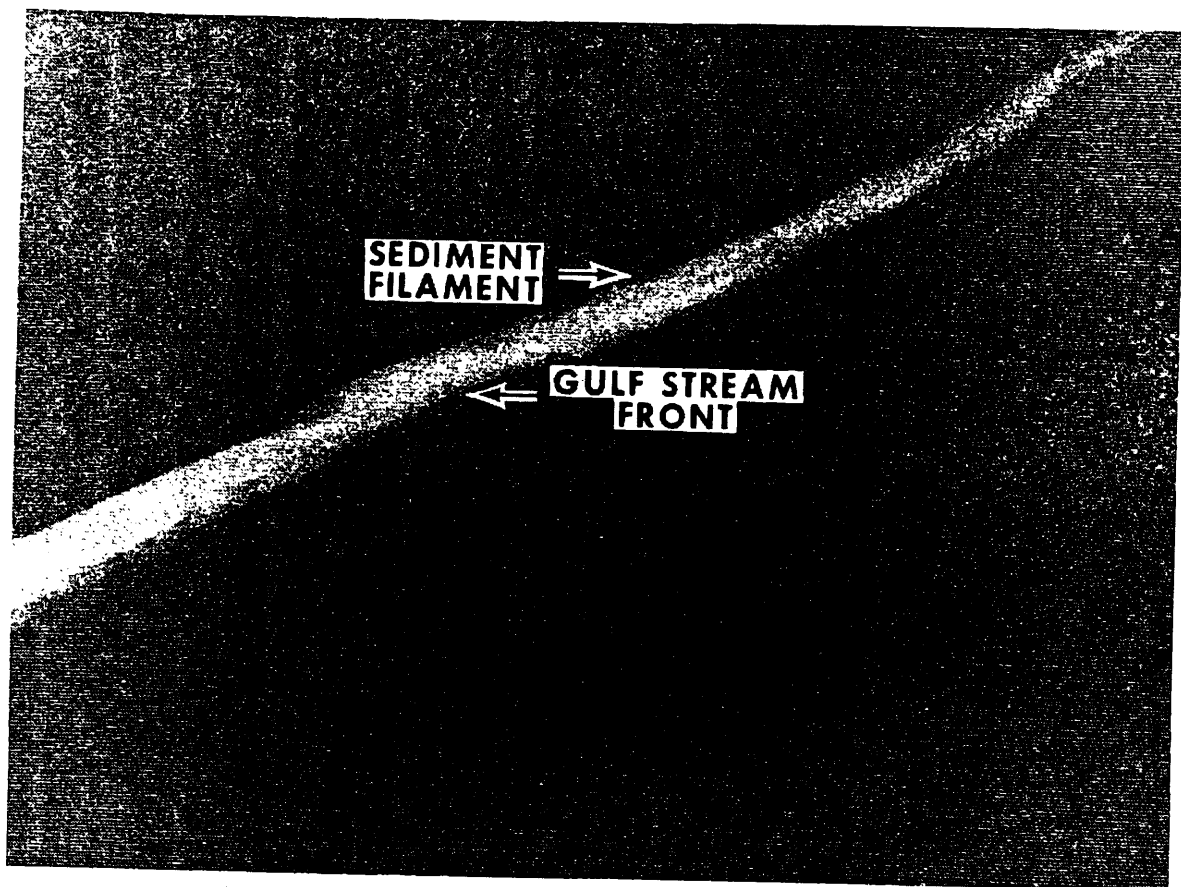


Figure A. 16 Contrast-stretched ( $12 \leq \text{DN} \leq 16$ ;  $n=1$ ) negative MSS-4 image of a sediment filament offshore of Cape Hatteras, North Carolina (ERTS ID 1149-15033), observed on 19 December 1972. This image was observed 17 days later than the data in figure A.2, but is an almost perfect extension of that sediment filament and about 270 km to sea. Note the DN limits have a range of only 5. The Gulf Stream waters are at the same intensity as the waters north of the sediment filament, and the stream is observable only because little small-scale mixing has occurred across the boundary. Horizontal distance across the image is 135 km.



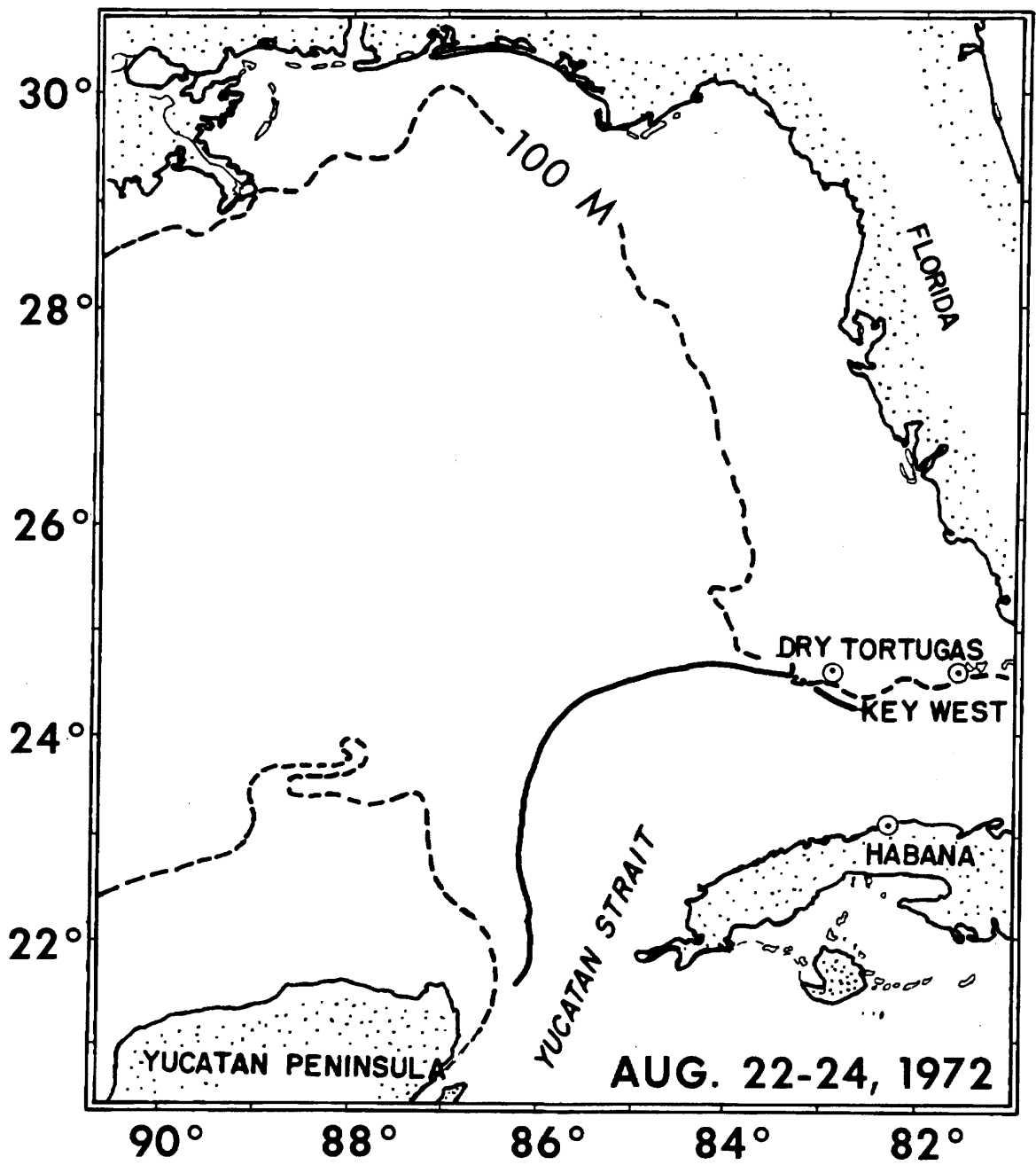
**GULF STREAM  
FRONT** →

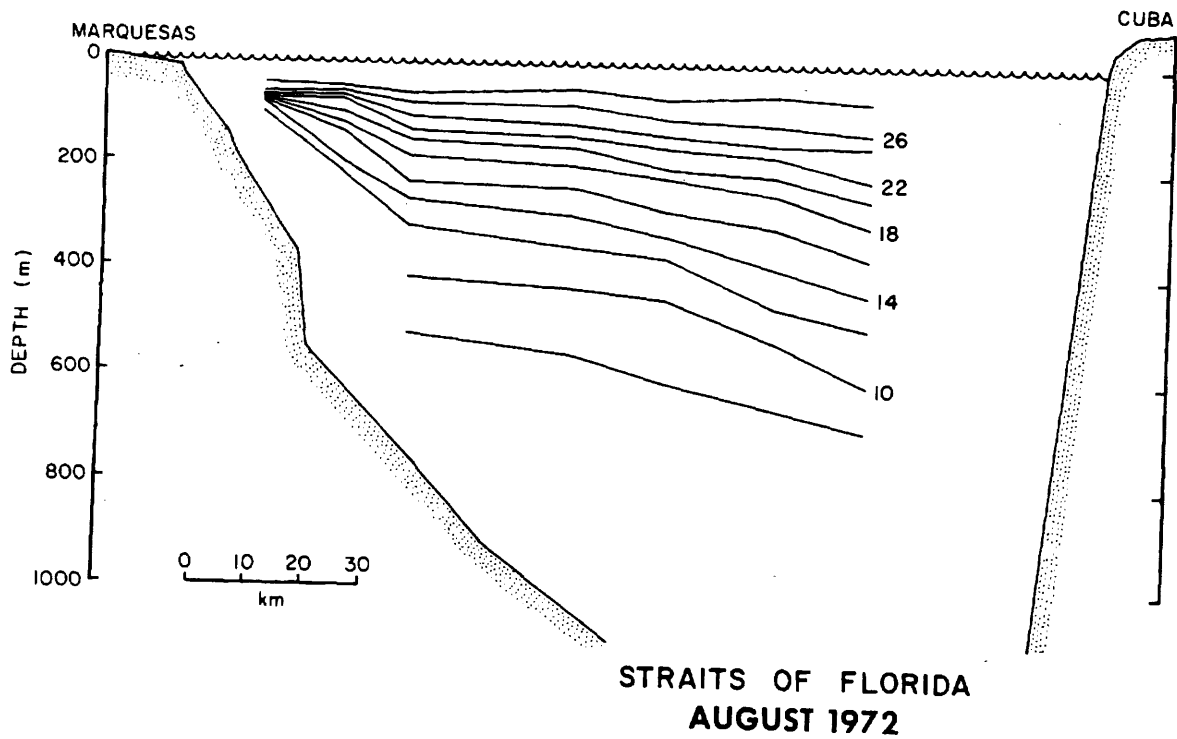
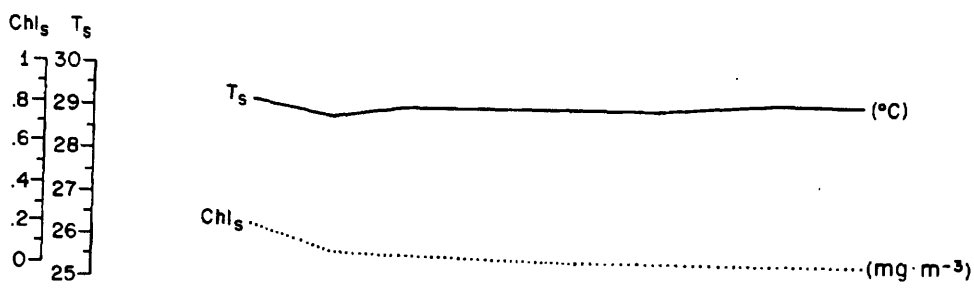
Figure A.17 Contrast-stretched ( $11 \leq DN \leq 15$ ;  $n=1$ ) negative MSS-5 image of the Gulf Stream off Delaware (ERTS ID 1257-15033), observed on 6 April 1973. The stream is observable in this case due to higher radiance caused by increased sea state in the flow. This image is 350 km northeast of Cape Hatteras. There is a hazard in using sea state only to identify the current because, even in MSS-7, a slight increase in radiance occurs which could be caused by high thin cirrus clouds. Horizontal distance across the image is 135 km.

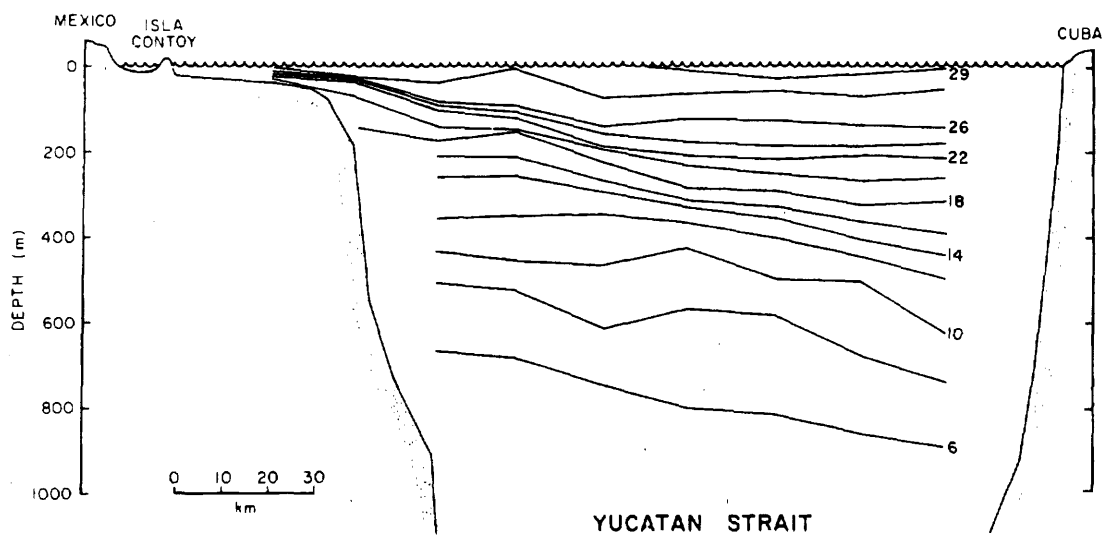
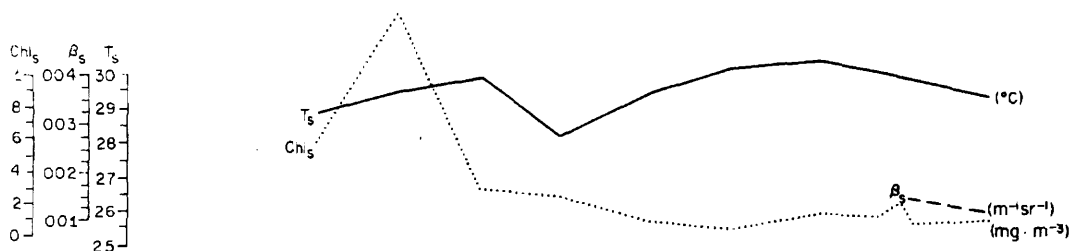
## APPENDIX B

Details of the time series presented in figure 3.2, and the cross-section from which table 3.1 was tabulated, are presented in this appendix. As described before, the solid line on the chart of the Gulf of Mexico represents the  $22^{\circ}\text{C}$  isotherm at 100 m. This stretch of the  $22^{\circ}\text{C}$  isotherm is presented first in the three figures for each cruise (except January 1973 which has two figures). The second figure is the transect of the Straits of Florida showing the surface values of temperature ( $T_s, ^{\circ}\text{C}$ ), volume-scattering function ( $\beta_s$ ) at  $45^{\circ}$  using a blue (436 nm) filter ( $\text{m}^{-1} \text{sr}^{-1}$ ), and chlorophyll-a ( $\text{Chl}_s$ ) observed by the method of Lorenzen (1966) at the surface ( $\text{mg m}^{-3}$ ). Temperature and chlorophyll were continuous observations, whereas volume scattering was observed at each STD station. The third figure of each section is the transect data for the Yucatan Strait, in the same format as for the Straits of Florida. In general, seven STD stations at ~18 km spacing were taken in the Straits of Florida, and nine stations were required in the Yucatan Strait; the cross sections of the temperature field ( $^{\circ}\text{C}$ ) are given below the surface variables.

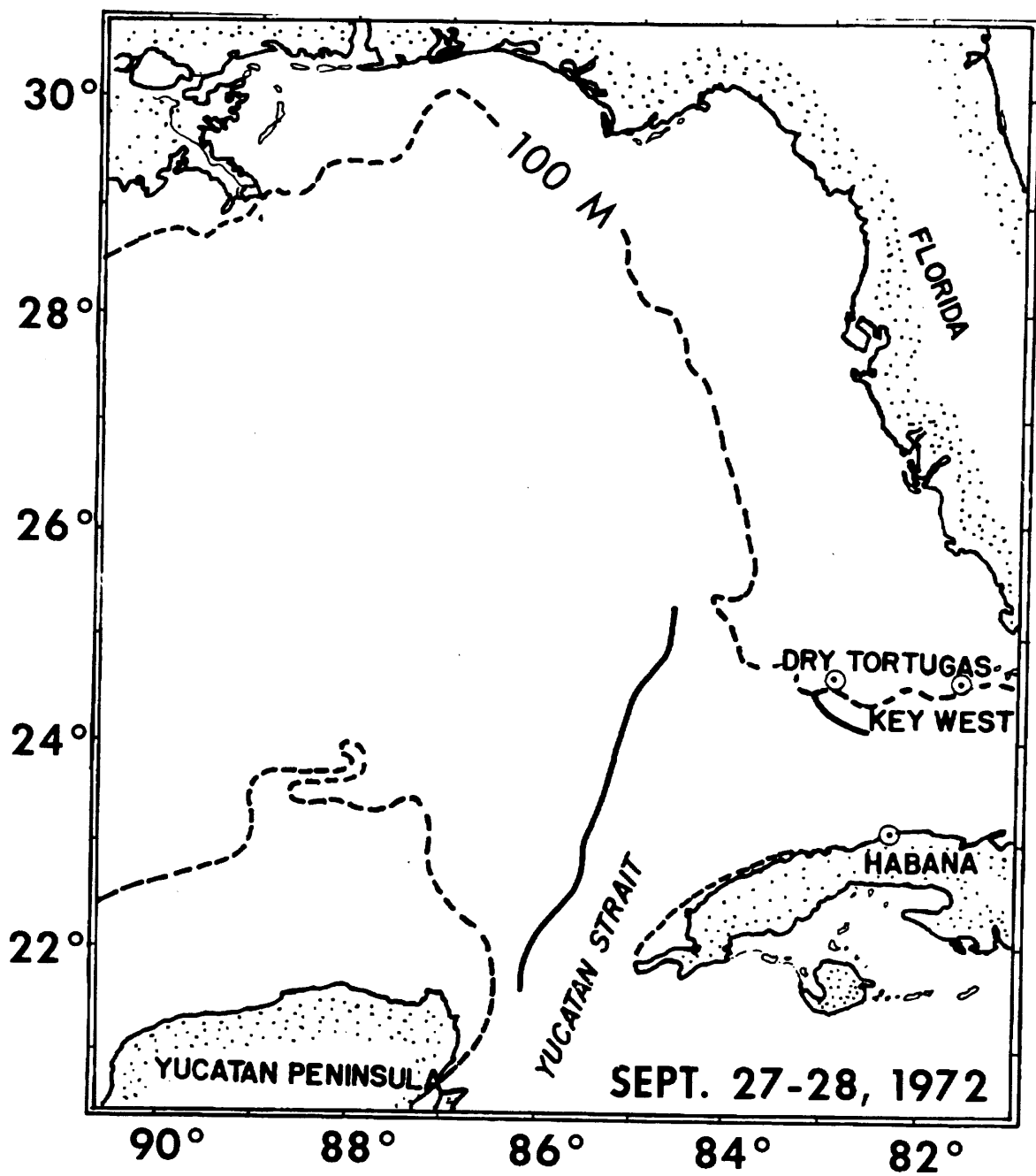
Dates on the charts showing the location of the indicator isotherm represent the time required to track the  $22^{\circ}\text{C}$  @ 100 m from Yucatan to Florida. In 1972, the cruises originated in St. Petersburg, and the Yucatan section (which required about 24 hr) was observed immediately preceding the tracking; the Straits of Florida section also required about 24 hr and was done 1 day after the transect was completed. In January 1973, foul weather prevented observing the section in the Straits, however, a suborbital track section from  $25^{\circ}55'\text{N}$ ,  $84^{\circ}40'\text{W}$  to  $23^{\circ}26'\text{N}$ ,  $85^{\circ}20'\text{W}$  was observed. Chlorophyll-a and volume-scattering function were not observed because of equipment failure and rough seas. The remaining cruises originated in Miami, and the Straits of Florida section was observed prior to the tracking; approximately 24 hr were required to reach Cabo San Antonio from Habana. The Straits of Florida section is also a suborbital trackline that was occupied within a day or two of satellite transit. All standard hydrographic data presented herein are on file at NODC.

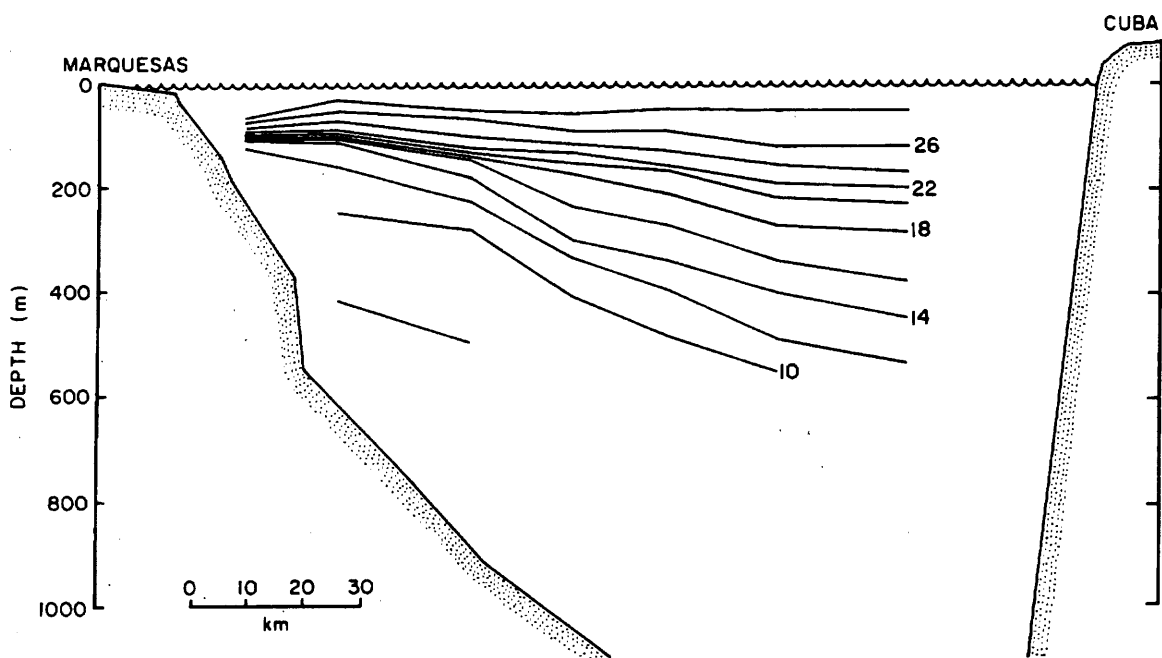
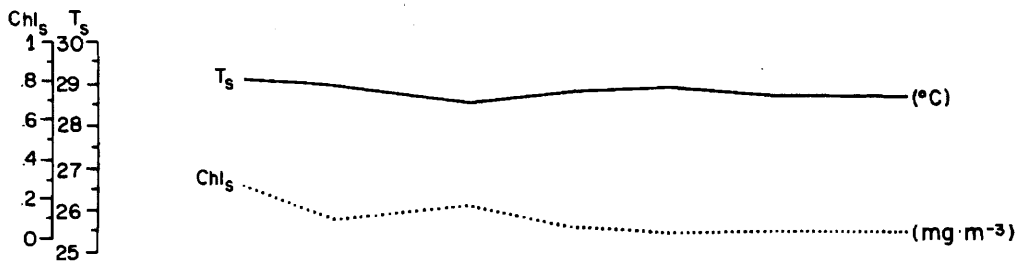






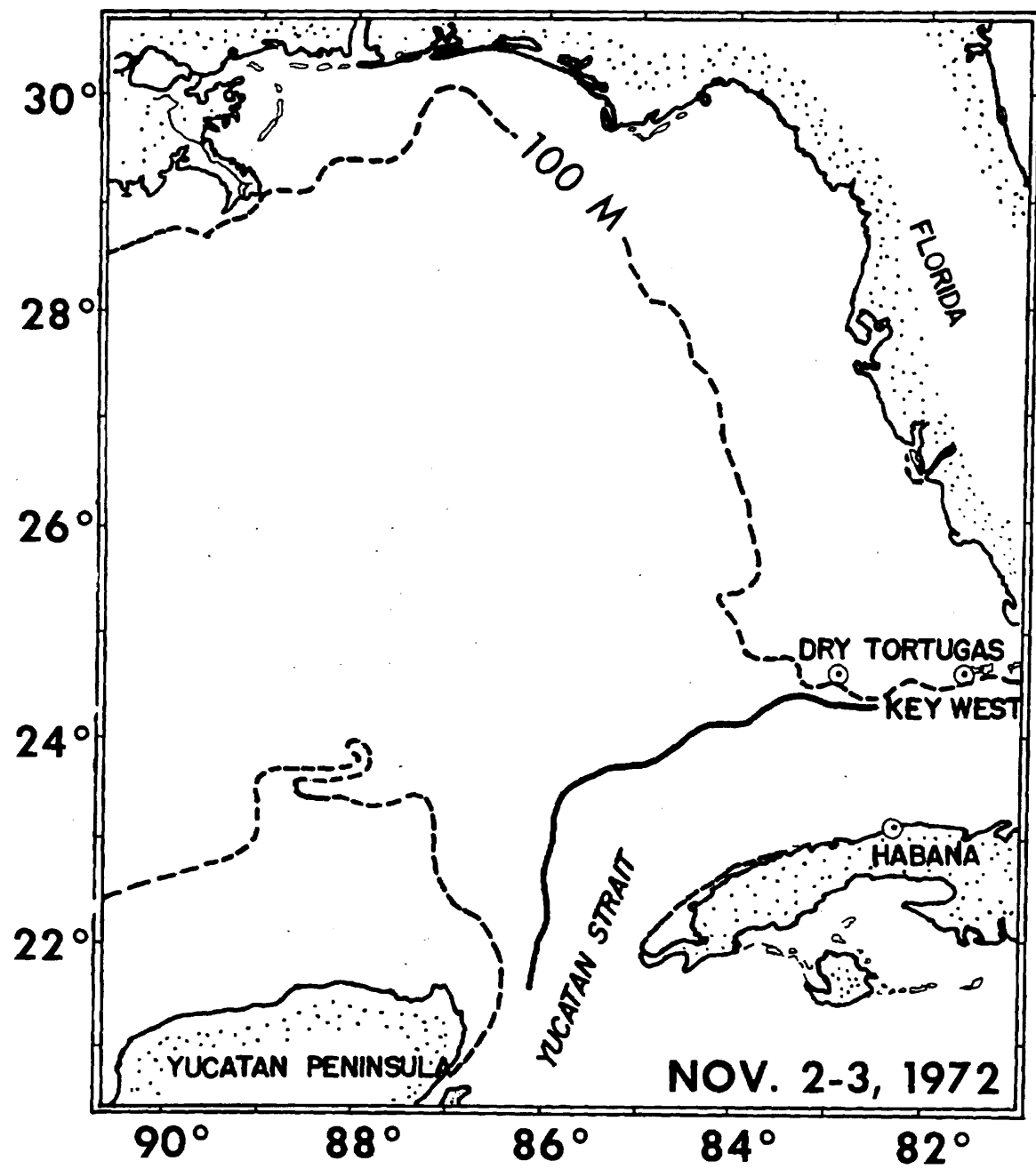
YUCATAN STRAIT  
AUGUST 1972

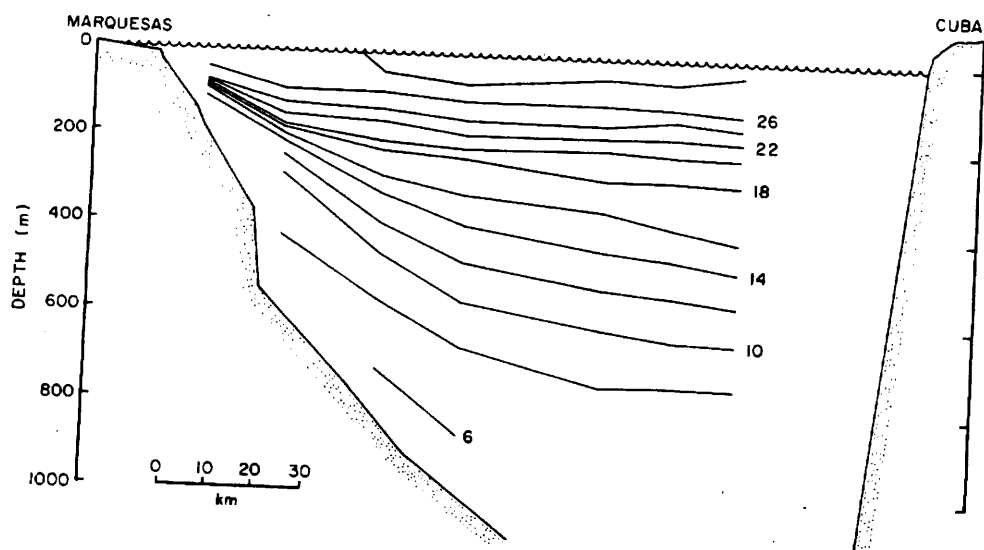
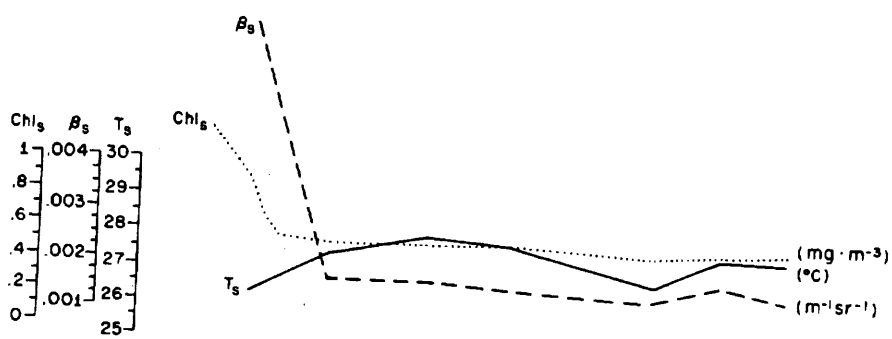




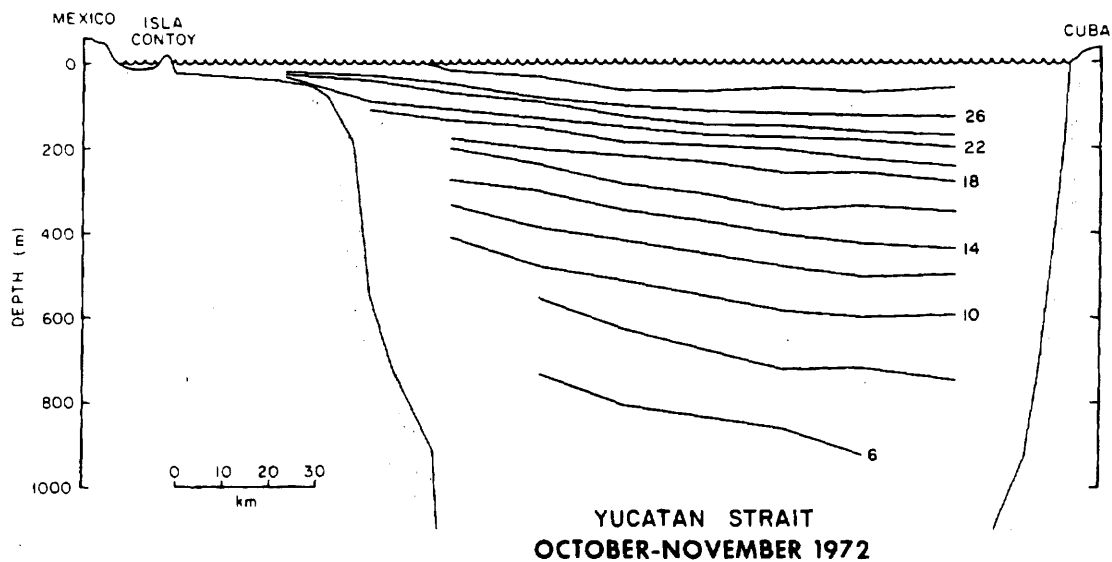
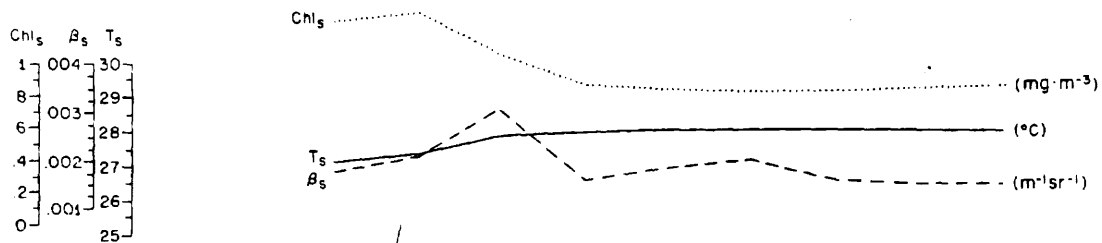
STRAITS OF FLORIDA  
SEPTEMBER 1972

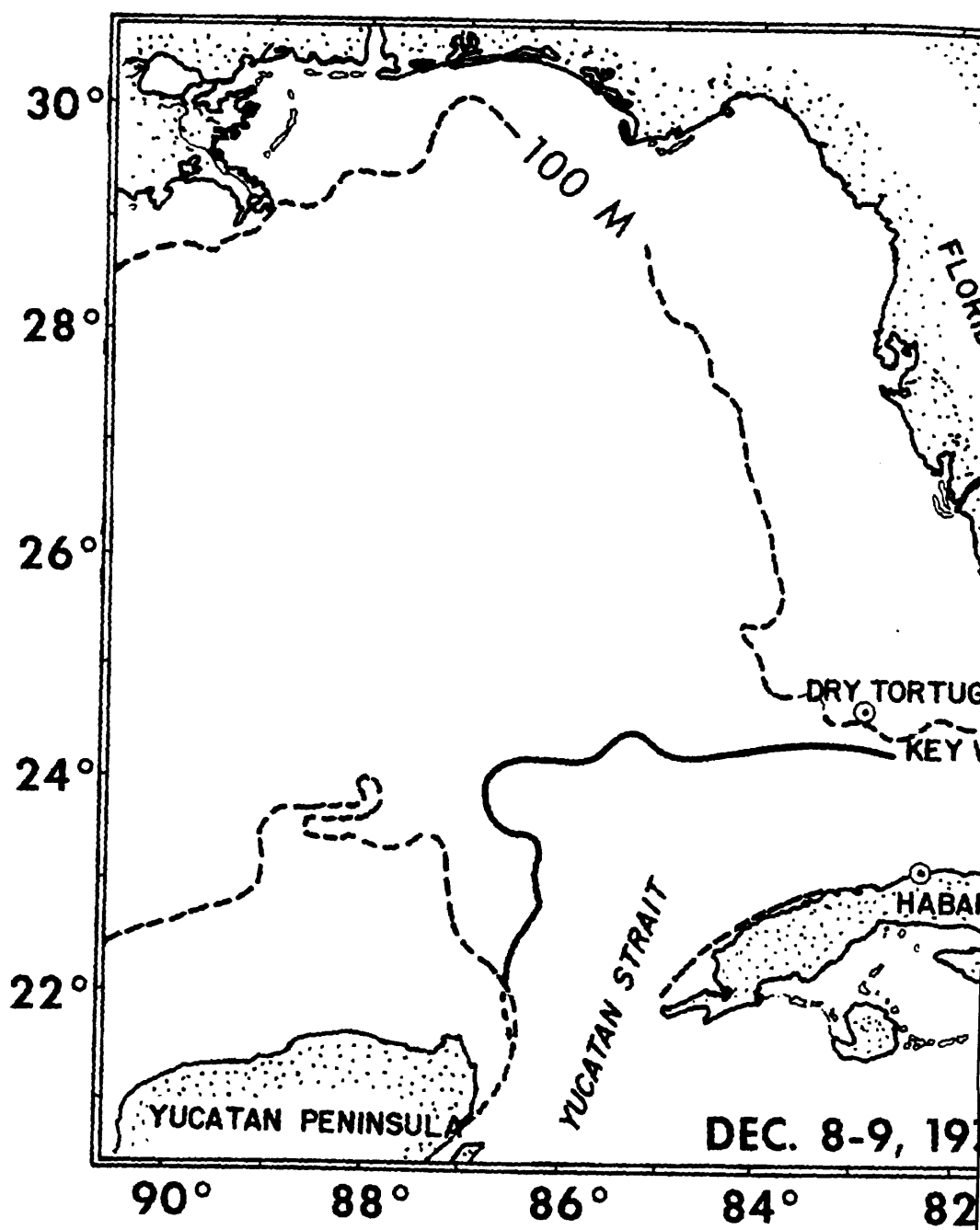


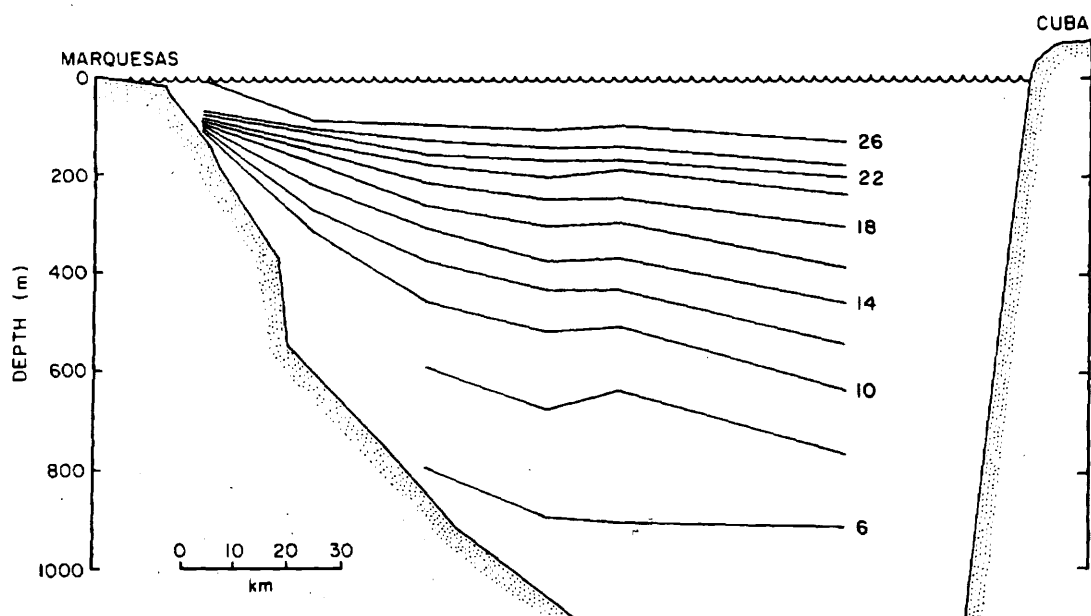
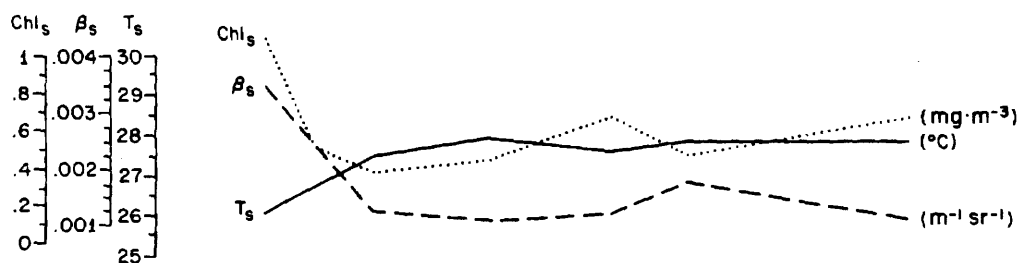




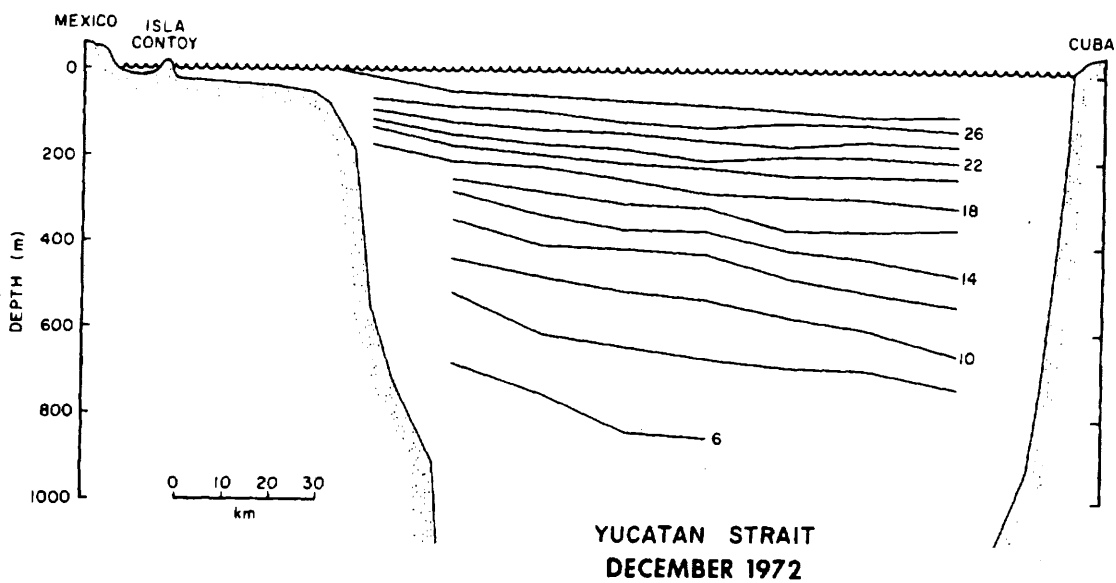
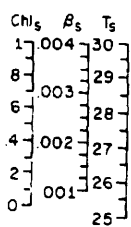
STRAITS OF FLORIDA  
 OCTOBER-NOVEMBER 1972

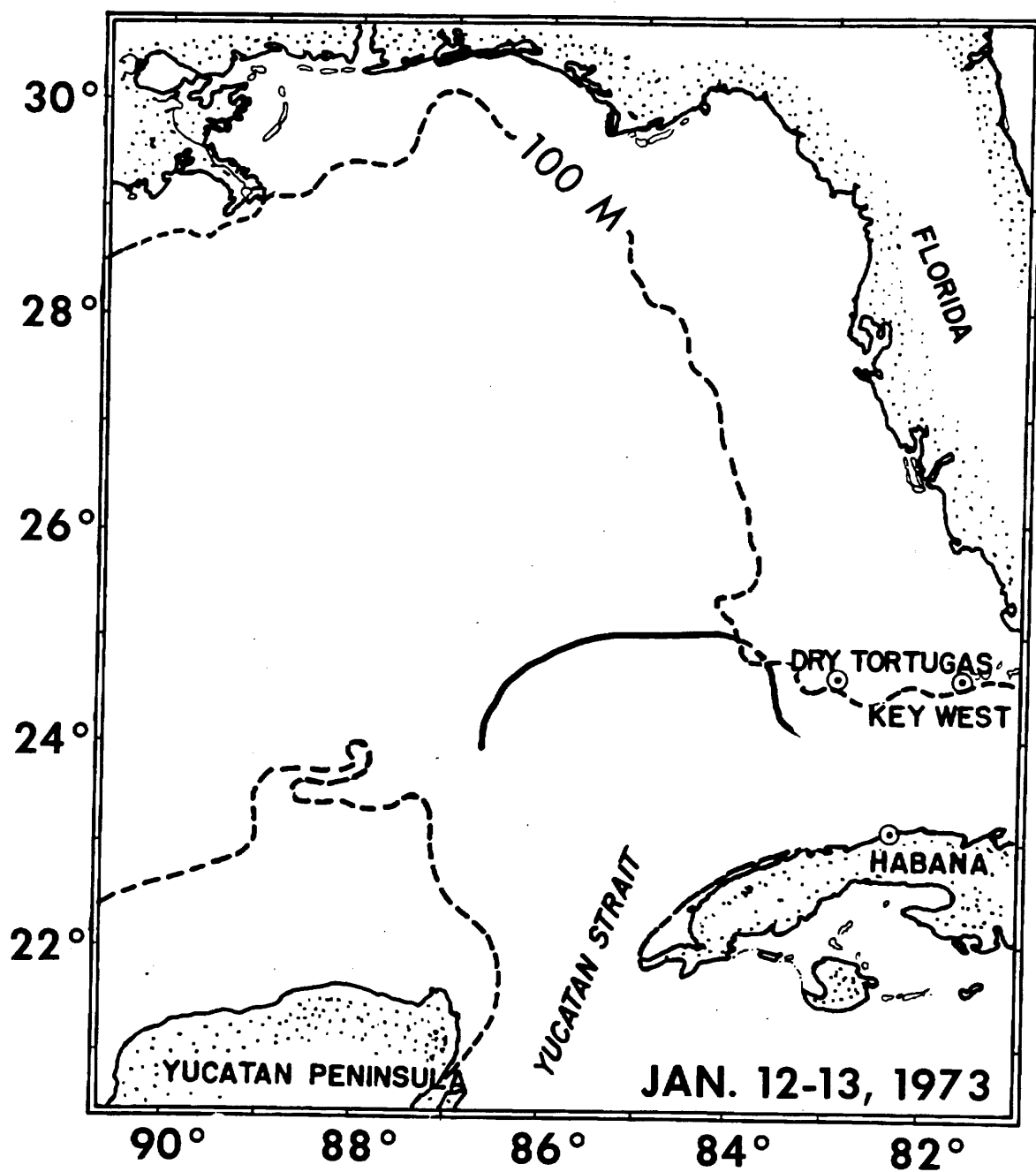






STRAITS OF FLORIDA  
 DECEMBER 1972





SURF SALINITY

36.5  
36.0  
35.5

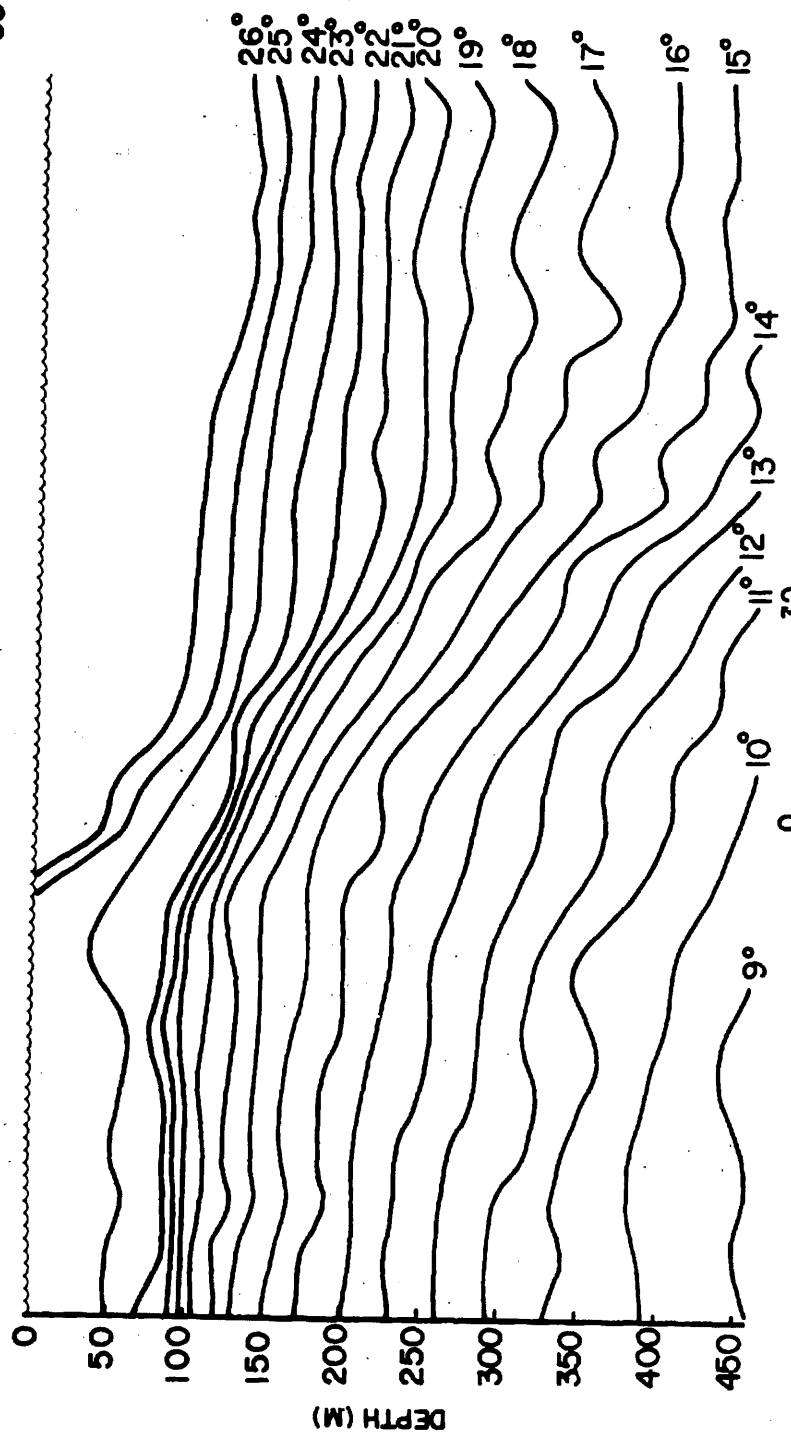
$T_s$

28  
26  
24

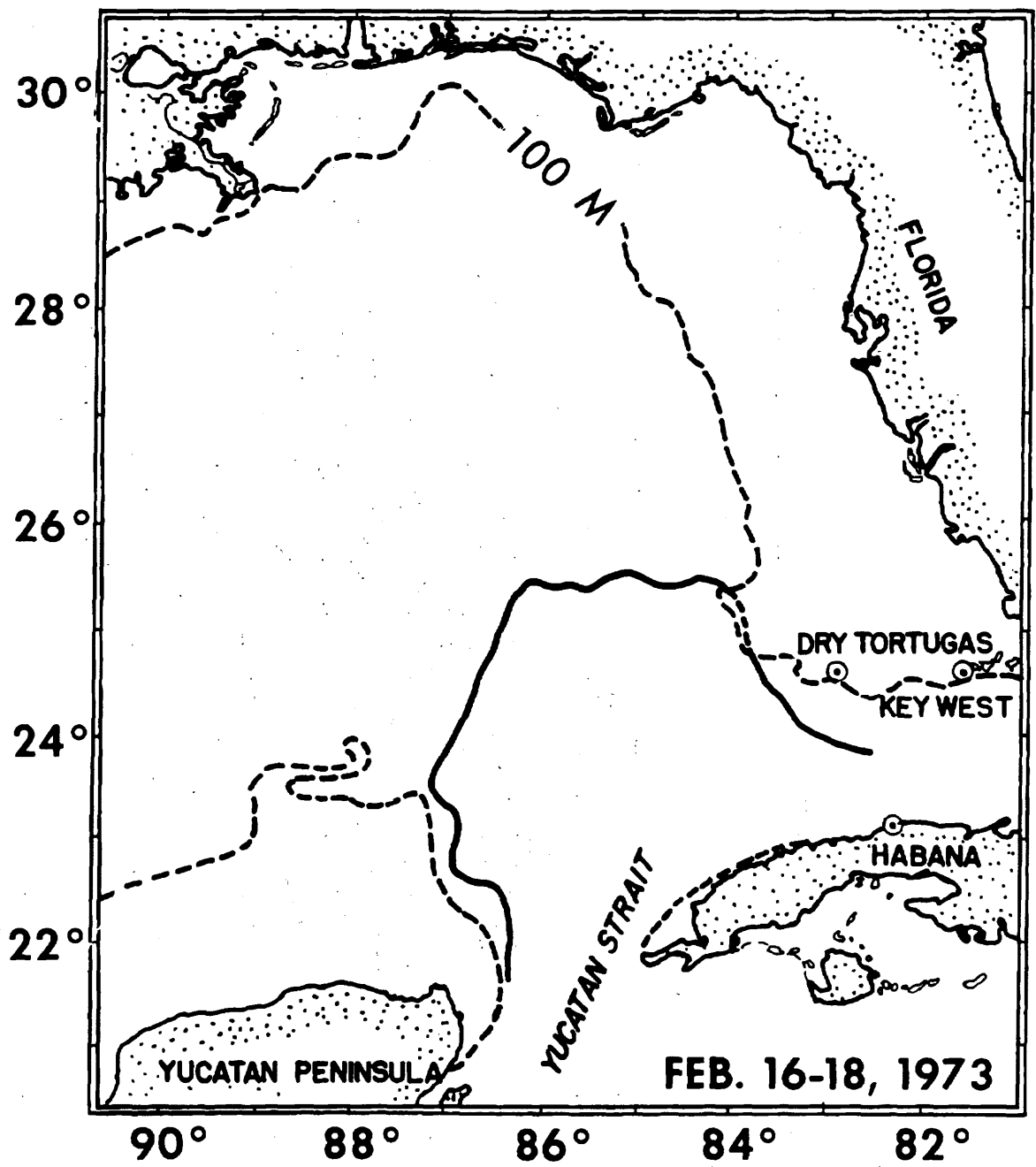
--- BUCKET TEMPERATURE  
— RADIATION TEMPERATURE

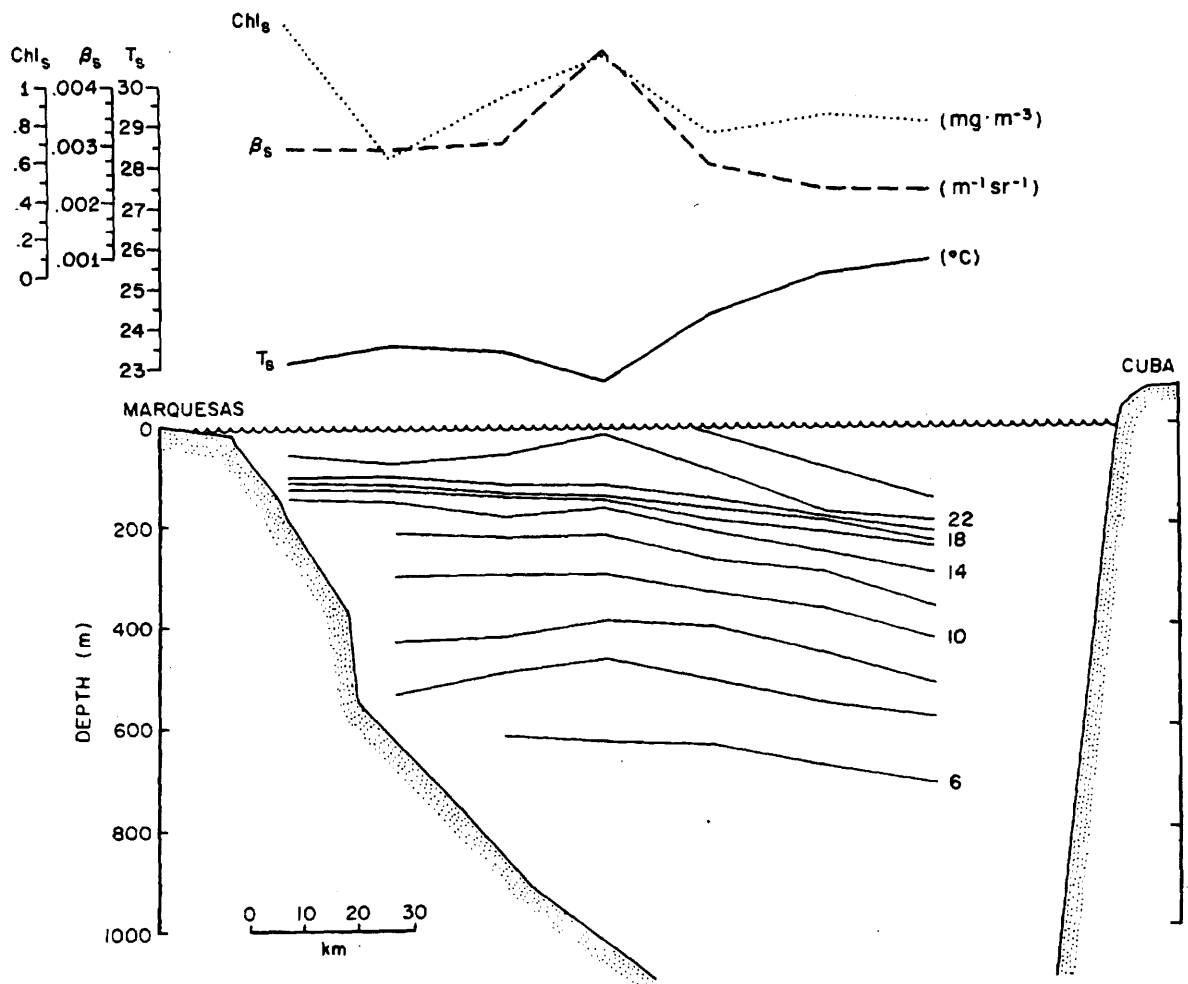
25° 55' N  
84° 40' W

23° 26' N  
85° 20' W

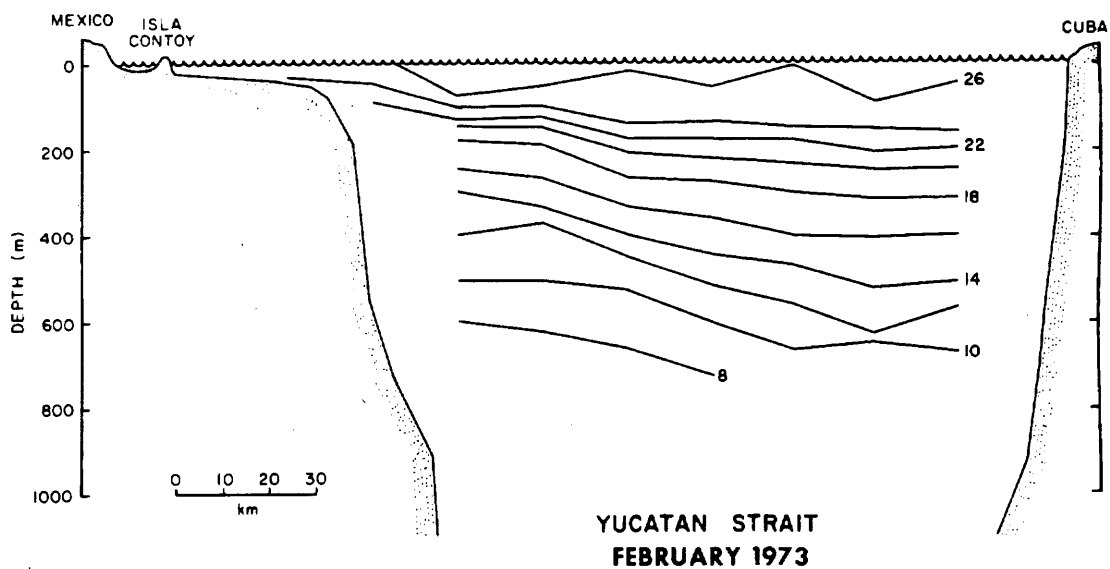
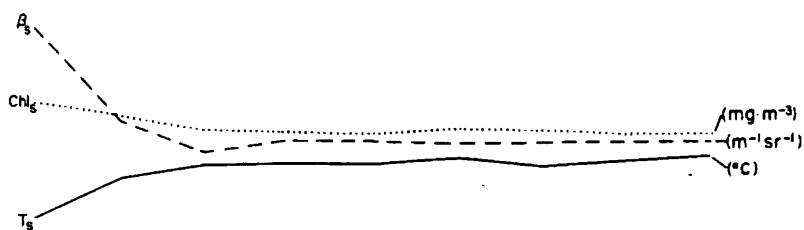
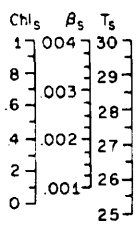


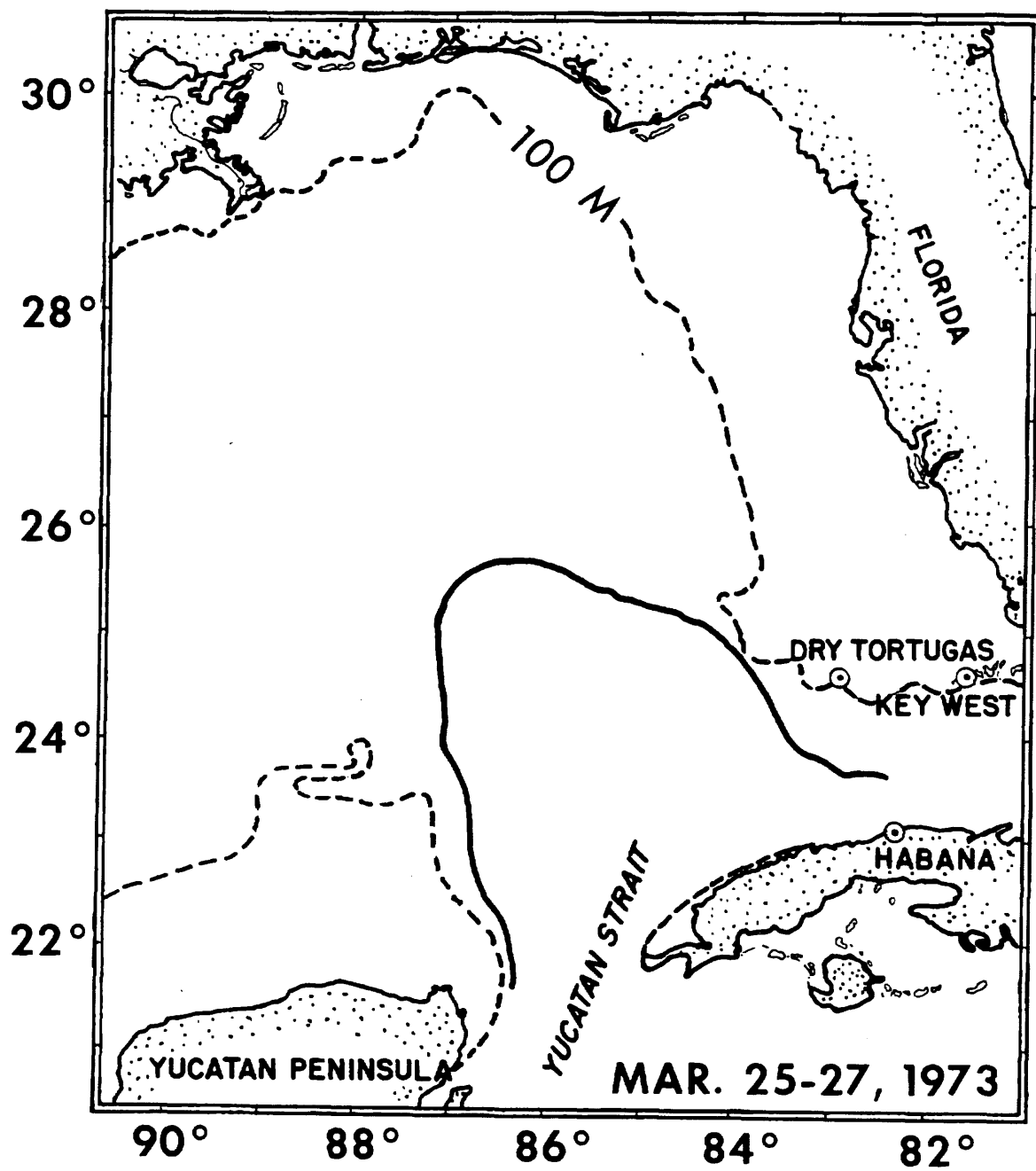


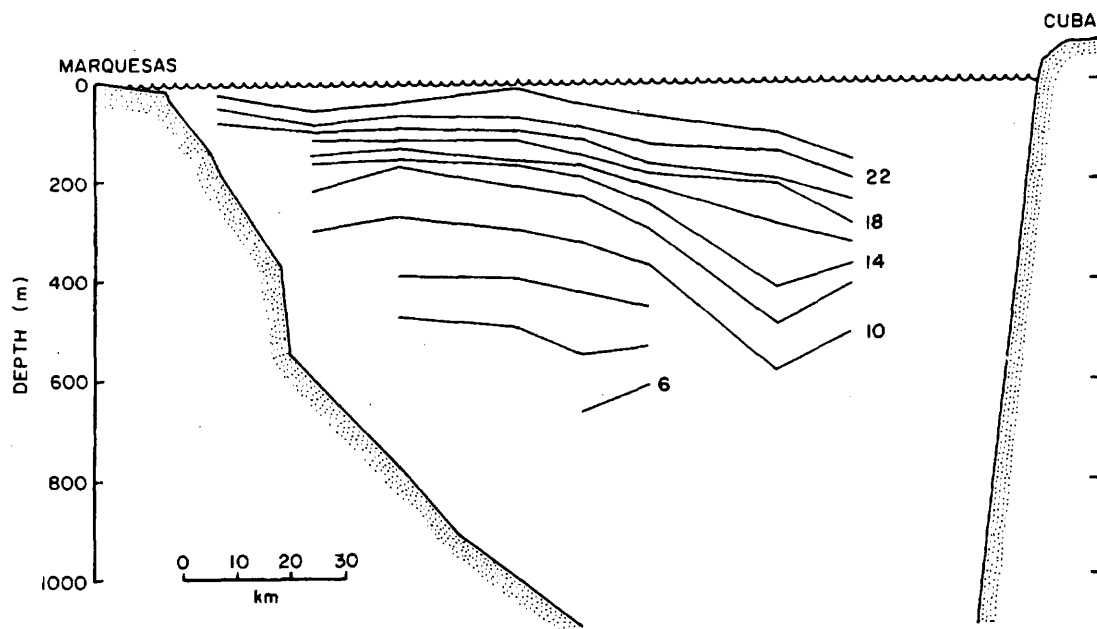
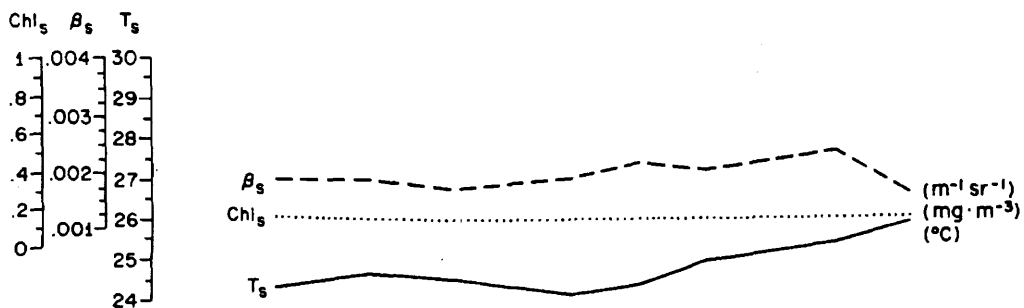




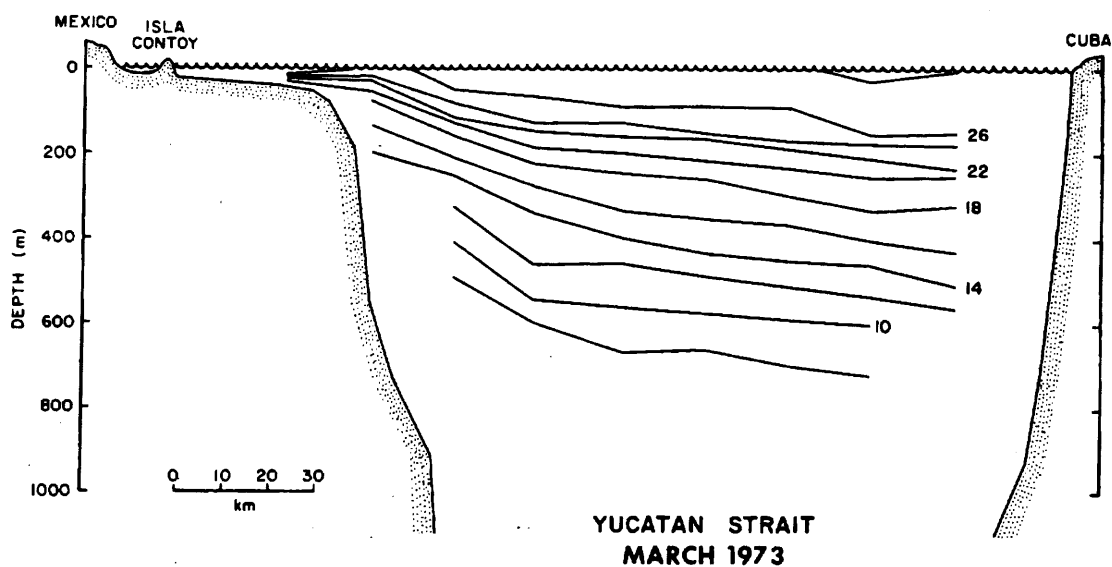
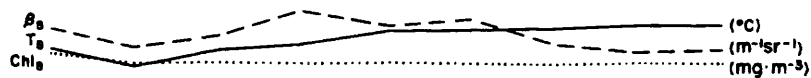
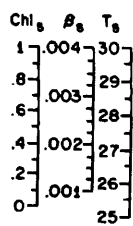
STRAITS OF FLORIDA  
FEBRUARY 1973

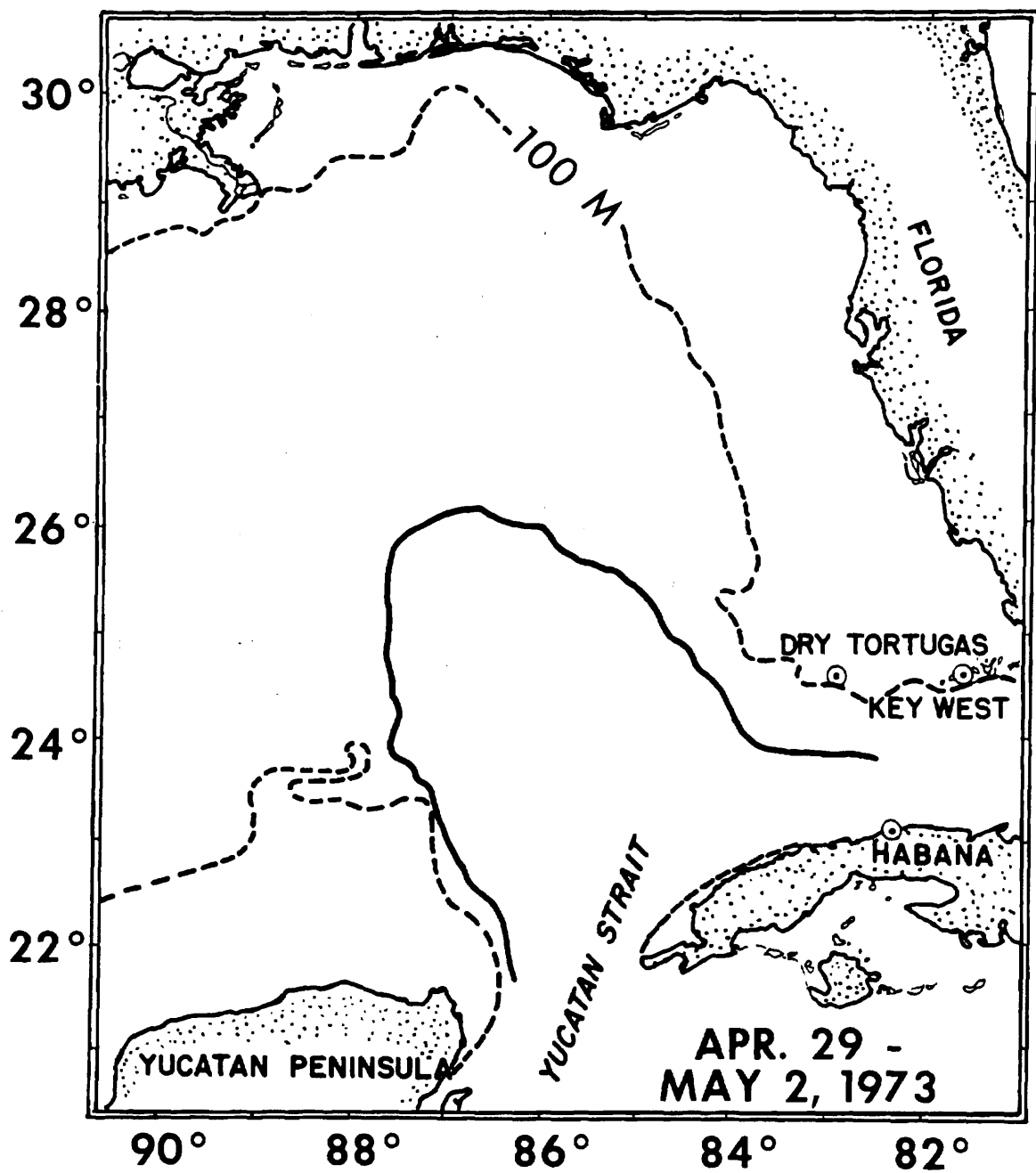


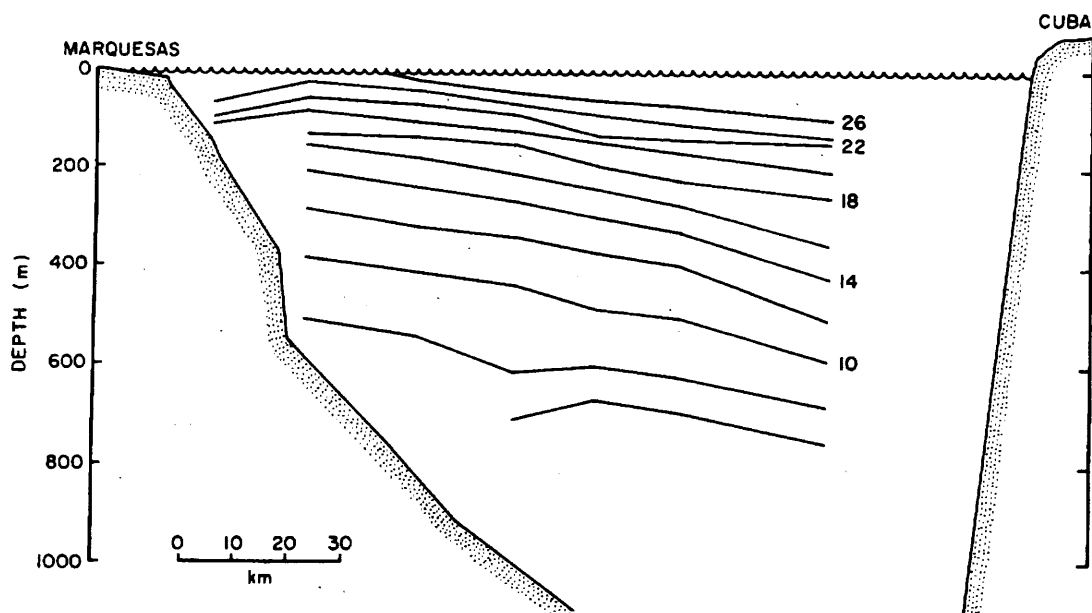
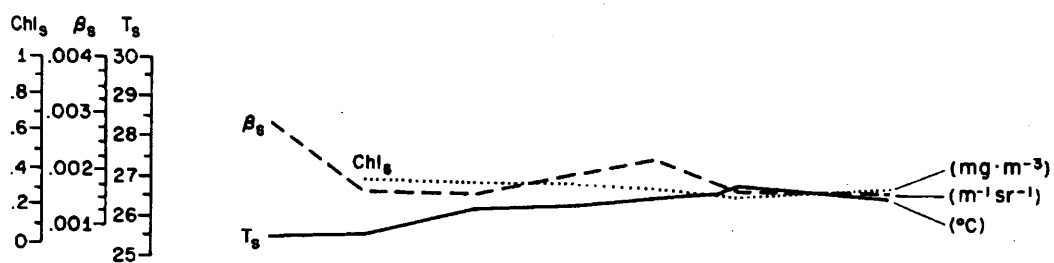




STRAITS OF FLORIDA  
MARCH 1973

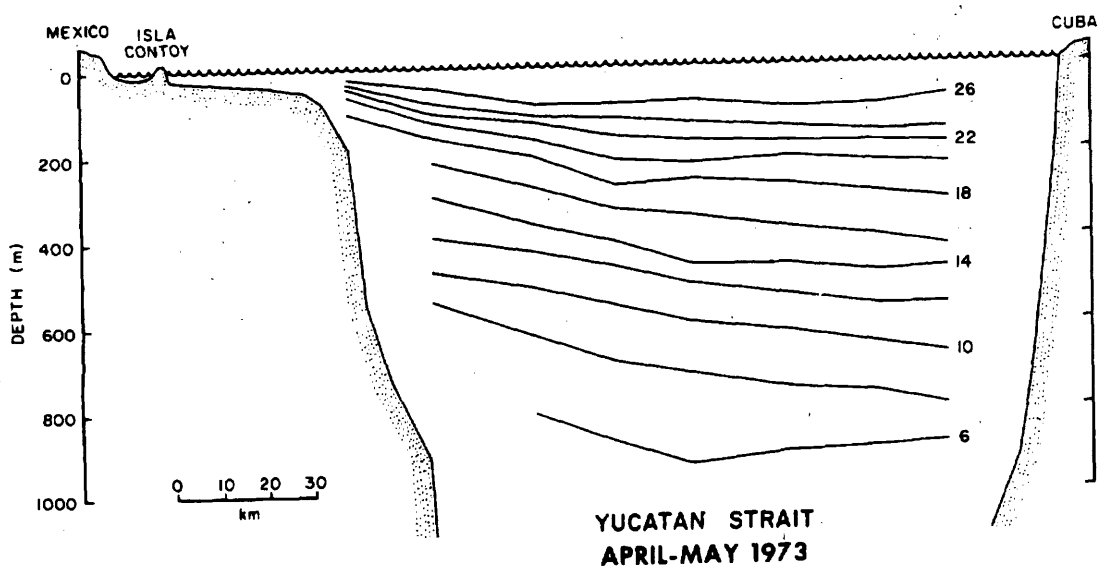
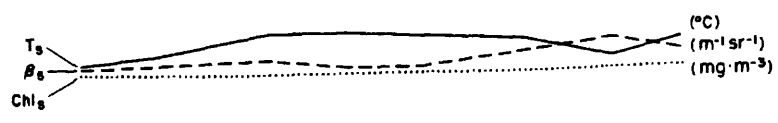
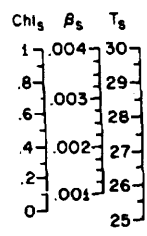


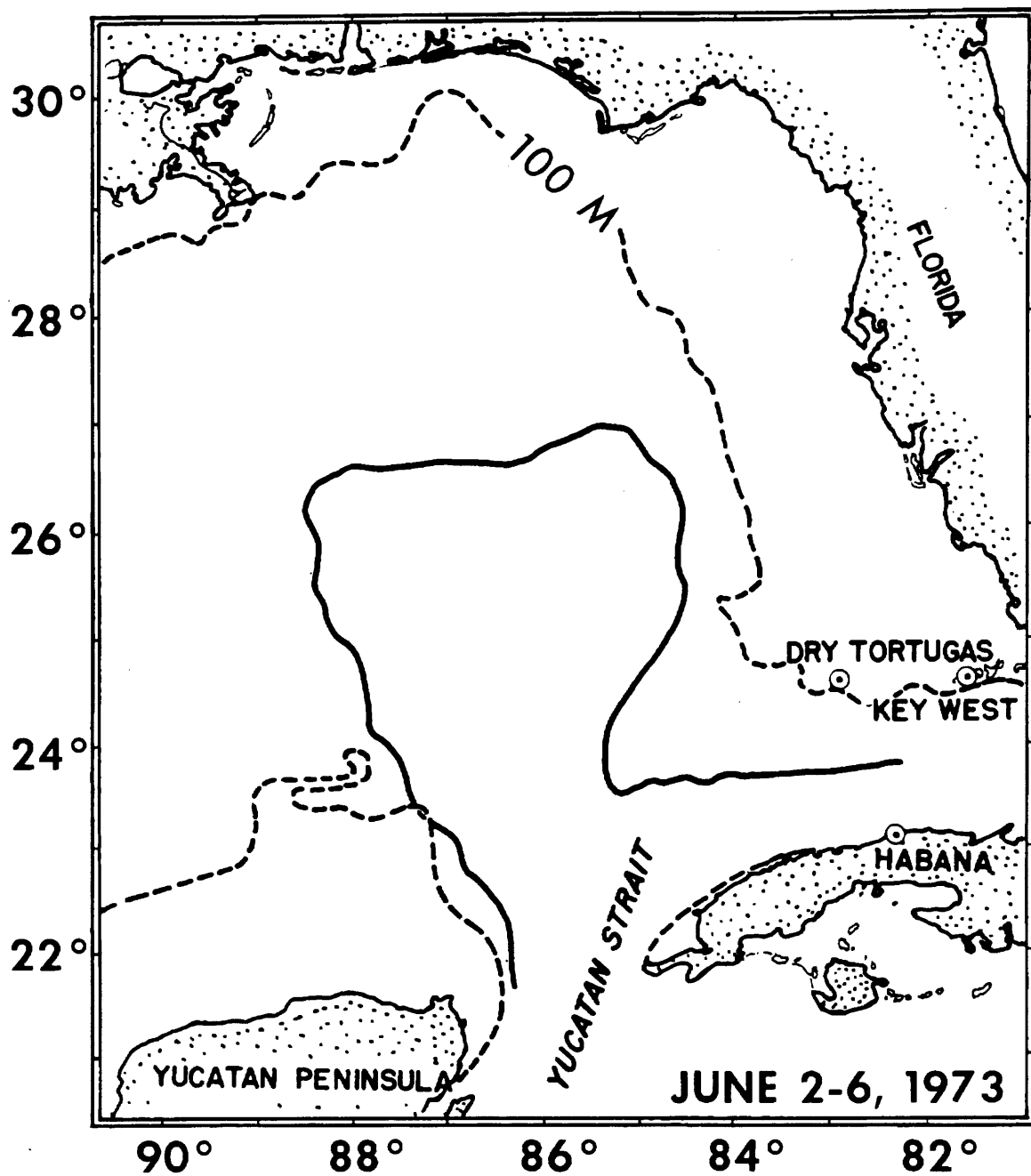


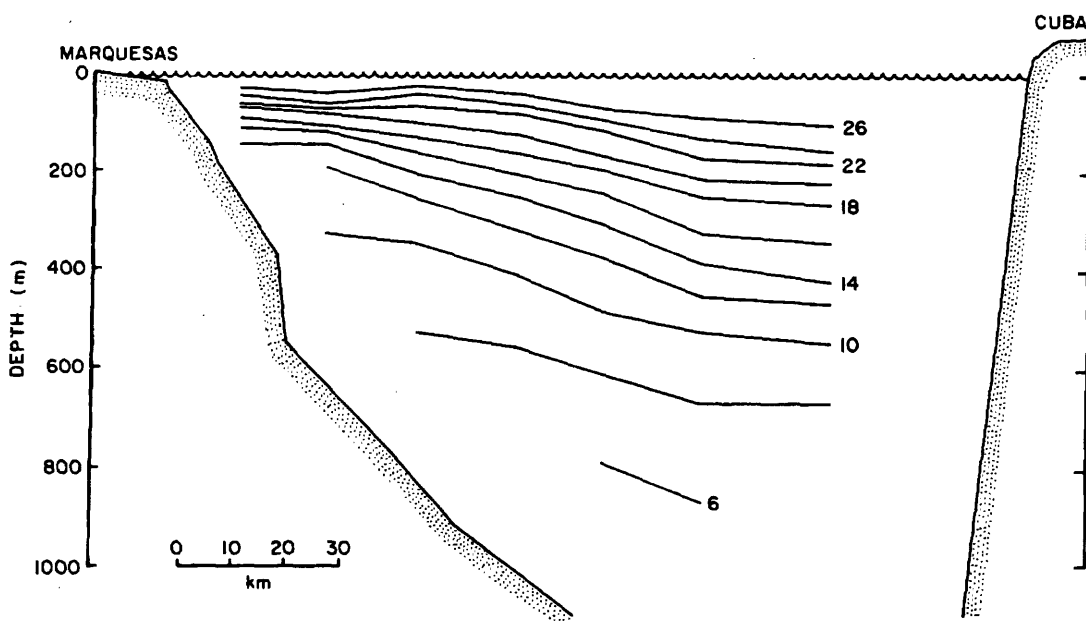
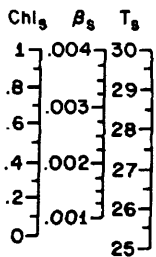


STRAITS OF FLORIDA  
APRIL-MAY 1973

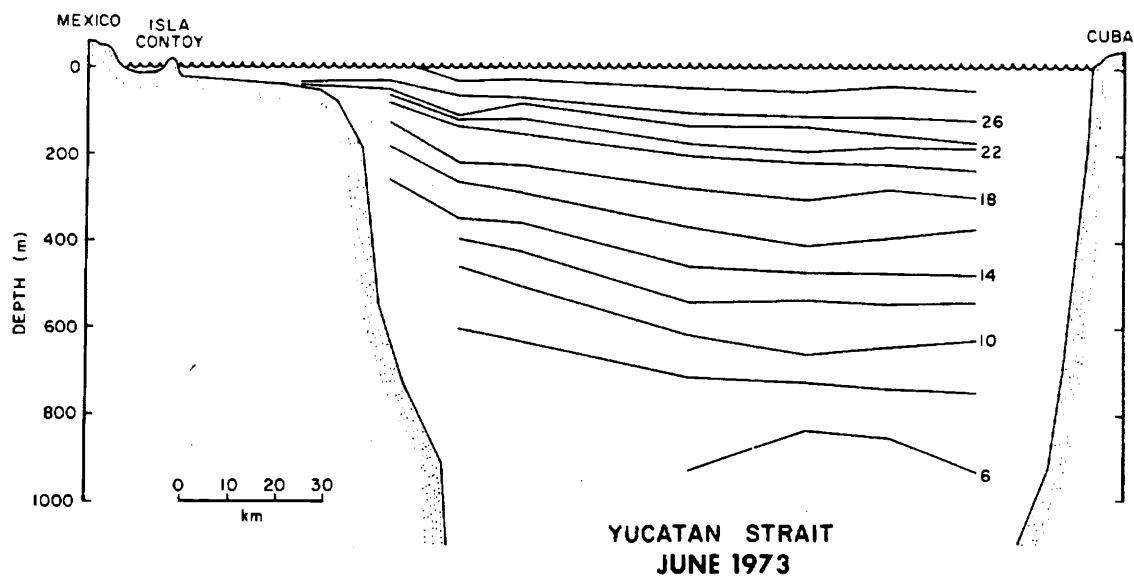
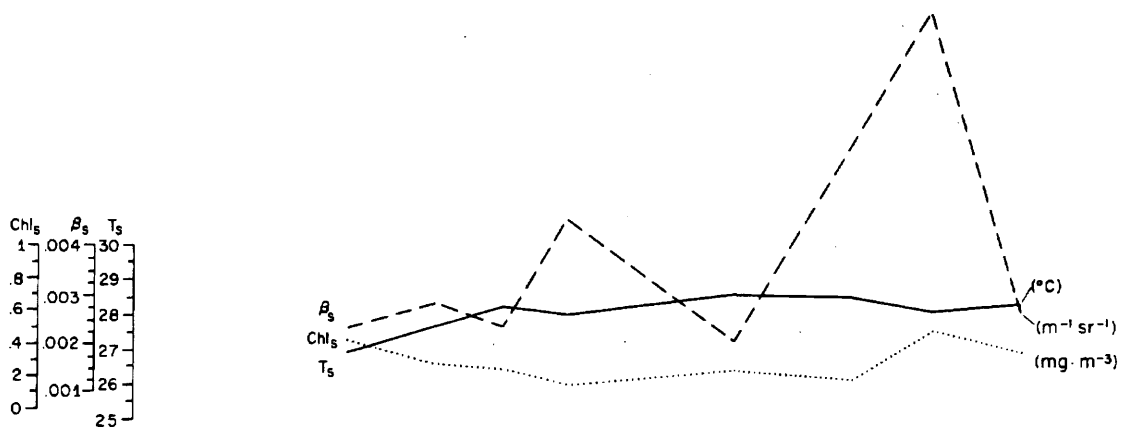


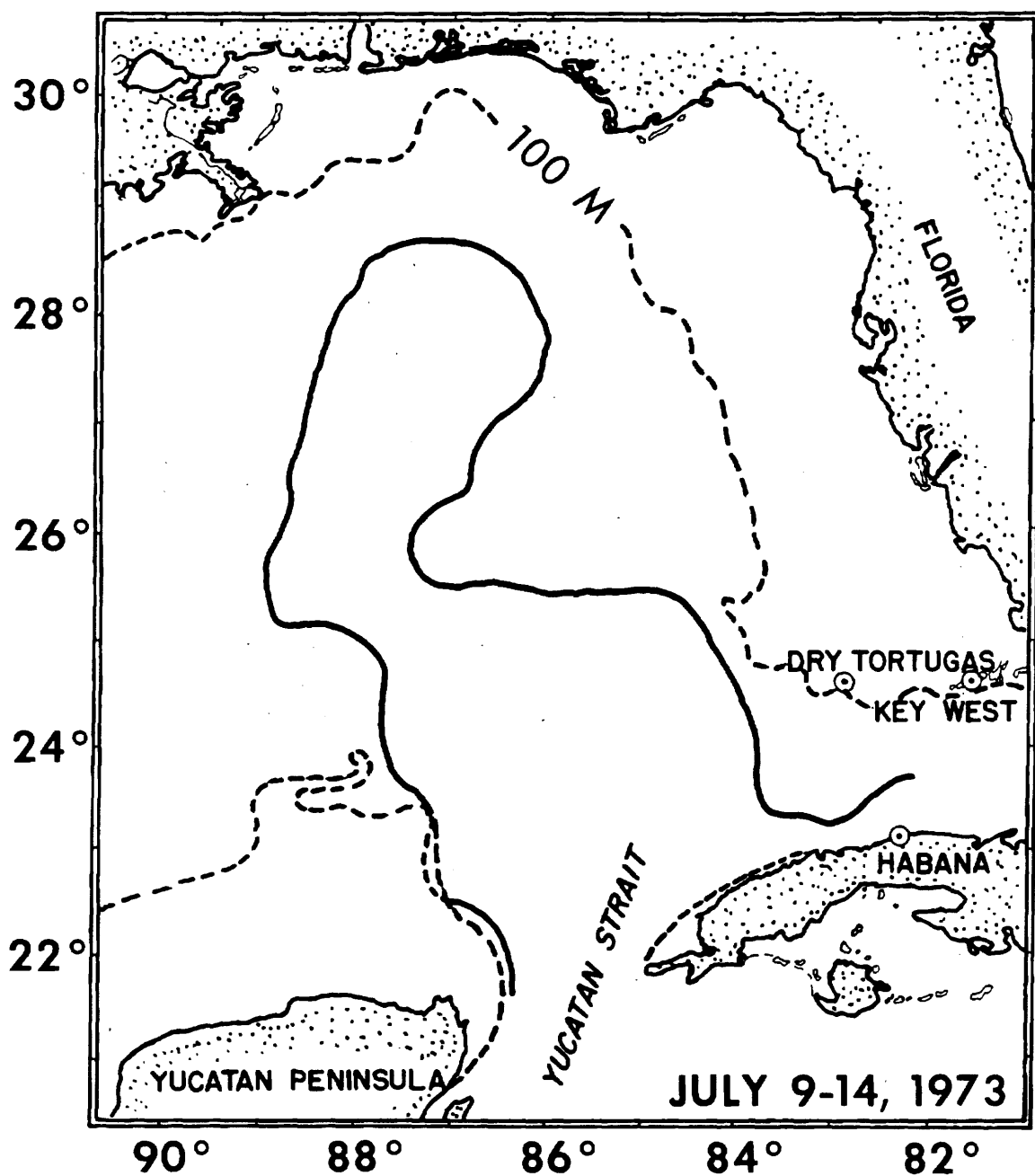


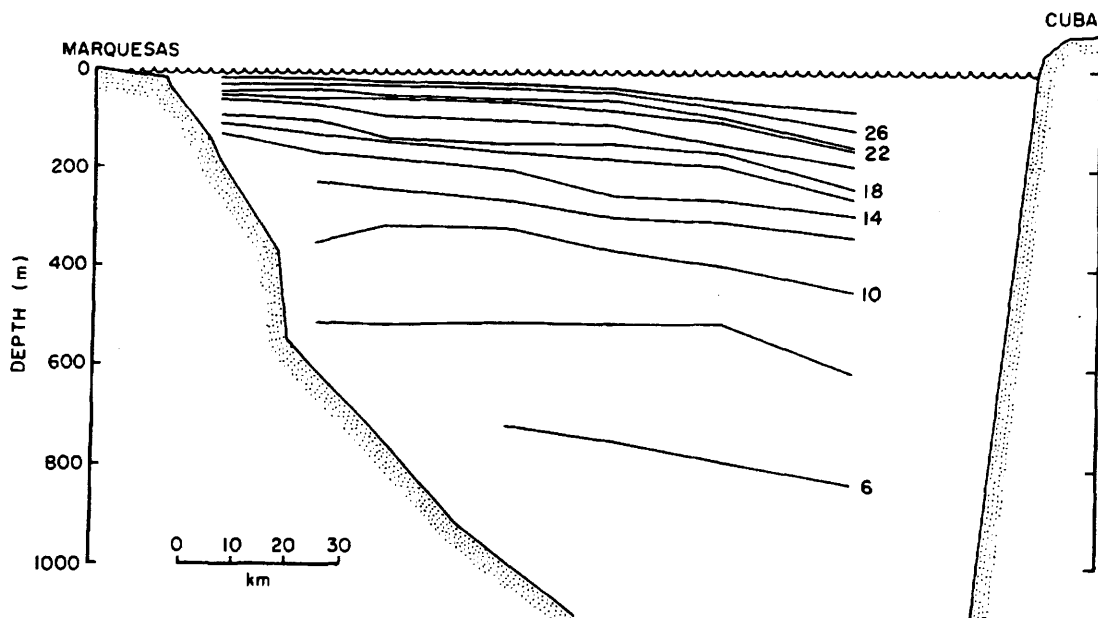
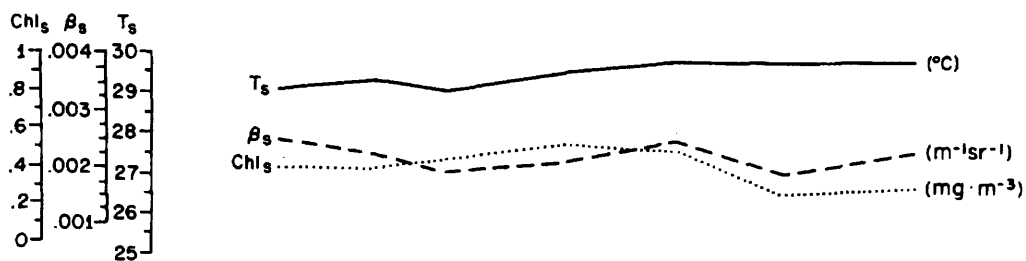




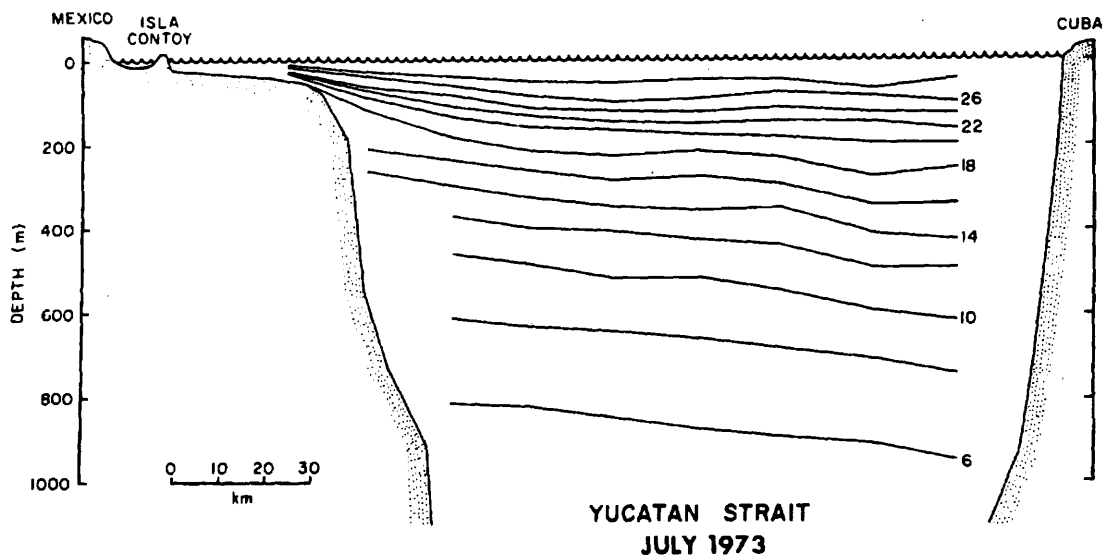
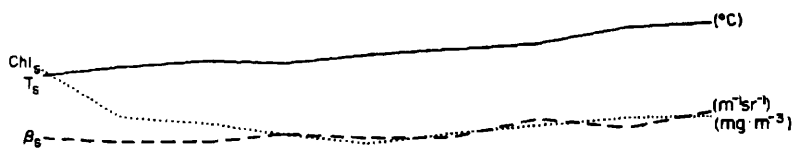
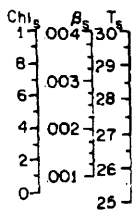
STRAITS OF FLORIDA  
JUNE 1973

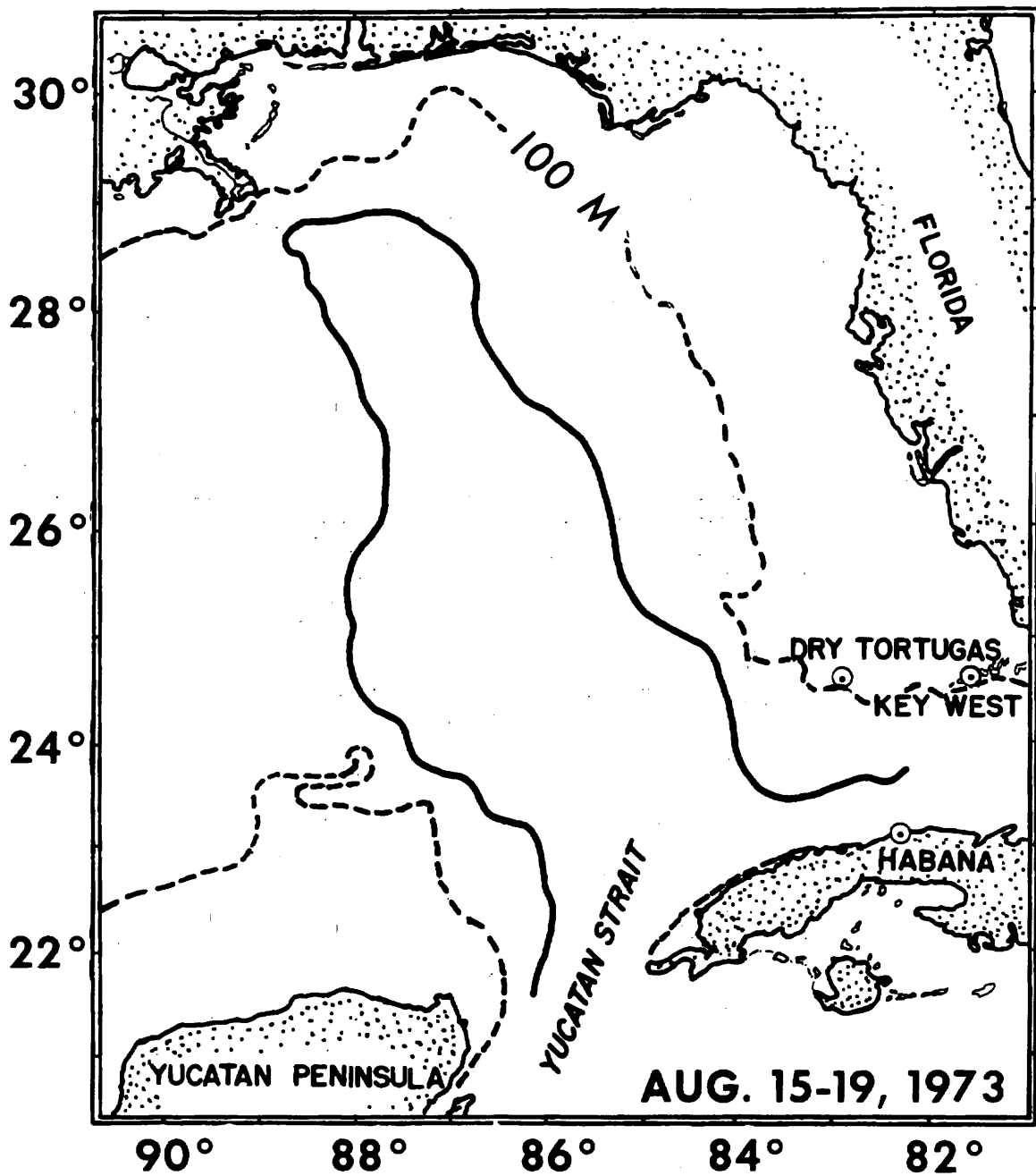




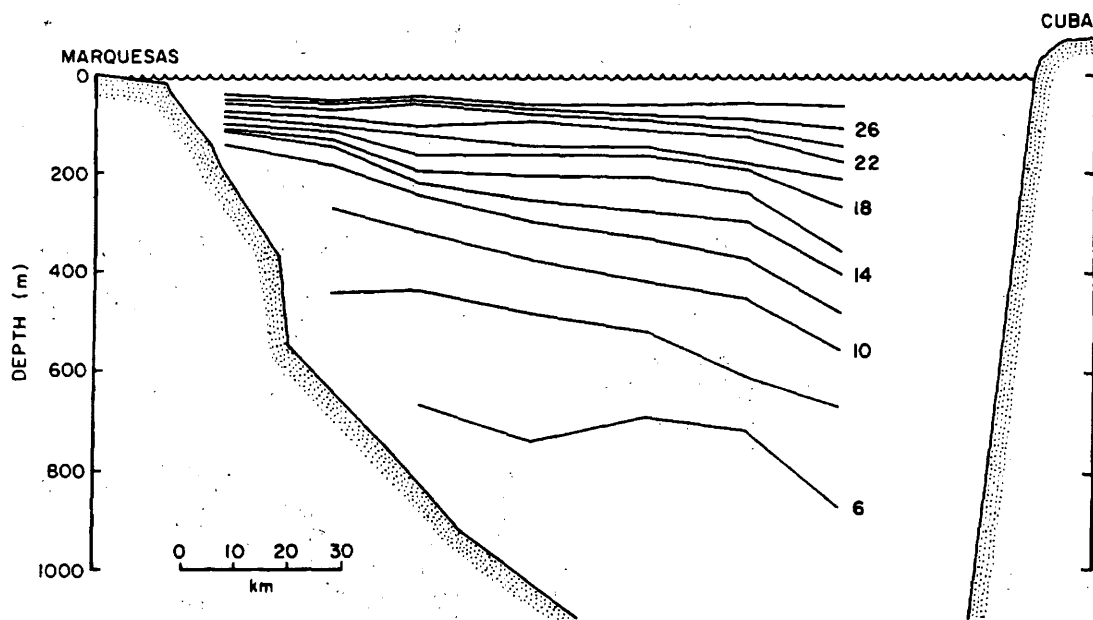
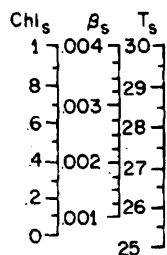


STRAITS OF FLORIDA  
JULY 1973









STRAITS OF FLORIDA  
AUGUST 1973

